

## ABSTRACT

BATTISTA, CHRISTINA. Parameter Estimation of Viscoelastic Wall Models in a One-Dimensional Circulatory Network. (Under the direction of Mette S. Olufsen and Mansoor A. Haider.)

Flow and pressure waves originate from the contraction of the heart and propagate along deformable vessels where the waves are reflected, dampened, and dispersed within smaller sub-networks of vessels. Wave propagation in the circulatory system has been studied from many different angles with the most successful being from a fluid dynamics approach. This thesis develops and applies a one-dimensional nonlinear fluid dynamics model for pulse wave propagation in large systemic ovine arteries with the goal of enhancing the understanding of cardiovascular disease and potentially impacting diagnostic techniques related to systemic hypertension. Hypertension, high blood pressure, is associated with the stiffening of large or small arteries, and by stiffening the arteries in our network, we show the impact that each has on the pressure waveform.

The Navier-Stokes equations that govern blood flow in the large arteries are highly dependent upon the parameters specified by both the in- and outflow boundary conditions as well as the coupled arterial wall model. The most common outflow boundary condition, the three-element Windkessel model, requires diligent estimation of parameters to produce physiologically relevant and sensible results. Simultaneously, biomechanical properties of the arterial wall change along the axial direction, resulting in stiffer arteries and less viscoelasticity with progressively smaller vessels or as diseases progress. With a change in mechanical properties of the arterial wall, in particular viscoelasticity, various amounts of energy are lost throughout the system. Energy loss must then be compensated for in the downstream vasculature via means of the outflow boundary conditions. Thus the Windkessel model relies not only on pressure and flow but also the wall model and its parameters.

While the Windkessel model has been implemented and studied for many years, the current approach for determining the parameters has been based on elastic wall models where minimal amounts of energy are lost as the pulse waves propagate along the network. When incorporating viscoelastic walls where larger energy losses are evident, it is a non-trivial task to estimate the outflow boundary condition parameters. This thesis presents a systemic approach for determining Windkessel parameters based on vessel radius, stiffness, and viscoelasticity.

© Copyright 2015 by Christina Battista

All Rights Reserved

Parameter Estimation of Viscoelastic Wall Models in a One-Dimensional Circulatory  
Network

by  
Christina Battista

A dissertation submitted to the Graduate Faculty of  
North Carolina State University  
in partial fulfillment of the  
requirements for the Degree of  
Doctor of Philosophy

Applied Mathematics

Raleigh, North Carolina

2015

APPROVED BY:

---

Mette S. Olufsen  
Co-chair of Advisory Committee

---

Mansoor A. Haider  
Co-chair of Advisory Committee

---

Brooke N. Steele

---

Pierre Gremaud

---

Sharon Lubkin

## DEDICATION

For all of my grandparents....

Thank you for being my biggest fans and always reminding me I could accomplish this.

*“What children need most are the essentials that grandparents provide in abundance. They give unconditional love, kindness, patience, humor, comfort, lessons in life...and most importantly, cookies.”*

– Rudy Giuliani



## BIOGRAPHY

Christina was born in Buffalo, NY and grew up in a small suburb called Alden. Upon graduating high school in 2007, she attended the Rochester Institute of Technology (RIT) in Rochester, NY where she decided to major in Applied Mathematics. After attending George Washington University's Summer Program for Women in Mathematics at the end of her sophomore year, Christina knew she didn't want her education to end after her bachelor's degree. She registered for the BS/MS program in Applied and Computational Mathematics at RIT and added two minors, Applied Statistics and Criminal Justice, and a concentration in Physics.

While at RIT, she participated in numerous research projects with many professors who helped pave the way for her love of applied mathematics (Dr. Darren Narayan, Dr. Tamas Wiandt, and Dr. David S. Ross). She worked with Dr. David S. Ross at RIT on her master's research project which was entitled "Parathyroid hormone and cell signaling in bone remodeling." This had been the first time Christina applied mathematics to biology-related topics and truly embraced her inner nerd. Realizing that she loved the biology as well as the mathematics being applied to it, she decided to apply for Ph.D. programs where there were opportunities to continue applied mathematics research with biological applications.

In February of 2011, Christina received a call with news that the Department of Mathematics at North Carolina State University was inviting her into their graduate program. She moved to Raleigh that June and Mansoor Haider offered her a research assistantship for the first semester in the 2011 schoolyear. Mansoor Haider and Mette Olufsen advised Christina through four years of research and a successful dissertation defense in August 2015. Christina has accepted a position at The Hamner Institute for Health Sciences as a postdoctoral fellow within the DILI-sim group.

## ACKNOWLEDGEMENTS

First and foremost, I would like to express my sincere appreciation to my advisory committee: Mette S. Olufsen, Mansoor A. Haider, Brooke L. Steele, Pierre Gremaud, and Sharon Lubkin. Thank you all for providing me with support and insightful criticism throughout this research. A special thanks to my advisors, Mette and Mansoor, for their patience and guidance these past four years. A finite amount of words cannot do justice to thank them for helping me grow as a researcher and letting me have a little fun along the way. Their confidence in me never faltered, even when mine did, and they always pushed me to look at the bigger picture. Without their help and support, I wouldn't have made it where I am today.

A special thanks to all the friends I made during graduate school. I was fortunate enough to have been surrounded by so many friends from the moment I moved to North Carolina. There are too many people to list but I am grateful for the distractions provided by sporting events, trivia, craft nights, card games, crosswords, and geocaching. ☺

I am especially thankful for my officemates over the years—Nakeya Williams, Gregory Mader, Christian Olsen, Jacob Sturdy, and Reneé Brady—and to the rest of the Cardiovascular Dynamics Group (#wedonothing). Thank you for not only being classmates and colleagues, but also friends, and for making my workspace such a fun place to be. You guys made research tolerable on the days when I didn't think I could do it and provided me with enough distractions throughout the process to keep me sane. Some of my happiest and my saddest moments in graduate school happened in our office and I'm glad to have had you there to share them with.

Thanks to the most adorable (and supportive!) four-legged friends in the world, Tippy and Zoë, and to the recent family addition, Gus.

Lastly, and most importantly, I want to thank my family both near and far. Graduate school is hard enough as it is and I couldn't imagine doing it without the support of my family. They have been there for me every step of the way, keeping me sane via phone calls and visits, loving me unconditionally, and standing by me through all of my tough decisions.

# TABLE OF CONTENTS

<b>List of Tables</b> . . . . .	<b>vii</b>
<b>List of Figures</b> . . . . .	<b>ix</b>
<b>Chapter 1 Introduction</b> . . . . .	<b>1</b>
1.1 Summary of the dissertation . . . . .	2
<b>Chapter 2 Cardiovascular Physiology</b> . . . . .	<b>4</b>
2.1 The cardiovascular system . . . . .	4
2.1.1 The systemic and pulmonary circuits . . . . .	5
2.1.2 The circulation of blood . . . . .	6
2.1.3 Vasculature . . . . .	9
2.2 Wall tissue . . . . .	11
2.2.1 Biomechanics of wall tissue . . . . .	13
2.2.2 Vascular pathology . . . . .	15
<b>Chapter 3 Experimental Data</b> . . . . .	<b>18</b>
3.1 Experimental setup . . . . .	18
3.1.1 Surgical preparation and acquisition of segments . . . . .	18
3.1.2 <i>Ex vivo</i> experiments . . . . .	19
3.2 Data preprocessing . . . . .	21
3.3 Available data in literature . . . . .	22
3.3.1 Pressure-area data . . . . .	22
3.3.2 Pressure-flow data . . . . .	23
<b>Chapter 4 Modeling Blood Flow in the Arteries</b> . . . . .	<b>26</b>
4.1 One-dimensional fluids models . . . . .	26
4.1.1 Literature review . . . . .	26
4.1.2 Derivation of conservation laws . . . . .	28
4.2 Arterial wall models . . . . .	33
4.2.1 Literature review . . . . .	34
4.2.2 Elastic model . . . . .	36
4.2.3 Viscoelastic model . . . . .	39
4.2.4 Quasilinear viscoelasticity theory . . . . .	44
4.3 Boundary conditions . . . . .	48
4.3.1 Literature review . . . . .	48
4.3.2 Outflow boundary conditions . . . . .	51
4.3.3 Inflow boundary conditions . . . . .	54
4.3.4 Junctions conditions . . . . .	55

<b>Chapter 5</b>	<b>Wave Intensity Analysis</b>	<b>56</b>
5.1	Calculating WIA	57
<b>Chapter 6</b>	<b>Numerical Methods</b>	<b>59</b>
6.1	Literature review	59
6.2	Finite element method	61
6.3	Strong form	62
6.4	Weak form and FEM discretization	62
6.5	Convergence of the solver	67
6.5.1	Non-tapered vessel	67
6.5.2	Tapered vessel	68
<b>Chapter 7</b>	<b>Results</b>	<b>74</b>
7.1	Parameter estimation	74
7.1.1	Vessel stiffness and unstressed vessel radii	75
7.2	Network geometry extracted from <i>ex vivo</i> experimental measurements	77
7.3	Elastic network	80
7.3.1	Model parameters	80
7.3.2	Network simulations	82
7.4	Viscoelastic network	82
7.4.1	Single vessel network	84
7.4.2	Symmetric branching networks	90
7.5	WIA results	99
<b>Chapter 8</b>	<b>Discussion</b>	<b>107</b>
8.1	Limitations and future work	109
<b>Bibliography</b>		<b>111</b>
<b>Appendices</b>		<b>126</b>
Appendix A	Conservation of momentum nondimensionalization	127
Appendix B	Wall model derivatives	130
Appendix C	Hyperbolicity of PDEs	134
C.1	Elastic wall model	134
C.2	Kelvin linear viscoelastic wall model	136
Appendix D	The Nelder Mead Method	138

## LIST OF TABLES

<b>Table 2.1</b>	Percent composition of the <i>media</i> and <i>adventitia</i> of three arteries at <i>in vivo</i> blood pressure. Values given are mean $\pm$ standard deviation. Adapted and reproduced with permission from [55]. . . . .	14
<b>Table 3.1</b>	Summary of data available in literature for <i>in vivo</i> or <i>ex vivo</i> pressure $p$ , area $A$ , and flow $q$ . Also specified are the species and arteries from which the data is measured. . . . .	24
<b>Table 4.1</b>	General summary of blood flow modeling in 1-D and 3-D plus those that have studied and compared results in both dimensions. . . . .	28
<b>Table 4.2</b>	Summary of wall models studied by different groups. . . . .	37
<b>Table 4.3</b>	Two linear wall models written in QLV formulation with creep function $K(t)$ and inverse elastic response function $s^{(e)}[p]$ . Note that the creep function distinguishes between elastic and viscoelastic. . . . .	47
<b>Table 5.1</b>	WIA table showing type and direction of dominating waveforms. Corresponding discretized WIA terminology is given in parenthesis. . . . .	57
<b>Table 6.1</b>	Summary of numerical methods implemented by references to solve 1-D fluid models. MoC: method of characteristics, FDM: finite difference method, FEM: finite element method, DG: discontinuous Galerkin. . . . .	60
<b>Table 7.1</b>	Average geometric and mechanical optimized parameters for the elastic and viscoelastic wall models. Results are presented as mean $\pm$ standard deviation. For all segments, $n = 11$ , $h$ is the wall thickness, $r_0$ is the zero-strain radius, $E$ is the Young's modulus, and $A_1$ and $b_1$ are the viscoelastic relaxation parameters. Parameters noted n.d. are non dimensional. . . . .	76
<b>Table 7.2</b>	Vessel dimensions and flow distribution. For each vessel segment shown in Figure 7.4, the table specifies length, proximal and distal unstressed radius (all in cm), as well as the distribution of flow to the vessel segment [31, 82, 146]. The total cardiac output was set at 66.9 mL/s [40]. Unstressed vessel radii were averaged from optimal values presented in Table 7.1. . . . .	80
<b>Table 7.3</b>	Model parameters. Fluid dynamics parameters were used in both the single vessel (SV) and the network simulations. All vessels are listed in the large network but only terminal vessels require outflow boundary conditions (RCR values). Parameters noted n.d. are non dimensional. . . . .	81

<b>Table 7.4</b>	Results for each of the symmetric networks where $Eh/r_0$ is constant throughout the vasculature. The increasing $R_1$ trend observed in the single vessel and 3-vessel network changes as more generations are added. However, the trends for $R_2$ and $R_1/R_t$ remain the same for the symmetric bifurcating networks. . . . .	94
<b>Table 7.5</b>	Parameter values and units for (7.4.4) and (7.4.5). The notation n.d. indicates non-dimensional quantities. . . . .	96
<b>Table 7.6</b>	Results for each of the symmetric networks where $Eh/r_0$ varies based on $r_0$ throughout the vasculature. $R_1$ now increases for all networks as viscoelastic degree ( $A_1$ ) is increased. However, the trends for $R_2$ and $R_1/R_t$ remain the same for the symmetric bifurcating networks. .	98
<b>Table 7.7</b>	Parameter values and units for (7.4.6) and (7.4.7) relating $R_1$ and $R_2$ to $A_1$ and $r_0$ for symmetric networks where $Eh/r_0$ varies with $r_0$ . . . . .	99

## LIST OF FIGURES

<b>Figure 2.1</b>	A schematic showing the parallel layout of the CVS. The only circulatory beds in series are those between the spleen, intestines, and the liver. Red arrows indicate vessels that carry oxygenated blood, blue vessels indicate those that carry deoxygenated blood. Purple boxes represent major vascular beds where the exchange of gases occurs. Adapted and reproduced with permission from [91]. . . . .	5
<b>Figure 2.2</b>	Blood flow in the heart. Systemic venous blood enters the right atrium (RA) through the superior (SVC) and inferior vena cava (IVC) where it then passes into the right ventricle (RV). The RV ejects blood into the pulmonary artery (PA) where it passes through the lungs and is reoxygenated before flowing through the left atrium (LA) and then filling the left ventricle (LV). From here, the blood is ejected through aorta (A) to be distributed to the major organs. Used with permission from [82]. . . . .	7
<b>Figure 2.3</b>	Pressure gradients in the systemic (left) and pulmonary (right) networks, indicating that the systemic network operates at a much higher pressure than the pulmonary network. Boxed numbers mark mean pressure values at each level. Reprinted with permission from [31]. .	8
<b>Figure 2.4</b>	Pressure-volume loop for the left ventricle including phases of the cardiac cycle and the opening and closing of the valves. Reprinted with permission from [91]. □ . . . . .	9
<b>Figure 2.5</b>	The variation in aggregate cross-sectional area at all levels of arborization. Aggregate cross-sectional area increases as larger arteries branch into smaller arterioles and capillaries. Adapted and reproduced with permission from [31]. . . . .	10
<b>Figure 2.6</b>	Branching of arteries and merging of veins. $r$ indicates the typical radius for a human at that level of arborization. Reprinted with permission from [31]. . . . .	11
<b>Figure 2.7</b>	Histological slices displaying a cross-section of the arterial wall from the ovine thoracic aorta (left) and the carotid artery (right). The vessels were stained with orcein which allows for differentiating the three main biomechanical components of the arterial wall: elastin (dark red), collagen (blue), and smooth muscle cells (yellow). The thoracic aorta has more elastin while the carotid artery contains more collagen. The difference in these compositions explains why the wall of the carotid artery appears “stiffer” than that of the thoracic aorta. Images made available by Dr. Daniel Bia, Universidad de la República, Uruguay. [26, 159] . . . . .	12

<b>Figure 2.8</b>	Vascular size, wall thickness, and relative composition at different levels of arborization in human vasculature. Values for medium arteries, arterioles, venules, and veins are illustrated. It should be noted that the dimensions vary widely vary. Wall compositions values from specific arteries are shown in Table 2.1. Reprinted with permission from [31]. . . . .	13
<b>Figure 2.9</b>	(left) A healthy pressure waveform where the forward wave (emanating from the heart) occurs before the reflected wave (emanating from the periphery). (right) As arterial walls stiffen, pulse wave velocity increases causing the forward and backward waves to occur at the same time, augmenting the pressure waveform. Adapted and reproduced with permission from [164]. . . . .	16
<b>Figure 3.1</b>	Mock circulation including a pneumatic pump, a perfusion line connected to the chamber with the mounted vessel segment, a resistance modulator (R), and a reservoir. The chamber was filled with a thermally controlled Tyrode's solution. Pressure (p) was measured with a micro transducer while the diameter (D) was measured with a pair of ultrasonic crystals using sonomicrometry. . . . .	20
<b>Figure 3.2</b>	Pressure-area, pressure time series, and area time series data from each of the seven excised vessels. Corresponding colors represent vessels from the same sheep. From top left to bottom right: AA, BT, CA, DA, FA, MA, and PA. . . . .	25
<b>Figure 4.1</b>	The velocity profile for varying values of $\gamma$ and the no-slip boundary condition inside a vessel with radius $r$ along the axial direction $x$ . As $\gamma$ increases, the shape changes from a parabolic profile (corresponding to a fully developed flow) to a blunt profile (mimicking a pulsatile flow). This work assumes a parabolic profile corresponding to $\gamma = 2$ . At a solid boundary (the arterial wall where $r = R$ ), the blood has zero velocity relative to boundary. This is true for any time $t$ and any $x$ along the axial direction. . . . .	32
<b>Figure 4.2</b>	The three simplest linear viscoelastic models composed of springs and dashpots: (a) Maxwell, (b) Voigt, and (c) Kelvin. Linear springs produce instantaneous deformations proportional to the load while dashpots slow motion, absorb energy, and produce velocity proportional to the load. . . . .	36
<b>Figure 4.3</b>	A diagram of the forces acting on a vessel under static equilibrium conditions. The $F_{outward}$ is due to blood pressure acting on the interior wall of the vessel and $F_{inward}$ is the force acting on the exterior of the wall. This is the cross-sectional area of half of a vessel with length $l$ . . . . .	37



<b>Figure 4.4</b>	The Kelvin viscoelastic model illustrated using mechanical analogs with a combination of two Hookean elastic springs and a dashpot. . . . .	40
<b>Figure 4.5</b>	The WK analogy to an air chamber. . . . .	50
<b>Figure 4.6</b>	Diagram depicting the three-element WK model. . . . .	51
<b>Figure 6.1</b>	(1st row) Maintaining the time steps per period (1200) converges for any number of elements. This shows spatial convergence for a straight elastic vessel. (2nd row) The temporal residual errors shown for pressure and area of an elastic non-tapered vessel on a log-log plot. (3rd row) The vessel is discretized spatially into 12 elements while increasing the time steps per period: 200, 400, 800, 1200, 2400, 4800, 9600. It is apparent that the solutions corresponding to 800, 1200, 2400, 4800, and 9600 time steps are the same, thus signifying temporal convergence of the solver. (4th row) The spatial residual errors shown for pressure and area of an elastic non-tapered vessel on a log-log plot. . . . .	70
<b>Figure 6.2</b>	(1st row) Convergence in space for the viscoelastic wall model for a non-tapered vessel with 1200 time steps per period. Although we change the number of elements (spatial mesh), we obtain the same results thus signifying convergence. (2nd row) The spatial residual errors shown for pressure and area of a viscoelastic non-tapered vessel on a log-log plot. (3rd row) Temporal convergence for the viscoelastic wall model with a non-tapered vessel discretized spatially into 12 elements. If each period is discretized into 800 or more time steps, we see convergence of the solver. (4th row) The temporal residual errors shown for pressure and area of a viscoelastic non-tapered vessel on a log-log plot. . . . .	71
<b>Figure 6.3</b>	(1st row) Maintaining the time step at 800 per period, we obtain approximately the same results for 50, 100, or 200 elements. Thus, signifying spatially convergence for 50 or more elements in an elastic tapering vessel. (2nd row) The spatial residual errors shown for pressure and area of an elastic tapered vessel on a log-log plot. (3rd row) The number of elements remains fixed at 12 per vessel while the time steps are 200, 400, 800, 1200, 2400, 4800, 9600 per period. It is apparent that the solutions corresponding to 1200, 2400, 4800, and 9600 time steps are the same, thus signifying temporal convergence of the solver. (4th row) The temporal residual errors shown for pressure and area of an elastic tapered vessel on a log-log plot. . . . .	72

<b>Figure 6.4</b>	(1st row) Convergence in space for the viscoelastic wall model in a tapered vessel. Although we change the number of elements (spatial mesh), we obtain the same results for 100+ elements, thus signifying convergence. (2nd row) The spatial residual errors shown for pressure and area of a viscoelastic tapered vessel on a log-log plot. (3rd row) Temporal convergence for the viscoelastic wall model with a tapered vessel discretized spatially into 12 elements. (4th row) The temporal residual errors shown for pressure and area of a viscoelastic tapered vessel on a log-log plot. . . . .	73
<b>Figure 7.1</b>	Elastic modulus and zero-strain radius optimized values for larger ovine arteries. . . . .	77
<b>Figure 7.2</b>	Measured diastolic radius values plotted against the theoretical, optimized elastic zero-strain radius for each sheep in each vessel. . . .	78
<b>Figure 7.3</b>	The best fit exponential decay function for all data points including those from the sheep data and those provided in Olufsen's dissertation. . . . .	78
<b>Figure 7.4</b>	The network geometry. The seven arteries from which pressure-area measurements have been taken are marked with letters (AA, BT, CA, PD, MD, DD, FA), while other major vessels are marked with letters in parenthesis (CM, RA, IL, IT). In the model, the renal arteries and the celiac and mesenteric arteries were each combined into a single vessel, and the carotid, iliac, and femoral bifurcations were modeled as symmetric. . . . .	79
<b>Figure 7.5</b>	Flow and pressure-area computations and data for each vessel in the network. . . . .	83
<b>Figure 7.6</b>	Pressure and flow waveforms along the aorta in an elastic network. Systolic pressure increases progressing toward the periphery. . . . .	84
<b>Figure 7.7</b>	Single non-tapered vessel representative of the ascending aorta where we have assumed a non-tapering vessel. This geometry is used to study the affects of the in- and outflow boundary conditions. . . . .	84
<b>Figure 7.8</b>	Model predictions in a single vessel (the ascending aorta) mimicking results from a specific sheep. . . . .	85
<b>Figure 7.9</b>	Effect of changing the WK parameters in a single vessel network. . . .	87
<b>Figure 7.10</b>	Effect of changing the compliance parameter values in a single vessel network. . . . .	88
<b>Figure 7.11</b>	Effect of changing wall viscosity while keeping outflow boundary conditions constant. $A_1$ ranges from 0 (corresponding to an elastic wall) to 0.867 in spectrum order. As $A_1$ increases, a decrease in pulse pressure is observed. . . . .	89

<b>Figure 7.12</b>	(Top) Results for matching pulse pressure in a single vessel. By increasing the peripheral resistance in the WK model as wall viscoelasticity increases, we are able to obtain the same pulse pressure but mean pressure increases. (Bottom) Results for matching mean pressure in a single vessel. As wall viscoelasticity increases, the distal resistance in the WK model must decrease in order to maintain the same mean pressure. However, this simultaneously leads to an increase in pulse pressure. . . . .	89
<b>Figure 7.13</b>	Increasing wall viscoelasticity while maintaining constant pulse and mean pressures requires an increase in proximal resistance and a decrease in distal resistance of the WK model, conserving the total resistance. The $R_1/R_T$ ratio, previously taken to be 0.2 [99], is directly correlated with wall viscoelasticity. As seen in the left bottom row, matching pulse pressure and mean pressure maintains pressure shape and size. . . . .	90
<b>Figure 7.14</b>	Symmetric geometries used to determine WK parameters in viscoelastic networks. From left to right: 3-, 7-, and 15-vessel networks. Note that these are representative and do not reflect the actual geometries. . . . .	91
<b>Figure 7.15</b>	$R_1$ and $R_2$ associated with each daughter vessel plotted as functions of $\zeta$ and $A_1$ . The total network resistance is defined as $2R_{Td}$ where $R_{Td} = R_1 + R_2$ as shown in the figures. Red lines show the functions given by (7.4.1) and (7.4.2). . . . .	92
<b>Figure 7.16</b>	A circuit of resistors $R_1, R_2, \dots, R_n$ in parallel. The total resistance of the circuit can be calculated using (7.4.3). . . . .	93
<b>Figure 7.17</b>	Total resistance in each symmetric network for increasing values of $A_1$ . It is important to note that when $A_1 = 0$ , corresponding to a purely elastic wall, the networks have the same total resistance. This supports our hypothesis that as viscoelastic vessels are added into a network, more energy is lost and thus higher resistances are needed at the outflow boundary conditions to account for these losses. The total resistance corresponding to the elastic models matches the total resistance found in the single vessel network and is equal to the mean pressure divided by the mean flow ( $R_T = \bar{p}/\bar{q}$ ). . . . .	95
<b>Figure 7.18</b>	$R_1$ (left) and $R_2$ (right) as functions of $A_1$ and $r_0$ for symmetric networks where $ Eh/r_0$ is the same in all vessels. $R_1$ is a second-order polynomial in $A_1$ and $r_0$ whereas $R_2$ is the sum of two exponentials containing $A_1$ and $r_0$ . As $A_1$ increases, we see the exponential increase in $R_2$ which makes large values of $A_1$ physiologically unfeasible for the given network setup. . . . .	95

<b>Figure 7.19</b>	Total resistance in each symmetric network for increasing values of $A_1$ . Again, the total resistance remains the same in each network for the elastic wall model and can be found via $R_T = \bar{p}/\bar{q}$ . As more viscoelastic vessels are added to the network, higher resistances are needed in the WK models to account for energy losses due to the wall model. . . . .	99
<b>Figure 7.20</b>	$R_1$ (left) and $R_2$ (right) as functions of $A_1$ and $r_0$ for symmetric networks where $ Eh/r_0$ is the same in all vessels. Both $R_1$ and $R_2$ are defined as second-order polynomials in $A_1$ and $r_0$ . . . . .	100
<b>Figure 7.21</b>	WIA in a single straight vessel where $ Eh/r_0$ is varied with an elastic wall (top) and where $A_1$ is varied in the viscoelastic model (bottom). The normal $ Eh/r_0$ value is shown in black. $ Eh/r_0$ varies as 25%, 50%, 150%, and 200% of this value. $A_1$ varies between 0 and 0.8 in increments of 0.2. . . . .	102
<b>Figure 7.22</b>	WIA for 3-vessel networks: (top) $ Eh/r_0$ constant, (bottom) $ Eh/r_0$ varying with $r_0$ . $A_1 = 0$ corresponding to the elastic case is shown in red; increasing $A_1$ given by the spectrum order. Velocity appears similar in the two cases; this is different from Figures 7.23 and 7.24. .	103
<b>Figure 7.23</b>	WIA for 7-vessel networks: (top) $ Eh/r_0$ constant, (bottom) $ Eh/r_0$ varying with $r_0$ . In the case of $ Eh/r_0$ varying exponentially with $r_0$ , the pressure and velocity waveforms are lined up for all cases of viscoelasticity validating our method for choosing WK parameters. . . .	104
<b>Figure 7.24</b>	WIA for 15-vessel networks: (top) $ Eh/r_0$ constant, (bottom) $ Eh/r_0$ varying with $r_0$ . The pressure and velocity waveforms are lined up for all cases of viscoelasticity when $ Eh/r_0$ varies exponentially with $r_0$ . . . . .	105
<b>Figure 7.25</b>	WIA in the ascending aorta from an elastic network mimicking healthy conditions. Note that there are more reflections present due to the number of bifurcations. . . . .	106

---

# Chapter 1

---

## Introduction

Cardiovascular diseases, defined as disorders of the heart and blood vessels, are the number one cause of death globally with 17.5 million deaths in 2012 [181] and an estimated 23.6 million deaths in 2030. One of the major risk factors for cardiovascular disease is hypertension, or elevated blood pressure. Hypertension can lead to coronary heart disease and is considered the most important risk factor for stroke, causing more than half of ischaemic strokes (obstruction of blood to the brain) and drastically increasing the risk for hemorrhagic stroke (ruptured vessels that bleed into the brain) [181].

One-third of the adult population (70 million people) in the United States suffers from hypertension and only half have their condition under control [36]. Another 70 million adults are prehypertensive [36], indicating a risk for hypertension. The etiology of hypertension is largely unknown [18], with little to no progress towards achieving an accepted hypothesis. The past century provided hypotheses on the relationship between hypertension and arteriosclerosis, and suggested that the splanchnic nerves and circulation play major roles in hypertension. One hypothesis is that the pathophysiology associated with the stiffening of large or small arteries causes changes in the hemodynamics and wave propagation in the circulatory network. Novel hypotheses on the etiology of hypertension, such as stiffening of arteries, can be interpreted and supported (or rejected) via means of computational modeling thus encouraging the need for this line of research.

## 1.1 Summary of the dissertation

My work focused on 4 aims: (1) to derive a 1-D fluid dynamics model that can be coupled with elastic or viscoelastic arterial wall models to study wave propagation, (2) to estimate parameters associated with arterial wall models and determine how these change with arterial cross-sectional area, (3) to construct and validate a systemic ovine arterial network model predicting *ex vivo* pressure and area, and (4) to develop a systematic approach analyzing how energy losses due to wall viscoelasticity effect outflow boundary conditions. The latter is important for network simulations which require large computations with many parameters, all of which must be estimated to obtain physiological results. Elastic networks are easier to calibrate than viscoelastic network. By forming a systematic approach to estimating outflow parameters in viscoelastic arteries, network simulation construction is simplified.

- Chapter 2 introduces structural and functional properties of the cardiovascular system relevant for the models developed in Chapter 4.
- Chapter 3 describes the experimental procedures used by the Hemodynamics Laboratory at the Universidad de la República in Montevideo, Uruguay to acquire pressure and area data from systemic ovine arteries. Moreover, it provides an overview of literature data available for validating 1-D blood flow models.
- Chapter 4 derives the 1-D model used for predicting arterial blood pressure, volumetric flow, and cross-sectional area in arterial networks. The major components are a 1-D fluids model, arterial wall models, and models of the boundary conditions. The 1-D fluids model is derived from the Navier-Stokes equations under the assumption of an axisymmetric, incompressible flow. The arterial wall models use the framework of Fung's quasilinear viscoelasticity theory which formulates arterial strain as a function of stress. The outflow boundary conditions are modeled by a three-element Windkessel model, relating pressure and flow at the outlet of terminal vessels. Each of these three components are accompanied by a literature review.
- Chapter 5 briefly presents wave intensity analysis, a method for analyzing wave reflections due to junctions and the peripheral vessels.

- Chapter 6 sets up the numerical scheme used to solve the system of partial differential equations. A stabilized space-time finite element method based on a discontinuous Galerkin method in time was utilized to solve the nonlinear equations governing pulsatile blood flow in the arteries. Results confirming convergence of the solver in a single vessel geometry are shown.
- Chapter 7 shows results for computations with elastic and viscoelastic networks. The inverse problem allowing for estimation of wall model parameters is briefly described. An elastic network geometry is developed and used to confirm the adequacy in using discrete *ex vivo* data in network simulations. The viscoelastic network is the heart of this dissertation and builds upon smaller networks to construct a clearcut way to predict outflow boundary conditions based on geometry, wall viscoelasticity, and vessel stiffness.
- Chapter 8 summarizes the key points addressed in this dissertation and suggests future research.

---

## Chapter 2

---

# Cardiovascular Physiology

This chapter presents the cardiovascular system, specifically the systemic arterial network which distributes blood from the left ventricle to the periphery. The general information presented here is from physiology books by Boron [31], Smith and Kampine [146], Levick [91], and Klabunde [82]. Section 2.1 outlines the cardiovascular system (CVS) and its functions while Section 2.2 presents various properties of the vasculature as well as common diseases affecting the arterial wall.

### 2.1 The cardiovascular system

The CVS is composed of a sophisticated network of blood vessels that facilitates the transportation of nutrients (oxygen, glucose, amino acids, fatty acids, vitamins, drugs, water) to and the removal of metabolic waste products (carbon dioxide, urea, creatinine) from tissues. There are three primary components of the CVS: 1) a pump (the heart), 2) the liquid (blood), and 3) a network (vessels). The system consists of two main divisions that form a closed network (Figure 2.1): the larger systemic division and the smaller pulmonary division.



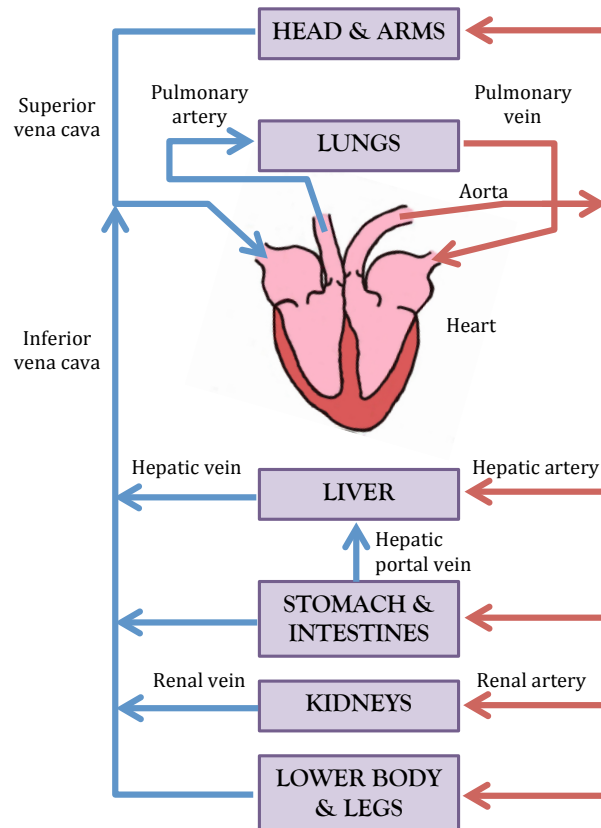


**Figure 2.1** A schematic showing the parallel layout of the CVS. The only circulatory beds in series are those between the spleen, intestines, and the liver. Red arrows indicate vessels that carry oxygenated blood, blue vessels indicate those that carry deoxygenated blood. Purple boxes represent major vascular beds where the exchange of gases occurs. Adapted and reproduced with permission from [91].

### 2.1.1 The systemic and pulmonary circuits

The heart, weighing only 300 grams, contains four chambers (Figure 2.2), making up two pumps that feed the pulmonary and systemic circulatory [146]. The pulmonary circuit involves the flow of deoxygenated blood from the right heart to the lungs, the flow within the lungs, and the flow of oxygen-rich blood back to the left heart. As blood passes through the lungs, oxygen and carbon dioxide are exchanged between the capillaries and the gases within the alveoli. The oxygenated blood is transported from the left heart throughout the body via the systemic circulation to organs where it diffuses from the blood into the surrounding tissue. Simultaneously, carbon dioxide and other waste products diffuse from

the tissues into the blood where they are transported back to the lungs and the exchange between blood and gases is made once again. Compared to the pulmonary circuit, the systemic circuit operates under a higher mean pressure as shown in Figure 2.3, 15 and 95 mmHg, respectively [31].

The right and left sides of the heart each contain an atrium and a ventricle. The left ventricle and left atrium are connected via the mitral (or bicuspid) valve which, under normal conditions, prevents back flow from the ventricle into the atrium. The right ventricle and right atrium are connected via the tricuspid valve which serves a similar purpose as the mitral valve. Venous blood from the systemic circulatory system is returned to the heart through the right atrium, and the right ventricle then cycles the blood to the pulmonary circuit. The blood leaves the pulmonary system and enters the left atrium via pulmonary veins where it then flows into the left ventricle. The left ventricle ejects blood into the systemic circuit, beginning with the aorta which then, in turn, distributes the blood throughout the body to all the organs. Blood that flows from the aorta to the major organ systems ultimately enters the venous system, the superior and inferior vena cava, and is then returned to the heart. Circulation to the major organ systems occurs primarily in parallel as shown in Figure 2.1.

Within organs, the arterial vasculature branches into smaller and smaller vessels. This branching, along with the decrease in radial size of the arteries, is vital to maintaining blood pressure and flow throughout the network. Its importance will be emphasized in the next section.

### **2.1.2 The circulation of blood**

The walls of the heart are composed of muscle tissue called the myocardium. The myocardium consists of three layers: the two outermost layers of fibers are diagonally oriented from the base of the heart to the apex, and the innermost layer is circumferentially oriented. Upon contraction, the innermost layers shorten the ventricular wall, pulling the apex towards the base while the circumferential fibers constrict the ventricular diameter of the heart.

As the heart pumps blood into the vasculature, a pressure gradient is induced within the network. This can be described by classical hydrodynamic laws, the most important in this scenario analogous to Ohm's law of electricity. Thus, the pressure difference ( $\Delta P$ ) between two points is equal to the product of the flow ( $Q$ ) and the resistance ( $R$ ), i.e. a higher

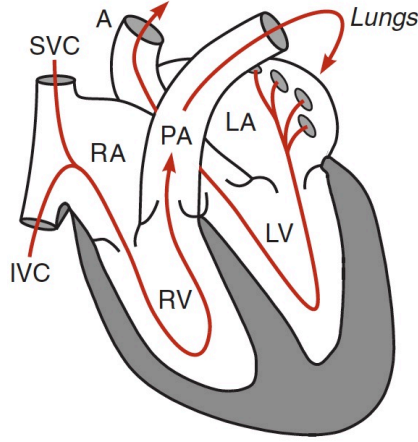


**Figure 2.2** Blood flow in the heart. Systemic venous blood enters the right atrium (RA) through the superior (SVC) and inferior vena cava (IVC) where it then passes into the right ventricle (RV). The RV ejects blood into the pulmonary artery (PA) where it passes through the lungs and is re-oxygenated before flowing through the left atrium (LA) and then filling the left ventricle (LV). From here, the blood is ejected through aorta (A) to be distributed to the major organs. Used with permission from [82].

pressure gradient is required to drive a given flow through a vessel with higher resistance:

$$\Delta P = Q R. \quad (2.1.1)$$

Alternatively, arterial resistance can be calculated based on vessel length  $L$  and radius  $r$  if the flow fulfills Poiseuille's law i.e. a fully-developed flow of a viscous liquid through a rigid, cylindrical pipe where the flow velocity varies from zero at the walls to a maximum along the centerline. Where applicable, this resistance is given as

$$R = \frac{8 \eta L}{\pi r^4} \quad (2.1.2)$$

where  $\eta$  is the viscosity. Based on Poiseuille's law, in wide vessels (such as the aorta), resistance is low because there is a larger area for the flow to pass through. In contrast, the resistance is higher in narrower vessels. In humans, large arteries account for 2% of the total systemic resistance, whereas the arterioles, capillaries, and the venous system make up 60%, 20%, and 15%, respectively [31].

The cardiac output (CO) is defined as the amount of blood ejected during each heart-beat (called stroke volume, SV) multiplied by the heart rate (HR):

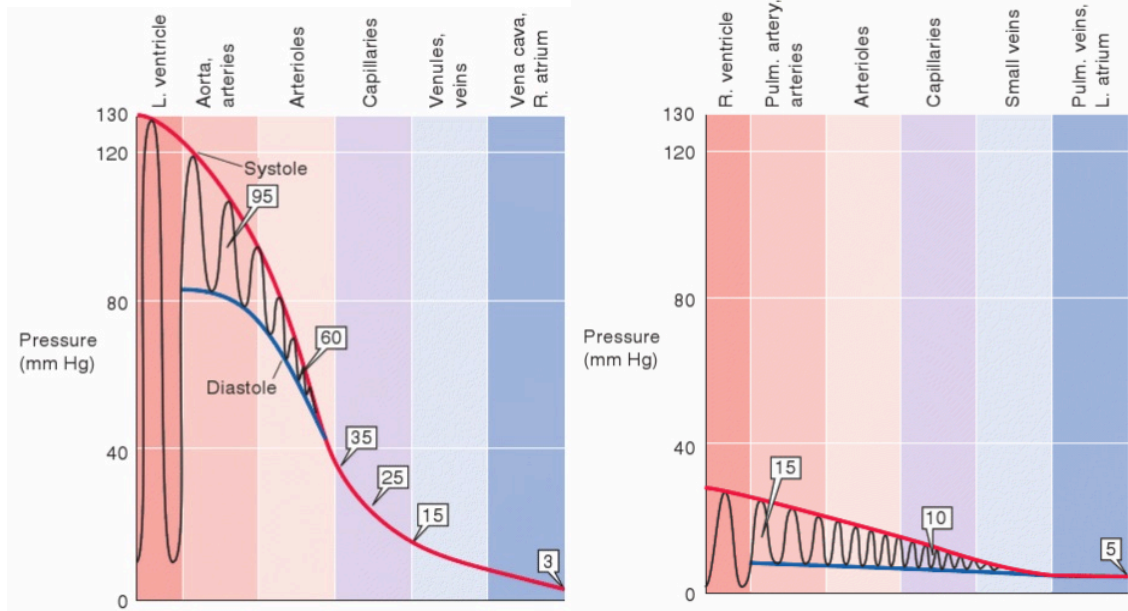


**Figure 2.3** Pressure gradients in the systemic (left) and pulmonary (right) networks, indicating that the systemic network operates at a much higher pressure than the pulmonary network. Boxed numbers mark mean pressure values at each level. Reprinted with permission from [31].

$$CO = SV \cdot HR, \quad (2.1.3)$$

i.e. changes in the heart rate or stroke volume will influence the cardiac output. The heart rate is determined by groups of cells known as pacemaker cells. These cells generate action potentials that are conducted throughout the heart and trigger contraction of the cardiac myocytes (or cardiac muscle cells.) This contraction results in the ejection of blood and the force of this contraction regulates stroke volume. The magnitude of this force is controlled by autonomic nerves and hormones. Stroke volume in a resting adult is typically 70-80 mL and heart rate is 60-75 beats per minute (bpm), resulting in a cardiac output of 5L/min [146]. It can increase in response to external factors (fear, excitement) or an increased peripheral oxygen demand (exercise). Cardiac output has been known to increase up to five times the normal amount during strenuous exercise [146]! At rest in the supine position, the average blood pressure is about 120/80. This corresponds to the ejection of blood in intermittent patterns during systole and rest during diastole where the systemic arterial pressure peaks at 120 mmHg and decays to 80 mmHg.

The systolic and diastolic portions allow the cardiac cycle to divide into an active phase and a relaxed phase (see Figure 2.4). The active phase results in an increase in pressure while the volume remains constant. When the ventricular pressure exceeds the arterial pressure, the aortic valve opens (initiating systole) and blood flows into the aorta. Systole ends when the aortic valve closes and ventricular pressure drops below the arterial pressure. The mitral valve opens and blood passes from the atrium into the ventricle. The mitral valve closes, initiating the cycle again.

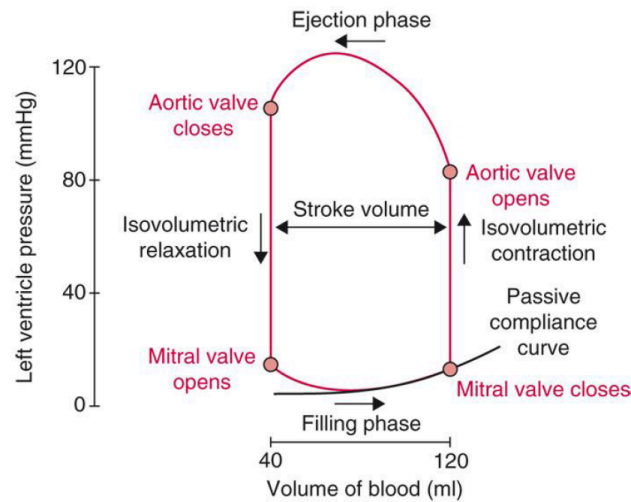


**Figure 2.4** Pressure-volume loop for the left ventricle including phases of the cardiac cycle and the opening and closing of the valves. Reprinted with permission from [91]. □

### 2.1.3 Vasculature

The aorta, stemming from the heart, is the largest artery in the body and branches into many large conduit arteries. These arteries branch repeatedly into smaller arteries which branch into even smaller vessels called arterioles, known to have a very high resistance. Arterioles ultimately branch into an abundant number of thin-walled capillaries 2.6. Through *arborization*, or branching of the arterial network, the number of vessels increases thus increasing the aggregate cross-sectional area at each level (Figure 2.5).

For instance, the aorta (radius  $\sim 1.1$  cm in humans) ultimately branches into  $\sim 10^4$  small

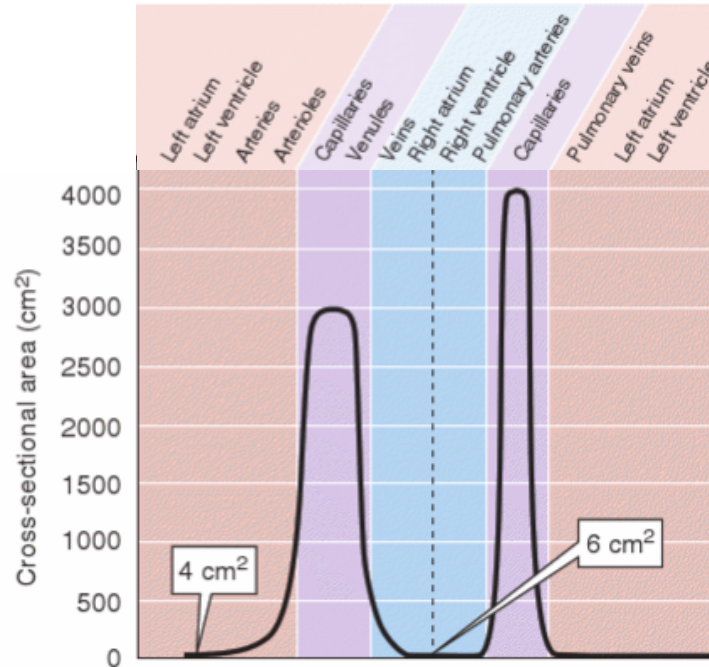


**Figure 2.5** The variation in aggregate cross-sectional area at all levels of arborization. Aggregate cross-sectional area increases as larger arteries branch into smaller arterioles and capillaries. Adapted and reproduced with permission from [31].

arteries,  $\sim 10^7$  arterioles, and  $\sim 4 \times 10^{10}$  capillaries (radii  $\sim 3 \mu\text{m}$ .) These capillaries then converge to form venules. Venules converge into small veins, ultimately merging to become larger, named veins such as the vena cava.

The structural branching is crucial in slowing the blood flow as the vessels decrease in size, thus increasing in vascular resistance. From (2.1.1), as resistance increases, blood flow decreases causing the blood velocity in capillaries to be 1/200th of the arterial velocity [31]. The slowing is necessary to give the red blood cells sufficient time to exchange carbon dioxide and oxygen. Capillaries are closest in proximity to cells in the body, and thus they permit this exchange. Similarly, the arborized structure allows for lower blood pressure values as vessels decrease in size. The largest drop in pressure is believed to occur in the arterioles (as shown in Figure 2.3). For this reason, arterioles are theoretically referred to as the resistance vessels although pressure in these vessels cannot be measured but rather shown computationally [126].

While all vessels exhibit some capacitance due to their elasticity, venous vessels, act-

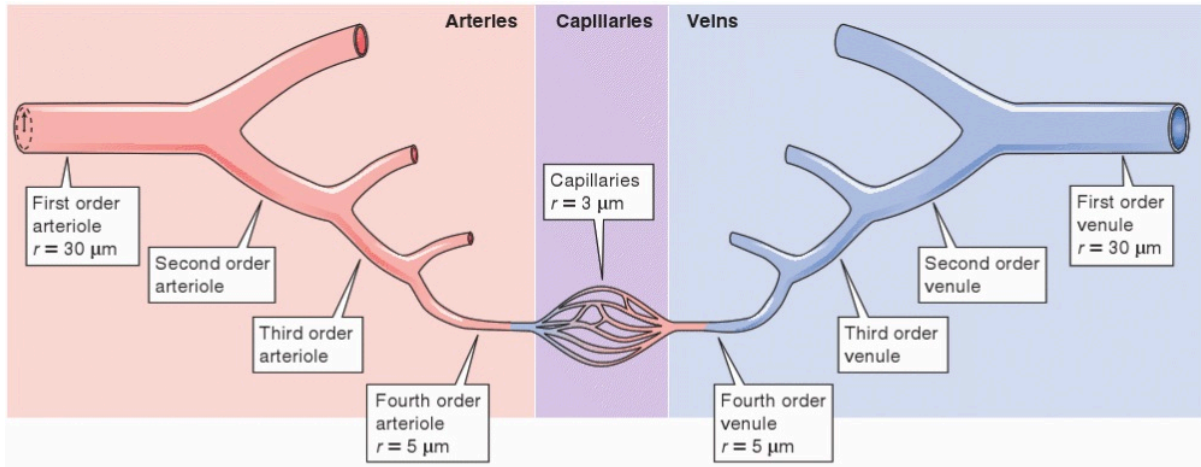


**Figure 2.6** Branching of arteries and merging of veins.  $r$  indicates the typical radius for a human at that level of arborization. Reprinted with permission from [31].

ing as blood reservoirs, are referred to as capacitance vessels. Venules and small veins outnumber their counterparts (arterioles and arteries) [29], consequently their aggregate cross-sectional area is high and aggregate resistance is low. Thus, a smaller pressure drop of 10–15 mmHg is sufficient to drive the cardiac output through the venules (Figure 2.6). At any given time, veins and venules contain about two-thirds of the circulating blood due to their abundance and size [31].

At all levels of arborization, blood vessels contract and dilate to regulate blood pressure, control blood flow within organs, and distribute blood volume throughout the body. The arterial wall alters in response to the activation of vascular smooth muscle within the wall by autonomic nerves, metabolic and biochemical signals outside the artery, and vasoactive substances released by cells that line the artery. The wall also plays a role in producing several necessary substances (nitric oxide, endothelin-1, and prostacyclin) that regulate the CVS functions, hemostasis, and inflammatory responses. More information on the synthesis and the functions of these substances can be found in [163] and [102], respectively.

## 2.2 Wall tissue

All blood vessels except capillaries have walls composed of three layers—the *tunica intima* (innermost layer), the *tunica media* (middle layer), and the *tunica adventitia* (outer layer).



It is possible to distinguish each of these layers macroscopically, as shown in Figure 2.7. Each layer is composed of particular cells serving different roles in the mechanical workings of the arterial wall. The proportion of these three layers varies depending on the size and location of the vessel as shown in Figure 2.8 and quantified in Table 2.1.

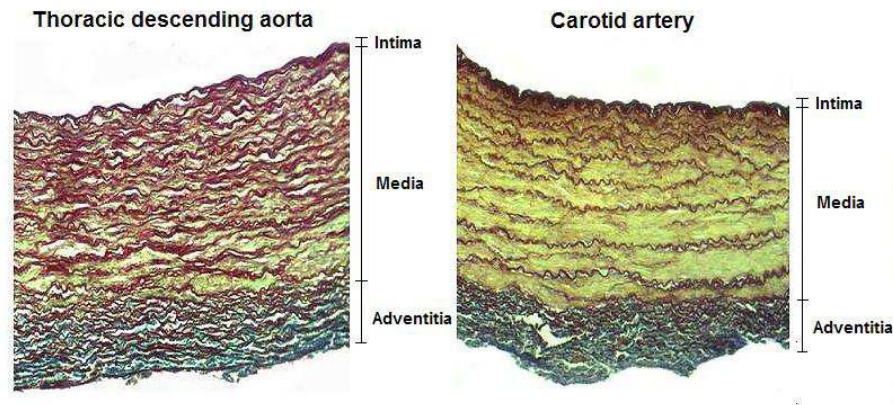


**Figure 2.7** Histological slices displaying a cross-section of the arterial wall from the ovine thoracic aorta (left) and the carotid artery (right). The vessels were stained with orcein which allows for differentiating the three main biomechanical components of the arterial wall: elastin (dark red), collagen (blue), and smooth muscle cells (yellow). The thoracic aorta has more elastin while the carotid artery contains more collagen. The difference in these compositions explains why the wall of the carotid artery appears “stiffer” than that of the thoracic aorta. Images made available by Dr. Daniel Bia, Universidad de la República, Uruguay. [26, 159]

The innermost layer, the *tunica intima*, is composed of a single layer of endothelial cells, a thin basal lamina, and a subendothelial layer. The subendothelial layer is composed of collagen, smooth muscle cells, and fibroblasts. This layer serves as the barrier that prevents plasma from seeping through the vessel wall. It also secretes many vasoactive chemicals including nitric oxide which is an antithrombotic vasodilator.

The *tunica media* is primarily composed of smooth muscle cells, arranged circumferentially and provides the mechanical strength and contractile power for the vessel. Elastin (in the form of fenestrated elastic lamellae) and collagen fibers are found in this layer of arterial walls. In humans, the number of elastic lamellae is related to the anatomical location of the artery. Muscular arteries have one internal and one external elastic lamella while the aorta has 60-90 elastic lamellae. Throughout the body, the number of lamellae



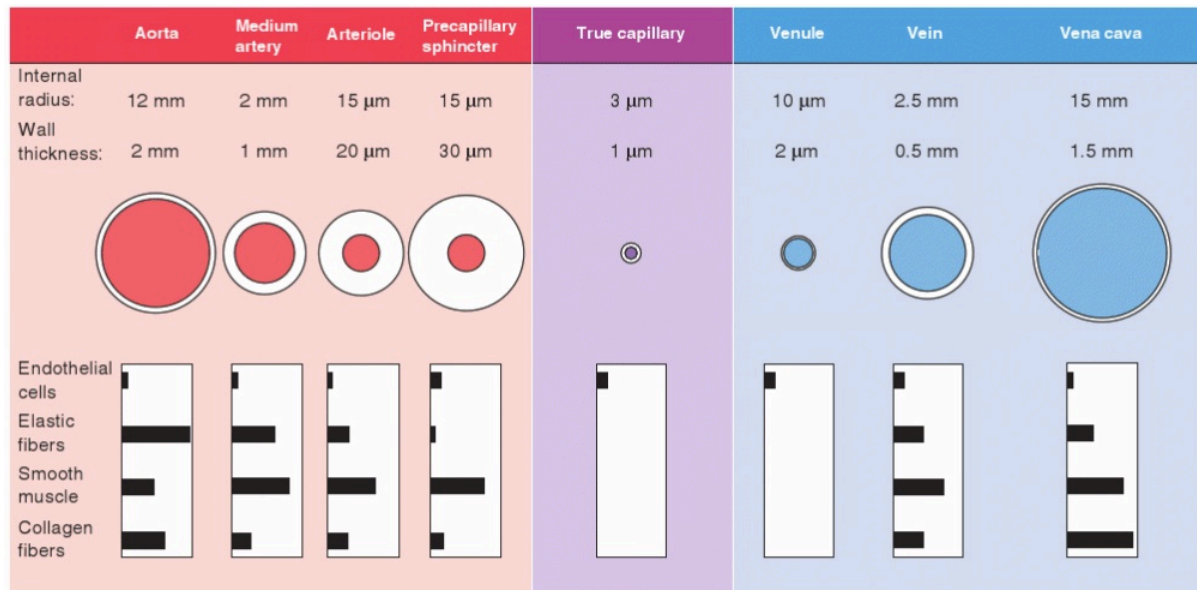


**Figure 2.8** Vascular size, wall thickness, and relative composition at different levels of arborization in human vasculature. Values for medium arteries, arterioles, venules, and veins are illustrated. It should be noted that the dimensions vary widely. Wall compositions values from specific arteries are shown in Table 2.1. Reprinted with permission from [31].

decreases toward the distal end of each arterial segment.

The *tunica adventitia*, the outermost layer of the arterial wall, is composed of dense fibroelastic tissue and has no distinct outer boundary. These fibers are responsible for releasing the vasoconstrictor agent, norepinephrin, which regulates local resistance and therefore local blood flow. In larger arteries and veins, the *adventitia* also contains *vasa vasorum* (or small blood vessels) which nourish the *media*.

### 2.2.1 Biomechanics of wall tissue

Arterial walls exhibit both *passive* and *active* deformation. Passive components, namely elastin and collagen fibers found in the *tunica media*, determine the elastic, viscous, and inertial properties exhibited by the wall. The smooth muscle contraction during vasoconstriction is the active component of the arterial wall.

*Elastin*, considered to be the primary determinant in blood flow dynamics, is six times more extensible than rubber, and it enables large arteries to serve as temporary blood storage as cross-sectional area expands by 10% during each heartbeat. This expansion occurs

**Table 2.1** Percent composition of the *media* and *adventitia* of three arteries at *in vivo* blood pressure. Values given are mean  $\pm$  standard deviation. Adapted and reproduced with permission from [55].

	Thoracic aorta	Pulmonary artery	Plantar artery
<i>Media</i>			
Smooth muscle	33 $\pm$ 10	46 $\pm$ 8	61 $\pm$ 7
Ground substance	6 $\pm$ 7	18 $\pm$ 9	26 $\pm$ 6
Elastin	24 $\pm$ 8	9 $\pm$ 3	1 $\pm$ 1
Collagen	37 $\pm$ 10	27 $\pm$ 13	12 $\pm$ 8
<i>Adventitia</i>			
Collagen	78 $\pm$ 14	63 $\pm$ 9	64 $\pm$ 10
Ground substance	11 $\pm$ 10	25 $\pm$ 8	25 $\pm$ 9
Fibroblasts	9 $\pm$ 11	10 $\pm$ 6	11 $\pm$ 3
Elastin	2 $\pm$ 3	2 $\pm$ 2	0 $\pm$ 0

to accommodate the blood ejected from each heartbeat. Stretched elastin stores mechanical energy which is used during diastole to maintain blood pressure and drive flow through the downstream resistive vessels. This mechanical energy allows blood pressure to stay above  $\sim 80$  mmHg despite the fact that the heart ejects blood intermittently with the least amount of energy expended.

Collagen, whose fibers are  $\sim 100$  times less distensible than elastin, stretches only 3 to 4% under physiological conditions. It prevents vessels from excessive expansion when blood pressure rises.

While elastin breaks down with age, collagen is built up and dominates the elastic properties of the vessels. Vessels get stiffer in a process called arteriosclerosis. This is part of the natural aging process, but vessels can also stiffen earlier and at quicker rates with the presence of cardiovascular diseases such as hypertension and diabetes [44].

Although all wall components contribute to *viscosity*, the magnitude of internal friction, smooth muscle cells in the *tunica intima* and *media* respond to physiological stimuli. Smooth muscle tone depends on blood flow, blood viscosity, and hematocrit values. Characterizing the viscous behavior of arterial walls sheds light on the physiological factors associated with plaque build-up or other arterial disease stages.

Due to the wall viscosity controlled by elastin, collagen, and smooth muscle cells, a time lag exists between applied pressure and pulsatile area waveforms, causing a hysteresis loop when pressure and area are plotted against each other [10, 107]. The time delay is

caused by the energy required to dilate a vessel during systole that is not recovered during diastole. It is common to plot and compare these loops at various locations in the body. By plotting hysteresis loops along a network, it is clear that vessels display different degrees of viscoelasticity. Wall viscosity varies depending on the state of the wall muscle and other arterial properties [26].

### 2.2.2 Vascular pathology

As discussed by Humphrey [74], the leading causes of morbidity and mortality are diseases of and injuries to the arterial vasculature. We will briefly outline the biomechanics of two common pathologies but refer the reader to [74] for further information.

#### 2.2.2.1 Hypertension

Hypertension is defined as an elevation in blood pressure from the normal 120 mmHg/ 80 mmHg. There are multiple criteria used to distinguish what constitutes an “above average” or “high” pressure [129]. In humans, systemic hypertension is typically characterized by systolic pressures greater than 160 mmHg or diastolic pressures greater than 90 mmHg. Many clinicians now diagnose “pre-hypertension” which is thought to be an intermediate stage between normal and hypertensive patients. Pre-hypertensive patients have a systolic pressure between 121–159 mmHg or a diastolic pressure between 81–90 mmHg and are at risk of becoming hypertensive.

The etiology of hypertension remains unknown [18], but accepted causes include aging, genetics, improper diet, and malfunction of major organs or nervous systems. When hypertension clearly results from another condition or disease, it is referred to as secondary hypertension. In opposition, when the cause is not due to another disease and is suspected to stem from vessel stiffening, it is referred to as primary hypertension.

As previously mentioned, within the *media*, elastin deteriorates with age and collagen becomes the dominating biomechanical substance in the arterial wall. This leads to an increase in stiffening which causes blood flow velocity to increase and reflected waves occur in sync with forward propagating waves (see Figure 2.9). This results in an augmented pressure waveform, a symptom of arterial hypertension. Hypertension is inevitable as humans age due to the deterioration of elastin. However, in other cases of hypertension, it is difficult to establish whether hypertension causes arterial stiffening or vice versa.

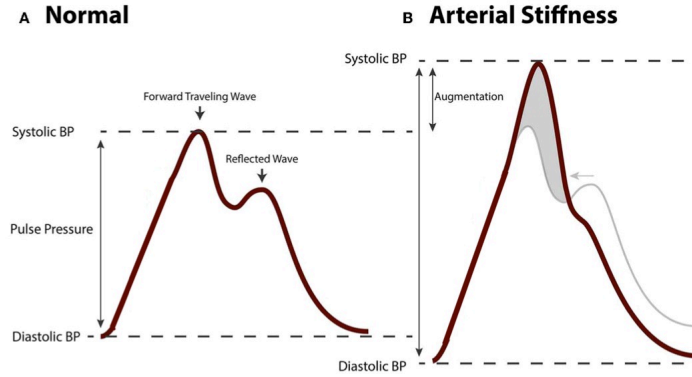


**Figure 2.9** (left) A healthy pressure waveform where the forward wave (emanating from the heart) occurs before the reflected wave (emanating from the periphery). (right) As arterial walls stiffen, pulse wave velocity increases causing the forward and backward waves to occur at the same time, augmenting the pressure waveform. Adapted and reproduced with permission from [164].

### 2.2.2.2 Arteriosclerosis

While hypertension mainly affects the *media*, arteriosclerosis is a local disease of the *intima* and the most common vascular disease overall. arteriosclerosis affects large- and medium-sized arteries, causing heart disease, stroke, and gangrene in the extremities via fatty deposits along the inner lining of the arterial wall. This affects the structure and function of blood vessels.

It has been suggested that following an insult to the endothelium and smooth muscle of the arterial wall, monocytes adhere to the local insult and migrate to the inner wall. There, they transform into macrophages and ultimately lipid foam cells. Meanwhile, smooth muscle cells are stimulated to migrate into the *intima* while calcium is accumulated locally. Between the two mechanisms aforementioned, the fatty deposits are locally deposited, typically at sites of complex geometry, and prevent normal blood flow to the downstream vasculature. This impairs the delivery of oxygen to tissues and impacts bodily function.

### 2.2.2.3 Relevant pathology

Because this dissertation focuses on one-dimensional modeling of blood flow in the arteries, we must remain realistic in the capabilities of our model. There are particular diseases which can be addressed while utilizing a one-dimensional network and those which require higher dimensions to properly study. Thus, the motivating factor for this work is

based on the uncertainty associated with causes for arterial hypertension. That said, this research mainly investigates healthy arterial networks in hopes that this will lead to improvement of tracking diseases and understanding the structural changes in vasculature associated with hypertension.

---

## Chapter 3

---

# Experimental Data

The experimental data used throughout this thesis were provided by Dr. Daniel Bia and his laboratory in the Physiology Department at the Universidad de la República in Montevideo, Uruguay and have been used by Valdez-Jasso et al. [159–162] to develop constitutive equations relating blood pressure and arterial cross-sectional area. As discussed in Section 3.1 and shown in Section 3.2, data recorded are time series measurements of arterial blood pressure and vessel diameter in ovine arteries. Measurements are taken from seven vessels in the systemic arterial network under *ex vivo* experimental conditions in eleven male Merino sheep. Section 3.3 details the literature data.

### 3.1 Experimental setup

#### 3.1.1 Surgical preparation and acquisition of segments

Details on the experiment are summarized from [26]. Blood pressure and cross-sectional area were measured in vessels excised from eleven healthy male Merino sheep, aged 18–24 months with a mean weight of 32 kg (ranging from 25–35 kg). All protocols were approved by the Research and Development Council of the Universidad de la República and were conducted in accordance with the guidelines for the care and use of laboratory animals [41]. The sheep were appropriately fed and assessed for optimal clinical status for the 30 days leading up to the surgery. General anesthesia was induced by intravenous ad-

ministration of pentobarbital (35 mg/kg). Alveolar ventilation was maintained by a respirator (Draeger SIMV Polyred 201, Madrid, Spain). Respiratory rate, tidal volume, and the inspired oxygen fraction were adjusted to maintain arterial  $p_{\text{CO}_2}$  at 35-45 millimeters of mercury (mmHg), pH at 7.35-7.4, and  $p_{\text{O}_2}$  above 80 mmHg. In each sheep, seven arteries (see Figure 7.4) were selected to evaluate their mechanical properties: the right carotid artery (CA), the brachiocephalic trunk (BT), the ascending aorta (AA), the proximal descending aorta (PD), the medial descending aorta (MD), the distal descending aorta (DD), and the left femoral artery (FA). For each vessel, a 6 cm segment (marked with suture references in the adventitia) was dissected from the surrounding tissue. Two miniature piezoelectric crystal transducers (5 MHz, 2mm in diameter) were sutured in the adventitia on opposite sides of each vessel, and the external vessel diameter was measured by converting the transit time of the ultrasonic signal (1580 m/s) between the crystals into distance by means of a sonomicrometer (1000 Hz frequency response, Triton Technology, Inc., San Diego, CA). Optimal positioning of the dimensionless gauges was assessed with an oscilloscope (model 465B, Tektronix, Richardson, TX). After marking the vessel segments, the animals were sacrificed with an intravenous overdose of pentobarbital followed by potassium chloride, and the arterial segments were excised. To limit rupture of the adventitia and endothelium, the “no-touch” technique was employed to excise and mount (in a mock circulation) the arterial segments. After completion of the excision, the correct position of the ultrasonic crystals as well as strength and adequacy of the suture were confirmed by visual inspection.

In summary, six steps were performed prior to the *ex vivo* mechanical tests [11]: 1) animals were anesthetized; 2) seven arterial segments were exposed and dissected from the surrounding tissue in each animal; 3) each arterial segment was marked with two suture references in the adventitia; 4) a pair of ultrasonic crystals was sutured into the adventitia to measure the external diameter; 5) the animals were sacrificed; and 6) the segments were excised.

### 3.1.2 *Ex vivo* experiments

As shown in Figure 3.1, the excised vessel segments were non-traumatically mounted in the organ chamber of the mock circulation, immersed and perfused with a thermally regulated (37° C) and oxygenated Tyrode’s solution with pH 7.4. The mock circulation consisted of polyethylene tubing powered by a pneumatic pump (Jarvik Model 5, Kolff Medical, Inc.,

Salt Lake City, UT). The pneumatic device was regulated via an air supply machine that allowed adjustments of hemodynamic parameter values and waveforms. The external arterial diameter was measured using sonomicrometry, employing the ultrasonic crystals sutured into the adventitia during the *in vivo* procedures. Pressure was measured with a solid-state microtransducer (Model P2.5, 1200 Hz frequency response, Konigsberg Instruments, Inc., Pasadena, CA) inserted into each artery through a small incision. This technique allows adequate and reproducible measurements of the arterial wall mechanics [10]. Pressure sensors were calibrated using a mercury manometer. To avoid signal interference, the pressure sensor was inserted 2 mm proximal to the ultrasonic crystals. Experimental pressure-area data are summarized in Figure 7.5 depicting pressure area loops for each vessel segment. These measurements are obtained by setting the inflow as mimicking the cardiac output of the individual sheep.

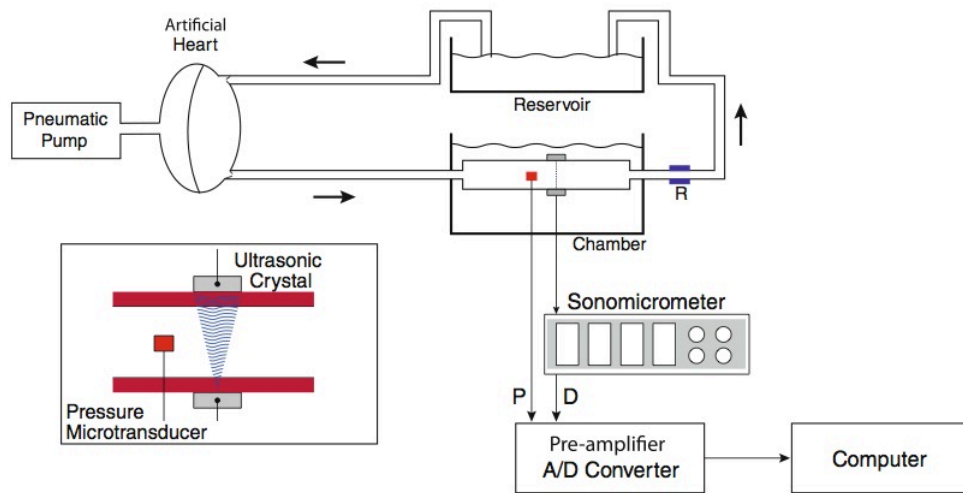


**Figure 3.1** Mock circulation including a pneumatic pump, a perfusion line connected to the chamber with the mounted vessel segment, a resistance modulator (R), and a reservoir. The chamber was filled with a thermally controlled Tyrode's solution. Pressure (p) was measured with a micro transducer while the diameter (D) was measured with a pair of ultrasonic crystals using sonomicrometry.

Lastly, a non-constricting ultrasonic perivascular flow probe connected to a transit-time ultrasonic flowmeter was positioned around each artery (Model T206, Transonic Systems, Inc., 8A, 10A, 12A, 16A, 20A, 24A Probes, Ithaca, NY) to ensure a physiological mean



flow in each arterial segment. The flow probe was positioned and the flow recording was used to adjust the Jarvik pump. Upon calibration of the pump, the flow probe was removed to avoid potential effects on the pressure and diameter signals. Flow data were not saved. Once placed in the organ chamber, each segment was allowed to equilibrate for a period of 15 minutes. After the arterial segments mounted in the *ex vivo* system were stretched to *in vivo* length, the arterial diameter was measured at zero pressure (0 mmHg) with the *ex vivo* system pump turned off (values shown in Table 7.1). Next, vessels were subjected to physiological hemodynamics conditions with a pumping frequency of 1.8 Hz [108 cycles per minute (cpm)]. The pressure and diameter signals were displayed in real time, digitized with a frequency of 200 Hz and stored for later analysis. For this study, approximately ten consecutive cardiac cycles were sampled and analyzed for each vessel. Using these measurements, the mean wall thickness given in Table 7.1 was calculated as the difference between the external radius  $r_e$  (determined by sonomicrometry) and the internal radius  $r_i$  (estimated). The internal radius (Table 7.1) was estimated from the vessel volume,  $V = \omega \rho$ , where  $\omega$  is the vessel weight (measured using a precision scale, Sartoris-Werke GMBH type 2442) and  $\rho$  is the tissue density (assumed constant as 1.06 g/mL), using the relation  $V = L(\pi r_e^2 - \pi r_i^2)$ , where  $L$  is the vessel length.

### 3.2 Data preprocessing

Pressure and radius data acquired were time series measurements over multiple cardiac cycles. We assume that the cardiac cycle is perfectly periodic in our model, and thus we compare our simulated results to a single selected cycle from the data time series. Additionally, the objective was to investigate pressure and cross-sectional area dynamics of the arterial wall as they relate to wave propagation. Pressure-area data are shown in Figure 3.2. Assuming arteries have a circular cross-sectional area, the diameter time series data  $d_j$  (in mm) was used to determine the cross-sectional area  $a_j$  (in  $\text{cm}^2$ ) via

$$a_j = \pi \left( \frac{d_j}{20} \right)^2.$$

### 3.3 Available data in literature

As aforementioned, complete data sets (blood flow, pressure, arterial cross-sectional area, and geometry) throughout the network are nonexistent. This is due to the difficulty in simultaneously and accurately measuring the three quantities ( $p, q, A$ ) at the same locations. However, many studies have been able to measure one or two of these quantities *in vivo* but at discrete locations. In the data we use (discussed previously in 3.2), we were fortunate enough to obtain both pressure and area measurements at the same location. These experiments were performed *ex vivo* after vessels were excised, causing changes in the biomechanical properties of the arterial wall [26]. There is a distinct trade-off between obtaining more data by performing *ex vivo* tests or less data where *in vivo* experiments are possible. The experiments and data available throughout blood flow literature are discussed below. It should be noted that some experiments are also performed on casted vasculature or synthesized polyurethane vessels created to mimic arteries. Because these casted or synthesized vessels do not accurately represent arterial distention, they will be neglected in this literature review.

#### 3.3.1 Pressure-area data

Early studies in the 1960s on canine subjects [22, 23, 121]. Bergel [22, 23] measured the static cross-sectional area *ex vivo* in two locations along the aorta and single recordings from the femoral and carotid arteries. This was accomplished by excising the vessels then filling them with fluid until specific pressure values were achieved at which their radii were measured. Pressures were increased at increments of 20 mmHg from 0 to 240 mmHg, noting that both ends of this range are unphysiological pressure values. A few years later, Patel et al. [121] studied the aorta in dogs both *in vivo* while under anesthesia and *ex vivo* after the vessels had been excised. They opened the chest of each dog to reveal and expose the thoracic aorta, measuring the external radius with vernier calipers. Next, the aorta was excised and placed in a chamber where pressure and area were measured by a transducer and an electric caliper, respectively. Although Thomas Young had described a relation between vessel elasticity and hemodynamics in 1808 [185], the experiments by Bergel and Patel et al. ultimately led to the first constitutive equations relating pressure and cross-sectional area over time series. Further information on constitutive equations for pressure and area will be discussed in Section 4.2.

Later, Langewouters et al. [87] studied human aortas at two locations (thoracic and abdominal) *ex vivo* by measuring diameter at incremental pressure values (0 to 180 mmHg in increments of 20 mmHg).

Armentano et al. have recorded canine aortic diameters and pressures [10] via an implanted microtransducer and ultrasonic crystals as previously described. In later work [11], human subjects' (23–45 years old) carotid arteries were tested in a similar manner post-mortem. While this used a similar setup to [10], they also performed noninvasive *in vivo* experiments on normotensive human subjects. An echographic recording was used to measure diameter while a tonometer was used to record pressure waveforms in the carotid artery.

### 3.3.2 Pressure-flow data

One study was able to measure pressure, flow, and area simultaneously in canine femoral arteries. This study, performed by Milnor and Bertram [100] in 1978, carefully records pressure and flow at the proximal and distal ends of the artery while recording the external diameter of the artery.

In her Ph.D. dissertation, Brooke Steele [147] also simulated stenoses along porcine aortas where polyester umbilical tape was tied around the descending aorta to restrict blood flow. A polyester graft was attached above and below the constriction, providing an alternate route for blood flow. Contrasted-enhanced magnetic resonance angiography (CE-MRA) was used to determine the arterial geometry while phase-contrast magnetic resonance imaging (PC-MRI) collected velocity information at four locations. Catheters were simultaneously used to record pressure above and below the graft. While this experiment set out to specifically test the effectiveness of a polyester graft in cases of aortic coarctation, it does measure all three quantities in question: area, pressure, and velocity.

Alastruey et al. [7] measured *in vivo* flow and pressure time series using a flow probe and two catheter transducers inserted in the femoral artery. Data were extracted from 10 New Zealand white male rabbits at 1 cm increments from the aortic root to the iliac to calculate the pulse wave velocity.

Many studies [43, 96, 132–134, 142] have referenced the human networks used by Noordergraaf [108], Westerhof et al. [178], and Stergiopulos et al. [149]. These networks combined have grown to include the main systemic arteries, the coronary network, and the cerebral arterial tree. This network currently boasts 103 arteries and has increased in its

**Table 3.1** Summary of data available in literature for *in vivo* or *ex vivo* pressure  $p$ , area  $A$ , and flow  $q$ . Also specified are the species and arteries from which the data is measured.

reference	$p$	$A$	$q$	<i>in vivo</i>	<i>ex vivo</i>	species	arteries (# of recordings)
[22], [23]	x	x			x	canine	aorta (2), femoral (1), carotid (1)
[121]	x	x		x	x	dogs	aorta (1)
[87]	x	x			x	human	aorta (2)
[10]	x	x			x	dog	aorta(1)
[11]	x	x		x	x	human	carotid (1)
[100]	x	x	x	x		dog	femoral (2)
[147]	x	x	x	x		pig	aorta ( $p$ : 2, $A$ : CE-MRA, $q$ : 3), graft ( $q$ : 1)
[108], [178], [149]			x	x		human	aorta (3), iliac (1), femoral (1)
[108], [178], [149]			x	x		human	carotid (2), vertebral (1), cerebral (1)
[108], [178], [149]	x			x		human	radial (1), temporal (1)
[7]	x		x	x		rabbit	aorta (~18)

complexity through numerous studies over the years. Although the network geometry is complex compared to other studies, the data available is still sparse. Pressure and flow measurements were taken from young, healthy volunteers. In one group of volunteers, volumetric flow in the systemic arteries was obtained using PC-MRI. Recordings were made for the ascending aorta, thoracic aorta, abdominal aorta, common iliac, and femoral arteries. In the second group, flow was measured in the precerebral and cerebral arteries using B-mode and color-coded duplex flow imaging. This consisted of four arteries: middle cerebral artery, vertebral artery, internal carotid artery, and common carotid artery. Only a portion of this second group was used to obtain pressure measurements on superficial arteries (radial and temporal) using tonometry.

A summary of the pressure, area, and flow data aforementioned are presented in Table 3.1.

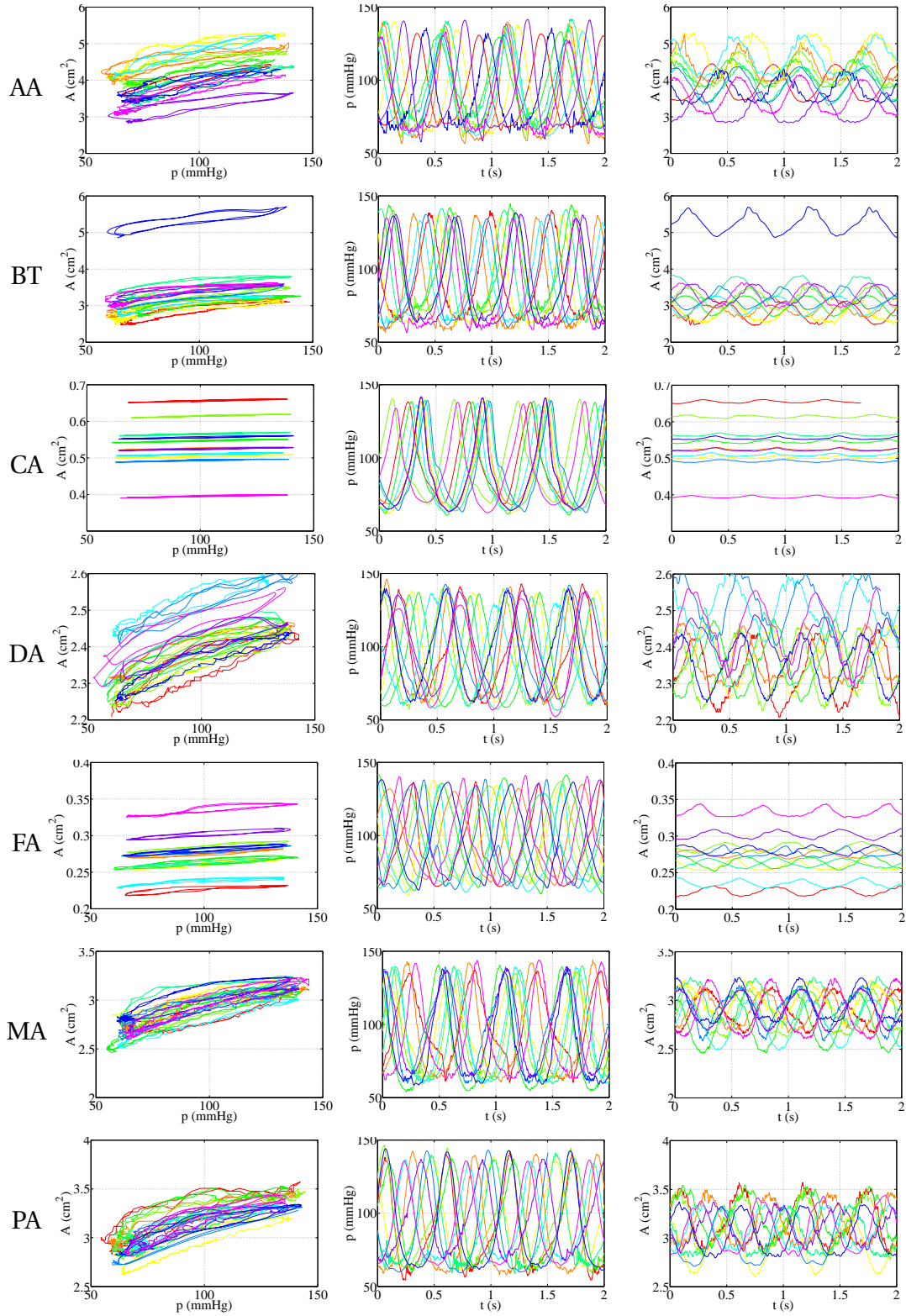


**Figure 3.2** Pressure-area, pressure time series, and area time series data from each of the seven excised vessels. Corresponding colors represent vessels from the same sheep. From top left to bottom right: AA, BT, CA, DA, FA, MA, and PA.

---

## Chapter 4

---

# Modeling Blood Flow in the Arteries

This chapter provides a literature review and derivations of the main components of the blood flow model: arterial wall models, the 1-D fluid model, and the boundary conditions. Section 4.1 presents the 1-D fluids model, Section 4.2 presents two linear wall models [55], and Section 4.3 presents various inflow and outflow boundary conditions.

### 4.1 One-dimensional fluids models

The system of equations that describes the one-dimensional (1-D) axisymmetric flow of an incompressible, Newtonian fluid consists of a conservation of mass equation, a conservation of momentum equation, and a constitutive wall model that relates pressure and area.

#### 4.1.1 Literature review

Blood flow analysis plays an important role in various forms of vascular disease; for example, pressure wave reflections alone can indicate the development of isolated systolic hypertension. However, from a clinical standpoint, it is still difficult to assess hemodynamical disorders within the arterial circulation. This renders blood flow modeling an attractive alternative and a capable method for providing crucial insight into better understanding the physiopathology of the CVS. Several modeling methodologies (0-D, 1-D, and 3-D model-

ing) have been put forward to study the CVS, each with a separate aim and ability to answer important physiological questions. 0-D studies model the CVS using a lumped parameter approach to evaluate hemodynamical interactions between organs but is unable to study wave propagation. 1-D is able to model wave propagation throughout a network and can be used to study global diseases while 3-D gives a more detailed look into the CVS and can model local diseases such as arteriosclerosis.

1-D models, known for quicker computations than 3-D models, are ideal for studying pressure and flow wave propagation throughout the arterial network. The modeling of forward and backward wave reflections can be performed using 1-D models which may help indicate cases of isolated systolic hypertension. In 1-D modeling, large systemic arteries are decomposed into arterial segments while smaller arteries and arterioles are represented by outflow boundary conditions as discussed in Section 4.3.

The 1-D theory of arterial flow was put forth by Lambert [85, 86] and attracted attention from a number of researchers including Anliker et al. [9], Hughes et al. [70], and Barnard et al. [15] who nondimensionalized the Navier-Stokes equations after experimentally observing that radial velocities are small compared with axial velocities. 1-D models of circulation have since been extensively studied to gain further insight into cardiovascular physiology and study pathologies such as hypertension [176] and arteriosclerosis [128]. Additionally, 1-D models have been used due to the ease of coupling them with 0-D models like those mimicking the left ventricle [52, 132] or distal vasculature [111].

Unlike the 1-D formulations for wave propagation, the 3-D models are based on the full Navier-Stokes equations and are appropriate to study complex flow structures in dynamic geometries. Reneman et al. [131] discussed the difficulty in modeling 3-D blood flow in arteries and was soon answered by van de Vosse et al. [171] and Taylor et al. [156, 157] and later addressed by Figueroa et al. [49]. Van de Vosse et al. [171] illustrated the potential for using finite element methods to model 3-D cardiovascular fluid-structure interactions in networks with linear elastic arterial walls. Figueroa et al. [49] then discussed a simplified algorithm that allowed for the solution of large 3-D viscoelastic cardiovascular networks while being computed in a clinically relevant time frame. Others have modeled patient-specific vessels such as healthy coronary arteries [80, 81] and aortic and cerebral aneurysms [183]. Although the 1-D analysis does not provide the same caliber of flow detail as the corresponding 3-D analysis, it is much more efficient and yields adequate information for determining how varying wall properties throughout a circulatory network impact

blood flow.

1-D models are sufficient for modeling many global phenomena in the arterial network. However, for models aiming to incorporate the effects of plaque build up or stenoses, a 3-D model would be better suited. Vignon-Clementel [165], Reymond et al. [134, 135], and Xiao et al. [182] have compared 1-D and 3-D models of the systemic arterial tree which revealed that both models are capable of capturing pressure and flow profiles. Others [21] have focused on estimating outlet boundary conditions in 3-D models.

After the early 1990s, a renewed interest in 1-D models surged because of the importance in determining both inflow and outflow boundary conditions for 3-D fluid-structure interaction problems [43, 182]. Crosetto et al. [43] utilizes the inflow flux from 1-D models in 3-D settings while Xiao et al. [182] optimized WK parameters in a 1-D setting and implemented them directly in the 3-D network.

A summary for groups that have studied 1-D and 3-D blood flow models is shown in Table 4.1.

**Table 4.1** General summary of blood flow modeling in 1-D and 3-D plus those that have studied and compared results in both dimensions.

dimension	reference
1-D	[9], [70], [85], [86], [15], [16], [174], [5], [6], [132], [54], [141], [142], [51], [128], [148], [90], [25], [57], [96]
3-D	[131], [156], [157], [171], [49], [80], [81], [183], [21]
1-D / 3-D	[165], [134], [135], [182]

## 4.1.2 Derivation of conservation laws

### 4.1.2.1 Conservation of mass

For an axisymmetric, incompressible flow ( $\vec{\nabla} \cdot \vec{u} = 0$ ) with constant density and fluid viscosity, the continuity equation in cylindrical coordinates can be written as

$$\frac{1}{r} \frac{\partial(r u_r)}{\partial r} + \frac{\partial u_x}{\partial x} = 0 \quad (4.1.1)$$



where  $r$  is the radial direction,  $x$  is the axial direction, and  $u$  is the fluid velocity. Integrating (4.1.1) over the interior cross-sectional area of the vessel where  $R$  is the internal radius results in

$$2\pi \left[ r u_r \Big|_0^R + \frac{\partial}{\partial x} \int_0^R r u_x dr \right] = 0 \quad (4.1.2)$$

where  $u_r|_R = \frac{\partial R}{\partial t}$  and the volumetric flow,  $q(x, t)$ , defined as

$$q = 2\pi \int_0^R r u_x dr \quad (4.1.3)$$

simplifying (4.1.2) to

$$2\pi R \frac{\partial R}{\partial t} + \frac{\partial q}{\partial x} = 0. \quad (4.1.4)$$

We can then substitute  $A = \pi R^2$  into (4.1.4) to obtain

$$\frac{\partial A}{\partial t} + \frac{\partial q}{\partial x} = 0, \quad (4.1.5)$$

the conservation of mass equation.

#### 4.1.2.2 Conservation of momentum

The Navier-Stokes equations in cylindrical coordinates for an incompressible fluid of constant dynamic viscosity  $\mu$  and density  $\rho$  are [32]

$$\begin{aligned} \rho \frac{D u_x}{D t} &= -\frac{\partial p}{\partial x} + \mu \Delta u_x \\ \rho \left( \frac{D u_r}{D t} - \frac{u_\theta^2}{r} \right) &= -\frac{\partial p}{\partial r} + \mu \left( \Delta u_r - \frac{u_r}{r^2} - \frac{2}{r^2} \frac{\partial u_\theta}{\partial \theta} \right) \\ \rho \left( \frac{D u_\theta}{D t} + \frac{u_r u_\theta}{r} \right) &= \frac{-1}{r} \frac{\partial p}{\partial \theta} + \mu \left( \Delta u_\theta + \frac{2}{r} \frac{\partial u_r}{\partial \theta} - \frac{u_\theta}{r^2} \right), \end{aligned}$$

where,  $u_x, u_\theta, u_r$  are the velocities in the  $x, \theta, r$  cylindrical coordinate directions,  $p$  is the pressure, and the operators  $D/Dt$  and  $\Delta$  are

$$\begin{aligned}\frac{D}{Dt} &= \frac{\partial}{\partial t} + u_r \frac{\partial}{\partial r} + \frac{u_\theta}{r} \frac{\partial}{\partial \theta} + u_z \frac{\partial}{\partial z} \\ \Delta &= \frac{\partial^2}{\partial r^2} + \frac{1}{r} \frac{\partial}{\partial r} + \frac{1}{r^2} \frac{\partial^2}{\partial \theta^2} + \frac{\partial^2}{\partial z^2}.\end{aligned}$$

Written this way, the left-hand side describes the time-dependent acceleration and the convective acceleration. Convection acceleration, in this context, refers to the time-independent rate of change of velocity due to the change in position of the fluid particles in the flow. In other words, this describes the acceleration with respect to space. The right-hand side is usually the sum of body forces and divergence of stress, both pressure and shear stress. However, we have assumed that there are no body forces acting on the vessels and thus our right-hand side is merely the pressure gradient together with viscosity.

Assuming that blood flow is axisymmetric with no swirl, we obtain

$$\frac{\partial u_x}{\partial t} + u_r \frac{\partial u_x}{\partial r} + u_x \frac{\partial u_x}{\partial x} = -\frac{1}{\rho} \frac{\partial p}{\partial x} + \nu \left[ \frac{1}{r} \frac{\partial}{\partial r} \left( r \frac{\partial u_x}{\partial r} \right) + \frac{\partial^2 u_x}{\partial x^2} \right] \quad (4.1.6)$$

$$\frac{\partial u_r}{\partial t} + u_r \frac{\partial u_r}{\partial r} + u_x \frac{\partial u_r}{\partial x} = -\frac{1}{\rho} \frac{\partial p}{\partial r} + \nu \left[ \frac{\partial^2 u_r}{\partial r^2} + \frac{1}{r} \frac{\partial u_r}{\partial r} + \frac{\partial^2 u_r}{\partial x^2} - \frac{u_r}{r^2} \right] \quad (4.1.7)$$

$$0 = -\frac{\partial p}{\partial \theta}. \quad (4.1.8)$$

Some studies chose to neglect the diffusion term in Navier-Stokes by nondimensionalizing the equations and assuming that vessel radius is much smaller than vessel length [5, 6, 9, 16, 51, 54, 128, 132, 141, 142, 174]. The work in this dissertation also follows suit, and the nondimensionalization is shown in Appendix A. Although many have neglected the diffusion term, there are still few who have incorporated the viscous effect while noting its small contribution [25, 57, 90, 96, 148].

Nondimensionalizing, we assume that  $L \gg r$  due to the natural structure of vessels (they are much longer in the axial direction than in the radial direction). From the nondimensionalization, we obtain  $u_x \gg u_r$ , which further simplifies the system. We also define  $\nu$ , the kinematic viscosity, as  $\frac{\mu}{\rho}$ .

From the nondimensionalization, (4.1.6), (4.1.7), and (4.1.8) are simplified as

$$\frac{\partial u_x}{\partial t} + u_r \frac{\partial u_x}{\partial r} + u_x \frac{\partial u_x}{\partial x} = -\frac{1}{\rho} \frac{\partial p}{\partial x} + \nu \left[ \frac{1}{r} \frac{\partial}{\partial r} \left( r \frac{\partial u_x}{\partial r} \right) \right] \quad (4.1.9)$$

$$0 = -\frac{\partial p}{\partial r} \quad (4.1.10)$$

$$0 = -\frac{\partial p}{\partial \theta}. \quad (4.1.11)$$

From (4.1.10) and (4.1.11), pressure is not a function of  $r$  but rather a function of  $x$  and  $t$  only.

Integrating (4.1.9) over the cross-sectional area gives

$$2\pi \int_0^R \left( \frac{\partial u_x}{\partial t} + u_r \frac{\partial u_x}{\partial r} + u_x \frac{\partial u_x}{\partial x} \right) r \, dr = 2\pi \int_0^R \left( -\frac{1}{\rho} \frac{\partial p}{\partial x} + \nu \left[ \frac{1}{r} \frac{\partial}{\partial r} \left( r \frac{\partial u_x}{\partial r} \right) \right] \right) r \, dr. \quad (4.1.12)$$

The first term in (4.1.12) can be simplified by using (4.1.3) as

$$2\pi \int_0^R \frac{\partial u_x}{\partial t} r \, dr = 2\pi \frac{\partial}{\partial t} \int_0^R r u_x \, dr = \frac{\partial q}{\partial t} \quad (4.1.13)$$

where  $q(x, t)$  is the volumetric flow as defined earlier. Next, integration by parts and (4.1.1) are used to simplify the second and third terms. By the no-slip condition boundary condition,  $u_x \Big|_{r=R} = 0$ . Integrating the second term by parts, we obtain:

$$2\pi \int_0^R r u_r \frac{\partial u_x}{\partial r} \, dr = -2\pi \int_0^R u_x \frac{\partial(r u_r)}{\partial r} \, dr. \quad (4.1.14)$$

Using (4.1.1), this is easily combined with the third term of (4.1.12) to obtain:

$$2\pi \int_0^R \left( u_r \frac{\partial u_x}{\partial r} + u_x \frac{\partial u_x}{\partial x} \right) r \, dr = 2\pi \int_0^R r u_x \left( \frac{\partial u_x}{\partial x} - \frac{1}{r} \frac{\partial(r u_r)}{\partial r} \right) \, dr \quad (4.1.15)$$

$$= 2\pi \int_0^R 2r u_x \frac{\partial u_x}{\partial x} \, dr \quad (4.1.16)$$

$$= 2\pi \int_0^R \frac{\partial(r u_x^2)}{\partial x} \, dr. \quad (4.1.17)$$

The right-hand side of (4.1.12) is straightforward and we ultimately find

$$\frac{\partial q}{\partial t} + 2\pi \int_0^R \frac{\partial(r u_x^2)}{\partial x} dr = -\frac{A}{\rho} \frac{\partial p}{\partial x} + 2\pi \nu R \frac{\partial u_x}{\partial r} \Big|_R. \quad (4.1.18)$$

By defining a velocity profile,  $u_x$ , these equations are further simplified. The general form for most velocity profiles is

$$u_x(r, x, t) = \frac{\gamma+2}{\gamma} U(x, t) \left( 1 - \left( \frac{r}{R(x, t)} \right)^\gamma \right) \quad (4.1.19)$$

where  $\gamma$  determines the shape of the profile itself and  $U(x, t)$  is the average axial velocity (see Figure 4.1).

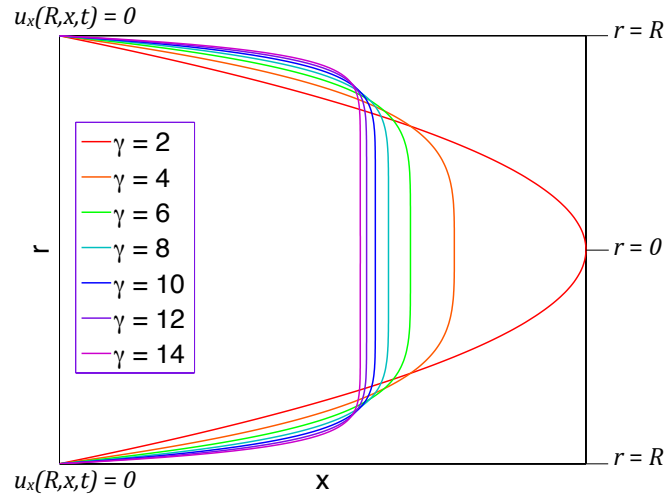


**Figure 4.1** The velocity profile for varying values of  $\gamma$  and the no-slip boundary condition inside a vessel with radius  $r$  along the axial direction  $x$ . As  $\gamma$  increases, the shape changes from a parabolic profile (corresponding to a fully developed flow) to a blunt profile (mimicking a pulsatile flow). This work assumes a parabolic profile corresponding to  $\gamma = 2$ . At a solid boundary (the arterial wall where  $r = R$ ), the blood has zero velocity relative to boundary. This is true for any time  $t$  and any  $x$  along the axial direction.

This is deemed an accurate flow profile by ensuring that the definition of volumetric

flow holds. From (4.1.3) and (4.1.19),

$$2\pi \int_0^R r u_x dr = U(x, t)A(x, t) = q(x, t).$$

Therefore, the general flow profile makes sense physically. Using the velocity profile, the terms in (4.1.18) are further simplified to

$$2\pi \int_0^R r u_x^2 dr = \left( \frac{\gamma+2}{\gamma+1} \right) U(x, t)q(x, t)$$

and

$$\frac{\partial u_x}{\partial r} \Big|_R = -(\gamma+2) \frac{U(x, t)}{R(x, t)}.$$

Thus, for a generic flow profile,

$$\frac{\partial q}{\partial t} + \left( \frac{\gamma+2}{\gamma+1} \right) \frac{\partial}{\partial x} \left( \frac{q^2}{A} \right) = -\frac{A}{\rho} \frac{\partial p}{\partial x} - 2(\gamma+2)\pi \nu \frac{q}{A} \quad (4.1.20)$$

where  $q(x, t) = U(x, t)A(x, t)$  by definition of volumetric flow. This works assumed a fully developed flow corresponding to  $\gamma = 2$ . Therefore, the equations we will solve for 1-D blood flow are

$$\begin{aligned} \frac{\partial A}{\partial t} + \frac{\partial q}{\partial x} &= 0, \\ \frac{\partial q}{\partial t} + \left( \frac{4}{3} \right) \frac{\partial}{\partial x} \left( \frac{q^2}{A} \right) &= -\frac{A}{\rho} \frac{\partial p}{\partial x} - 8\pi \nu \frac{q}{A}. \end{aligned} \quad (4.1.21)$$

## 4.2 Arterial wall models

The system of equations that describes 1-D blood flow includes a constitutive wall model relating blood pressure to arterial cross-sectional area. While there are many biomechanical properties to consider, wall models must be complex enough to capture the arterial dynamics while also simple enough to allow for rapid computation.

### 4.2.1 Literature review

As discussed in Chapter 2, the vascular wall is a heterogenous soft tissue that exhibits complex mechanical behavior due to its composition of elastin, collagen, and smooth muscle. The relative composition of these three components changes along the vasculature in health states and even more so with diseases [44]. Thus, the distention of the arterial wall and surrounding tissue is crucial in the transmission of blood flow during both normal and diseased states. To properly account for wave propagation phenomena observed in the circulatory system, the deformability of the arterial wall must be taken into account. This can be formed via a constitutive model relating strain and stress.

A material that exhibits both elastic and viscous characteristics when undergoing deformation is termed a *viscoelastic material*. In viscoelastic materials, the energy put into the system during inflation is not recovered during relaxation. This phenomenon can be found in many biological tissues; in the case of arterial walls, we see pressure-area loops signifying the energy lost through vessel dilation and contraction. Thus instead of modeling the wall with purely elastic characteristics, an alternative model can be formulated accounting for viscoelastic properties.

Viscoelasticity results in materials with memory and these materials exhibit three primary features: creep, stress relaxation, and hysteresis. Creep describes a material in continuous deformation over time when it is maintained under constant stress. Stress relaxation refers to the decrease of stress over time when it is maintained under constant strain. Lastly, hysteresis describes the dissipation of energy when a material undergoes cyclic loading and unloading. The energy dissipation associated with hysteresis makes the construction and simulation of viscoelastic networks a nontrivial matter.

The elastic properties of arteries have been studied for many years. Patel et al. [121] investigated the elastic properties of the aorta in living dogs where they concluded that vessel walls are anisotropic, an important finding that is still being researched today. Additionally, Patel et al. recorded the elasticity (or stiffness determined by Young's modulus) in the axial, radial, and tangential directions,  $E_x$ ,  $E_r$ , and  $E_\theta$ , respectively. Their findings revealed that the relative magnitudes of  $E_\theta$  and  $E_r$  were such that  $E_x$  became negligible, an assumption made in models today.

Constitutive linear elastic wall models were developed by Fung and Streeter et al. [55, 152], respectively, that correlated vessel cross-sectional area with arterial pressure, although at that time, Attinger [13] and Westerhof [177] had discussed the viscoelasticity of vascu-

lar walls. However, many, following in the footsteps of Fung, began to couple blood flow simulations with the linear elastic wall model [51, 54, 128, 139, 141, 142]. Shortly after linear elastic wall models were being used, nonlinear elastic models were developed [8, 87, 136, 160], noting that larger vessels (such as the aorta) displayed a nonlinear pressure-area relation. In particular, Fung et al. [55] proposed a strain-energy function of the exponential type while Langewouter [87] proposed an arctangent constitutive model that has been validated using *ex vivo* data sets over the years. Valdez-Jasso et al. [160] considered a sigmoidal function that accounts for saturation in the vessel wall distention at both high and low pressure values. Many of these models have been compared to data with good results. Holzapfel et al. [68] constructed a two-layer wall model that depicts the elastic and viscoelastic functions of the media and adventitia. Similarly, Alford et al. [8] developed a stress model for each component of the arterial wall—elastin, collagen, and smooth muscle cells—which shows reasonable agreement with experimental data in the aortas of rats although parameterization of this model proves to be tricky. Meanwhile Roccabianca et al. [136] employ a “four-fiber family” model that describes multiple sets of biaxial data for both human abdominal aortic aneurysms and the aging of the human abdominal aorta.

Although numerous studies have measured the arterial elasticity under static conditions, it is physiologically important to also study wall properties under dynamic conditions. When studying arteries under dynamic conditions, the viscous properties of vascular walls are observed. Gow and Taylor [59] quantified the dynamic elastic moduli as well as the viscous moduli of the arterial wall in a number of sites in living dogs. In doing so, they determined that viscoelasticity is truly necessary to capture wave propagation in large arteries such as the aorta while in smaller arteries, such as the femoral artery, viscoelasticity is not as prominent. The viscoelastic behavior of vessels, mainly attributed to smooth muscle cells, is usually described by analogous mechanical models consisting of springs and dashpots. The simplest linear viscoelastic models are the Maxwell, Voigt, and Kelvin (commonly known as the standard linear solid) models shown in Figure 4.2 and discussed in [55].

The Maxwell model, represented by a spring and a dashpot in series, is commonly used for to model fluid movement rather than solids. The Voigt model, however, is commonly used to model viscoelastic solids due to its simplicity, being composed of a spring and a dashpot in parallel [10, 11, 27, 28, 122, 173]. This particular model formulates pressure as a function of cross-sectional area or diameter, thus making it straightforward to incorporate

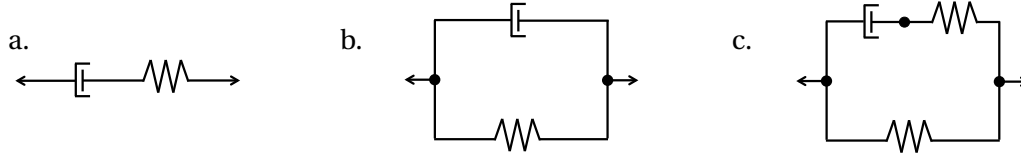


**Figure 4.2** The three simplest linear viscoelastic models composed of springs and dashpots: (a) Maxwell, (b) Voigt, and (c) Kelvin. Linear springs produce instantaneous deformations proportional to the load while dashpots slow motion, absorb energy, and produce velocity proportional to the load.

into a fluid dynamics model. The Kelvin model is composed of a Maxwell body in parallel with a spring. This model has been used as a standalone constitutive model by Balocco et al., Berglund et al., Orosz et al., and Podoltsev et al. [14, 24, 115, 122]. Yet, another study departed and based their constitutive equation on a generalized string model [51].

Recently, studies have incorporated a formulation proposed by Fung [55] and modified by Holenstein et al. [67] and Zhang et al. [186, 187] known as the quasilinear viscoelasticity theory (QLV) which characterizes the viscoelastic mechanics of arteries. QLV assumes that a viscoelastic kernel can be separated into time- and strain-dependent components [168]. In this context, QLV is tailored to model both the viscoelastic creep function of the tissue as well as the mechanical stress-strain response typically found in purely elastic models. Numerous studies have implemented linear viscoelastic walls through a QLV formulation [127, 160–162] while Valdez-Jasso et al. [162] put forward a nonlinear viscoelastic model. Text summarized in Table 4.2.

Again, both linear and nonlinear viscoelastic models are used throughout literature. For the purpose of this thesis, we will discuss only linear viscoelastic models but I have also contributed to work with nonlinear viscoelastic wall models [12].

### 4.2.2 Elastic model

This wall model assumes arterial walls are elastic which means the radius  $r$  is immediately variable with an increase in pressure  $p$ .

Laplace's law relates the circumferential stress  $\sigma_{\theta\theta}$  in the vessel wall to the fluid pressure  $p$  and the geometry of the vessel under equilibrium conditions. This law is derived by assuming a cylindrical vessel with radius  $r$  sliced in half axially along its length  $l$  and by determining the opposing forces acting on the vessel wall. In a state of equilibrium, the



**Table 4.2** Summary of wall models studied by different groups.

linear	nonlinear	elastic	viscoelastic	QLV	reference
x		x			[55], [152], [128], [54], [141], [142], [51], [139]
	x	x			[87], [136], [8], [160]
x		x	x		[68]
x		x	x		[8]
	x	x	x		[136]
x			x		[122], [28], [27], [10], [11], [173], [14], [24], [115], [122]
x			x	x	[55], [67], [186], [187], [168], [127], [160], [161]
	x		x	x	[162]

opposing forces must balance each other.

The outward force,  $F_{outward}$ , acting on the upper half of the vessel is the product of pressure  $p$  and the projected area of the cylindrical wall. Thus,  $F_{outward} = 2prl$ . The inward force,  $F_{inward}$ , that pulls the two halves of the vessel together is due to circumferential stress  $\sigma_{\theta\theta}$  acting along the vessel wall. Therefore  $F_{inward} = 2\sigma_{\theta\theta}lh$  where  $h$  is the wall thickness and the factor of 2 comes from the two walls in the cross-section. These forces are displayed in Figure 4.3. From the balance of  $F_{outward}$  and  $F_{inward}$ ,

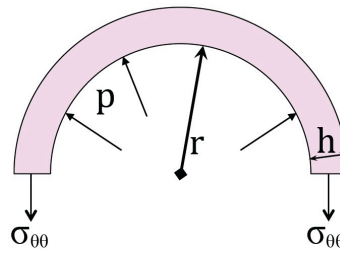


**Figure 4.3** A diagram of the forces acting on a vessel under static equilibrium conditions. The  $F_{outward}$  is due to blood pressure acting on the interior wall of the vessel and  $F_{inward}$  is the force acting on the exterior of the wall. This is the cross-sectional area of half of a vessel with length  $l$ .

$$F_{outward} = F_{inward}$$

$$2plr = 2\sigma_{\theta\theta}lh$$

$$pr = \sigma_{\theta\theta}h.$$

Therefore, circumferential stress of the vessel wall is given by

$$\sigma_{\theta\theta} = \frac{pr}{h}. \quad (4.2.1)$$

The circumferential strain  $\epsilon_{\theta\theta}$  describes the fractional circumferential distention of the arterial wall. It is defined as

$$\begin{aligned} \epsilon_{\theta\theta} &= \frac{2\pi r - 2\pi r_0}{2\pi r_0} \\ &= \frac{r - r_0}{r_0} \end{aligned} \quad (4.2.2)$$

where  $r_0$  is the initial cross-sectional vessel radius  $r$  corresponding to zero pressure. This is an assumption of the model based on [111].

Assuming that arteries can be modeled as a linear isotropic elastic material, the circumferential stress and strain can be related according to

$$\epsilon_{\theta\theta} = \frac{\sigma_{\theta\theta} - \nu\sigma_{rr} - \nu\sigma_{xx}}{E} \quad (4.2.3)$$

where  $\sigma_{rr}$  is the normal stress in the radial direction,  $\sigma_{xx}$  is the normal stress in the longitudinal direction,  $\nu$  is Poisson's ratio, and  $E$  is Young's modulus. Because we aim to mimic our blood vessels under in vivo conditions in which vessels are tethered longitudinally, we can neglect deformations in the axial direction. By doing so, we obtain  $\sigma_{xx} \approx 0$ ; the stress in the longitudinal direction is approximately zero. In addition, the arterial wall is assumed to be thin and thus  $\sigma_{rr} \ll \sigma_{\theta\theta}$ . Therefore, the stress-strain relationship in (4.2.3) can be approximated by

$$\epsilon_{\theta\theta} = \frac{\sigma_{\theta\theta}}{E}. \quad (4.2.4)$$

Substituting  $\sigma_{\theta\theta}$  and  $\epsilon_{\theta\theta}$  into (4.2.4) using (4.2.1) and (4.2.2) respectively, we obtain a

stress-strain relation in terms of vessel geometry:

$$\frac{r - r_0}{r_0} = \frac{p r}{h E},$$

which can be rearranged to yield

$$\begin{aligned}\frac{r - r_0}{r} &= \frac{r_0}{E h} p \\ 1 - \frac{r_0}{r} &= \frac{r_0}{E h} p \\ 1 - \sqrt{\frac{A_0}{A}} &= \frac{r_0}{E h} p.\end{aligned}$$

This can be rewritten as

$$p = \frac{E h}{r_0} \left( 1 - \sqrt{\frac{A_0}{A}} \right) \quad (4.2.5)$$

where  $A_0 = \pi r_0^2$  and  $A = \pi r^2$ . Thus, (4.2.5) gives the pressure-area elastic relation. Here,  $E h$  together represents the effective elastic modulus. This term allows us to vary the stiffness in each of the vessels in our system. Physiologically, vessels with smaller radii are stiffer than larger vessels, i.e. the elastic modulus is higher in smaller arteries.

### 4.2.3 Viscoelastic model

A material that exhibits both elastic and viscous characteristics when undergoing deformation is termed a *viscoelastic material*. In viscoelastic materials, the energy put into the system during inflation is not recovered during relaxation. This phenomenon can be found in many biological tissues; in the case of arterial walls, we see pressure-area loops signifying the energy lost through vessel dilation and contraction. Thus instead of modeling the wall with purely elastic characteristics, an alternative model can be formulated with viscoelastic properties.

Viscoelasticity is a property in which strain depends on the history of stress (or vice versa). Therefore, viscoelasticity results in materials with memory and these materials exhibit three primary features: creep, stress relaxation, and hysteresis. Creep describes a material in continuous deformation over time when it is maintained under constant stress. Stress relaxation refers to the decrease of stress over time when it is maintained under

constant strain. Lastly, hysteresis describes the dissipation of energy when a material undergoes cyclic loading and unloading. The energy dissipation associated with hysteresis makes the construction and simulation of viscoelastic networks a nontrivial matter.

Again, both linear and nonlinear viscoelastic models are used throughout literature. For the purpose of this thesis, we will discuss only linear viscoelastic models but I've contributed to work with nonlinear viscoelastic wall models [12].

Next, consider a linear viscoelastic model represented by a circuit of springs and dashpots, where the springs represent the elastic elements of the wall and the dashpots correspond to the viscoelastic elements. The Kelvin model—the simplest viscoelastic model that captures the effects of creep, stress relaxation, and hysteresis—uses an exponential creep function and a linear elastic response to define the wall model. The other models (shown in Figure 4.2) do not account for the energy dissipation subject to cyclic change. For this reason, we utilize the Kelvin model in formulating the viscoelastic arterial wall model. This model is shown in detail in Figure 4.4.

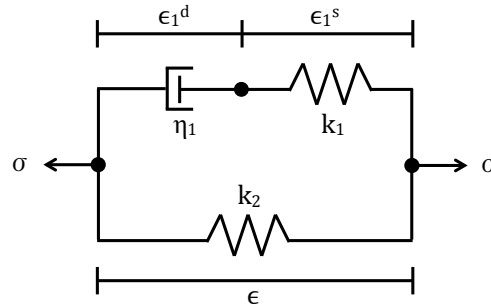


**Figure 4.4** The Kelvin viscoelastic model illustrated using mechanical analogs with a combination of two Hookean elastic springs and a dashpot. Here,  $k_1$  and  $k_2$  are the spring constants,  $\eta_1$  is the damping coefficient of the dashpot, and  $\epsilon$  is the displacement due to the loading force  $\sigma$ .

The relationships between the loading forces  $\sigma$  and displacement  $\epsilon$  acting on the springs

and dashpot (superscripts  $s$  and  $d$ , respectively) are

$$\sigma_1^s = k_1 \epsilon_1^s \quad (4.2.6)$$

$$\sigma_1^d = \eta_1 \dot{\epsilon}_1^d \quad (4.2.7)$$

$$\sigma_2^s = k_2 \epsilon \quad (4.2.8)$$

$$\epsilon = \epsilon_1^s + \epsilon_1^d \quad (4.2.9)$$

$$\sigma = \sigma_1^s + \sigma_2^s \quad (4.2.10)$$

$$\sigma_1^s = \sigma_1^d. \quad (4.2.11)$$

The springs obey Hooke's Law with spring coefficients  $k_1$  and  $k_2$  and the damping coefficient of the dashpot is  $\eta_1$ .

From (4.2.6), (4.2.8), and (4.2.10), the effects of the springs can be described by

$$\epsilon_1^s = \frac{\sigma}{k_1} - \frac{k_2}{k_1} \epsilon. \quad (4.2.12)$$

Solving for  $\epsilon_1^s$  in (4.2.6) and using (4.2.7), (4.2.9), and (4.2.11), the spring and dashpot displacements can be written as

$$\epsilon_1^s = \frac{\sigma_1^s}{k_1} = \frac{\sigma_1^d}{k_1} = \frac{\eta_1}{k_1} \dot{\epsilon}_1^d = \frac{\eta_1}{k_1} (\dot{\epsilon} - \dot{\epsilon}_1^s). \quad (4.2.13)$$

From (4.2.12) and (4.2.13) together, we obtain

$$\begin{aligned} \frac{\eta_1}{k_1} (\dot{\epsilon} - \dot{\epsilon}_1^s) &= \frac{\sigma}{k_1} - \frac{k_2}{k_1} \epsilon. \\ \frac{\eta_1}{k_1} \left( \dot{\epsilon} - \frac{\dot{\sigma}}{k_1} + \frac{k_2}{k_1} \dot{\epsilon} \right) &= \frac{\sigma}{k_1} - \frac{k_2}{k_1} \epsilon. \\ k_2 \epsilon + \eta_1 \left( 1 + \frac{k_2}{k_1} \right) \dot{\epsilon} &= \sigma + \frac{\eta_1}{k_1} \dot{\sigma}. \end{aligned} \quad (4.2.14)$$

Defining new constants

$$\tau_1 = \frac{\eta_1}{k_2} \left( 1 + \frac{k_2}{k_1} \right) \quad (4.2.15)$$

$$\tau_2 = \frac{\eta_1}{k_1} \quad (4.2.16)$$

$$W = k_2,$$

simplifies the Kelvin model

$$\epsilon + \tau_1 \dot{\epsilon} = \frac{1}{W} (\sigma + \tau_2 \dot{\sigma}). \quad (4.2.17)$$

Here,  $\tau_1$  is the relaxation time for constant stress,  $\tau_2$  is the relaxation time for constant strain, and  $W$  is the material modulus. It should be noted that  $\tau_1 > \tau_2$  by (4.2.15) and (4.2.16). In (4.2.17), the displacement  $\epsilon$  can be thought of as vessel distention  $\varepsilon$  and the force  $\sigma$  can be considered equivalent to blood pressure  $p$  in the artery. Assuming that the arterial wall behaves as a linear elastic thin-walled tube, the material modulus can be replaced by  $Wh/r_0$ , where  $Wh$  is the elastic modulus. By these assumptions, the Kelvin model can be related to the linear elastic model (Section 4.2.2)

$$\varepsilon(t) + \tau_1 \frac{d\varepsilon}{dt} = \frac{r_0}{Wh} \left( p(t) + \tau_2 \frac{dp}{dt} \right) \quad (4.2.18)$$

$$\varepsilon(t) = \left( 1 - \sqrt{\frac{A_0}{A(t)}} \right). \quad (4.2.19)$$

Hence, the four independent parameters that define the Kelvin viscoelastic model are  $\theta = \{r_0, Wh, \tau_1, \tau_2\}$ .

Equation (4.2.18) relates blood pressure to strain and their respective first-order derivatives. However, this formulation requires the differentiation of both strain and pressure, and additionally, the differential form of the Kelvin model does not provide a clear framework for further extension of the model. The Kelvin model can therefore be rewritten in an equivalent integral form which allows for prediction of arterial wall deformation using blood pressure as an input. We can obtain the integral form of (4.2.18) by using an integrat-

ing factor method and integrating from an arbitrary time  $t_0$  to the current time  $t$ .

$$\begin{aligned}
\varepsilon(t) + \tau_1 \frac{d\varepsilon}{dt} &= \frac{r_0}{Eh} \left( p + \tau_2 \frac{dp}{dt} \right) \\
e^{t/\tau_1} \left( \frac{1}{\tau_1} \varepsilon(t) + \frac{d\varepsilon}{dt} \right) &= e^{t/\tau_1} \frac{r_0}{Eh} \frac{1}{\tau_1} \left( p + \tau_2 \frac{dp}{dt} \right) \\
\int_{t_0}^t \frac{d}{d\zeta} \left( e^{\zeta/\tau_1} \varepsilon(\zeta) \right) d\zeta &= \int_{t_0}^t e^{\zeta/\tau_1} \frac{r_0}{Eh} \frac{1}{\tau_1} \left( p + \tau_2 \frac{dp}{d\zeta} \right) d\zeta \\
\varepsilon(t) e^{t/\tau_1} - \varepsilon(t_0) e^{t_0/\tau_1} &= \frac{r_0}{Eh} \frac{1}{\tau_1} \int_{t_0}^t e^{\zeta/\tau_1} \left( p + \tau_2 \frac{dp}{d\zeta} \right) d\zeta \\
\varepsilon(t) e^{t/\tau_1} - \varepsilon(t_0) e^{t_0/\tau_1} &= \frac{r_0}{Eh} \frac{1}{\tau_1} \int_{t_0}^t e^{\zeta/\tau_1} p d\zeta + \frac{r_0}{Eh} \frac{\tau_2}{\tau_1} \int_{t_0}^t e^{\zeta/\tau_1} \frac{dp}{d\zeta} d\zeta \quad (4.2.20)
\end{aligned}$$

Using integration by parts, we find the last term in (4.2.20) becomes

$$\int_{t_0}^t e^{\zeta/\tau_1} \frac{dp}{d\zeta} d\zeta = (p(t) e^{t/\tau_1} - p(t_0) e^{t_0/\tau_1}) - \frac{1}{\tau_1} \int_{t_0}^t p(\zeta) e^{\zeta/\tau_1} d\zeta,$$

which gives the integral form of the Kelvin model as

$$\varepsilon(t) = e^{(t_0-t)/\tau_1} \left( \varepsilon(t_0) - \frac{r_0}{Eh} \frac{\tau_2}{\tau_1} p(t_0) \right) + \frac{r_0}{Eh} \frac{\tau_2}{\tau_1} p(t) + \frac{r_0}{Eh} \frac{\tau_1 - \tau_2}{\tau_1^2} \int_{t_0}^t e^{(\zeta-t)/\tau_1} p(\zeta) d\zeta. \quad (4.2.21)$$

Thus we find that at any given time  $t$ , strain is described in terms of the initial and instantaneous response of the vessel in addition to a term that captures the history of the pressure. This term is represented by the integral of the weighted pressure data up through the current time. Because we aim to capture the *in vivo* conditions, it is impossible to achieve a zero-strain state and thus  $t_0$  instead corresponds to an intermediate state of vessel deformation.

#### 4.2.4 Quasilinear viscoelasticity theory

In order to develop and utilize a generalized wall model that can be used to implement different properties, we turn to the quasilinear viscoelasticity (QLV) theory developed by Y. C. Fung [55]. The QLV formulation for viscoelastic materials relates strain to stress via

$$\varepsilon(t) = \int_{t_0}^t K(t-\zeta) \frac{ds^{(e)}[p(\zeta)]}{d\zeta} d\zeta, \quad (4.2.22)$$

noting that Fung sets  $t_0 = -\infty$ . Using the QLV framework, we will first determine the corresponding creep function and inverse elastic response for the Kelvin viscoelastic model. Section 4.2.4.2 expands the QLV framework to a more generalized formation for viscoelastic models, incorporating the creep function and the inverse elastic response functions as shown above.

##### 4.2.4.1 Kelvin viscoelastic model in QLV formulation

To implement the integral form of the Kelvin model in the QLV formation, the last term of (4.2.21) can be represented in terms of its pressure derivative. Thus we have (from integration by parts)

$$\begin{aligned} \int_{t_0}^t e^{(\zeta-t)/\tau_1} p(\zeta) d\zeta &= \tau_1 p(\zeta) e^{(\zeta-t)/\tau_1} \Big|_{t_0}^t - \int_{t_0}^t \tau_1 e^{(\zeta-t)/\tau_1} \frac{dp(\zeta)}{d\zeta} d\zeta \\ &= \tau_1 p(t) - \tau_1 p(t_0) e^{(t_0-t)/\tau_1} - \tau_1 \int_{t_0}^t e^{(\zeta-t)/\tau_1} \frac{dp(\zeta)}{d\zeta} d\zeta. \end{aligned}$$

Therefore, the Kelvin model in terms of the pressure derivative is

$$\varepsilon(t) = \varepsilon(t_0) e^{(t_0-t)/\tau_1} + \frac{r_0}{Eh} p(t) - \frac{r_0}{Eh} p(t_0) e^{(t_0-t)/\tau_1} - \frac{r_0}{Eh} \frac{\tau_1 - \tau_2}{\tau_1} \int_{t_0}^t e^{(\zeta-t)/\tau_1} \frac{dp(\zeta)}{d\zeta} d\zeta \quad (4.2.23)$$

From the Fundamental Theorem of Calculus Part II,

$$\int_{t_0}^t \frac{dp(\zeta)}{d\zeta} d\zeta = p(t) - p(t_0) \quad \text{and therefore} \quad p(t) = \int_{t_0}^t \frac{dp}{d\zeta} d\zeta + p(t_0),$$



which can be used to simplify (4.2.23). Thus, (4.2.23) becomes

$$\varepsilon(t) = \varepsilon(t_0)e^{(t_0-t)/\tau_1} - \frac{r_0}{Eh}p(t_0)e^{(t_0-t)/\tau_1} + \frac{r_0}{Eh}p(t_0) + \frac{r_0}{Eh} \int_{t_0}^t \left(1 - \frac{\tau_1 - \tau_2}{\tau_1} e^{(\zeta-t)/\tau_1}\right) \frac{dp(\zeta)}{d\zeta} d\zeta. \quad (4.2.24)$$

The corresponding creep function and inverse elastic response in the QLV form can be determined from (4.2.24):

$$\begin{aligned} \varepsilon(t) &= \frac{r_0}{Eh} \int_{t_0}^t \left(1 - \frac{\tau_1 - \tau_2}{\tau_1} e^{(\zeta-t)/\tau_1}\right) \frac{dp(\zeta)}{d\zeta} d\zeta \\ &= \int_{t_0}^t \left(1 - \frac{\tau_1 - \tau_2}{\tau_1} e^{(\zeta-t)/\tau_1}\right) \frac{d}{d\zeta} \left(\frac{r_0}{Eh} p(\zeta)\right) d\zeta. \end{aligned} \quad (4.2.25)$$

In rewriting (4.2.25), the creep and inverse elastic response functions are, respectively,

$$K(t) = 1 - \frac{\tau_1 - \tau_2}{\tau_1} e^{-t/\tau_1}, \quad s^{(e)}[p] = \frac{r_0}{Eh} p \quad (4.2.26)$$

with the relation between stress and area,

$$\varepsilon(t) = 1 - \sqrt{\frac{A_0}{A(t)}}.$$

To simplify this further, let  $A_1$  and  $b_1$  be defined as

$$A_1 = \frac{\tau_1 - \tau_2}{\tau_1} \quad \text{and} \quad b_1 = \tau_1$$

which results in  $K(t) = 1 - A_1 e^{-t/b_1}$ . Note that  $0 \leq A_1 < 1$  since  $\tau_1 > \tau_2$  as previously discussed, and  $A_1 = 0$  refers to a purely elastic wall model.  $A_1$  and  $b_1$  will henceforth be considered the viscoelastic parameters.

#### 4.2.4.2 Generalized QLV formulation for viscoelastic models

To consolidate various viscoelastic models into a generalized form, define the elastic response starting from a positive time,  $t_0$  such that

$$s^{(e)}[p(t)] = \begin{cases} \tilde{s}^{(e)}[p(t)] & : t \geq t_0 \\ 0 & : t < t_0 \end{cases}. \quad (4.2.27)$$

This can equivalently be written as

$$s^{(e)}[p(t)] = \tilde{s}^{(e)}[p(t)] H(t - t_0) \quad (4.2.28)$$

where  $H(t)$  is the Heaviside step function. Using (4.2.28) in Fung's original formulation

$$\begin{aligned} \varepsilon(t) &= \int_{t_0}^t K(t - \zeta) \frac{d}{d\zeta} (\tilde{s}^{(e)}[p(\zeta)] H(\zeta)) d\zeta \\ &= \int_{t_0}^t K(t - \zeta) H(\zeta) \frac{d\tilde{s}^{(e)}[p(\zeta)]}{d\zeta} d\zeta + \int_{t_0}^t K(t - \zeta) \tilde{s}^{(e)}[p(\zeta)] \frac{dH(\zeta)}{d\zeta} d\zeta \\ &= \int_{t_0}^t K(t - \zeta) \frac{ds^{(e)}[p(\zeta)]}{d\zeta} d\zeta + \int_{t_0}^t K(t - \zeta) \tilde{s}^{(e)}[p(\zeta)] \delta(\zeta - t_0) d\zeta \end{aligned} \quad (4.2.29)$$

$$= \int_{t_0}^t K(t - \zeta) \frac{ds^{(e)}[p(\zeta)]}{d\zeta} d\zeta + K(t - t_0) s^{(e)}[p(t_0)] \quad (4.2.30)$$

by properties of the Heaviside step and the Dirac delta functions. Using integration by parts, the remaining integral found in (4.2.30) can be written as

$$\int_{t_0}^t K(t - \zeta) \frac{ds^{(e)}[p(\zeta)]}{d\zeta} d\zeta \Rightarrow \begin{cases} u = K(t - \zeta), & du = -K'(t - \zeta) d\zeta \\ v = s^{(e)}[p(\zeta)], & dv = \frac{ds^{(e)}[p(\zeta)]}{d\zeta} \end{cases}. \quad (4.2.31)$$

Thus, this integral becomes

$$\begin{aligned}
\int_{t_0}^t K(t-\zeta) \frac{ds^{(e)}[p(\zeta)]}{d\zeta} d\zeta &= K(t-\zeta) \Big|_{t_0}^t + \int_{t_0}^t K'(t-\zeta) s^{(e)}[p(\zeta)] d\zeta \\
&= K(0)s^{(e)}[p(t)] - K(t-t_0)s^{(e)}[p(t_0)] + \int_{t_0}^t K'(t-\zeta)s^{(e)}[p(\zeta)] d\zeta.
\end{aligned} \tag{4.2.32}$$

Re-evaluating (4.2.30), the strain is given by

$$\varepsilon(t) = K(0)s^{(e)}[p(t)] + \int_{t_0}^t K'(t-\zeta)s^{(e)}[p(\zeta)] d\zeta. \tag{4.2.33}$$

This allows for the formulation of new viscoelastic wall models based on creep function  $K(t)$  and elastic response function  $s^e[p(t)]$ . This current works utilizes the Kelvin linear model previously derived although a nonlinear viscoelastic wall model [162] has been implemented and used in collaborative efforts [12]. Current work has studied one creep function ( $K(t) = 1 - A_1 e^{-t/b_1}$ ) while the elastic response function changes based on linear or nonlinear relationships between area and pressure. The two models studied in this dissertation are presented in Table 4.3.

**Table 4.3** Two linear wall models written in QLV formulation with creep function  $K(t)$  and inverse elastic response function  $s^{(e)}[p]$ . Note that the creep function distinguishes between elastic and viscoelastic.

model	$K(t)$	$s^{(e)}[p(t)]$
linear elastic	1	$\frac{r_0}{Eh}p(t)$
Kelvin viscoelastic	$1 - A_1 e^{-t/b_1}$	$\frac{r_0}{Eh}p(t)$

## 4.3 Boundary conditions

The model given by (4.1.21) and (4.2.33) forms a system of hyperbolic quasilinear first-order partial differential equations. Quasilinear first-order partial differential equations have the form

$$\frac{\partial \mathbf{U}}{\partial t} + \tilde{\mathbf{A}} \frac{\partial \mathbf{U}}{\partial x} = \tilde{\mathbf{B}} \quad (4.3.1)$$

where  $\mathbf{U} = [p, q]^\top$ ,  $p$  is a function of  $A$ , and  $\tilde{\mathbf{A}}$  and  $\tilde{\mathbf{B}}$  are functions of  $(x, t)$  and  $\mathbf{U}$  [111]. A system is then termed hyperbolic if  $\tilde{\mathbf{A}}$  is diagonalizable. This was shown for the linear elastic wall model in Olufsen's dissertation [111] and for the Kelvin linear viscoelastic wall model in DeVault's dissertation [45]. See Appendix C for more details.

Due to the large number of tiny vessels in the arterial network, it is imperative to truncate geometries at the small arteries to reduce complexity and computational cost. At these terminal truncation points, outlet boundary conditions are applied to account for the resistance and wave propagation in the downstream vasculature. In modeling 1-D blood flow, there are three commonly used outflow boundary conditions: a pure resistor boundary condition, a structured tree model, or a Windkessel model. It has been noted that the choice in outflow boundary condition can greatly affect the upstream results. We will implement a 3-element Windkessel model at our boundaries, but for completion, we will briefly discuss historically used alternative methods.

### 4.3.1 Literature review

*Pure resistor.* At terminal boundaries, the simplest condition imposed is a pure resistor boundary, implemented in [9, 50, 105, 110, 138, 142, 174]. This model was popular circa 1960-1980 and assumed the pressure was proportional to the blood flow rate,  $P = RQ$  where  $R$  is a constant but has a specific value at each outlet. Assuming pressure and flow rate to be proportional causes them to be in phase, an unphysiological approximation. Additionally, this method ignored the arterial wall compliance, thus producing a large, non-physical wave reflection of blood flow and producing suboptimal results from a physiological standpoint [47].

*Windkessel models.* Lumped models, such as the Windkessel (WK), are the most popular used to represent the blood flow and pressure in the downstream vasculature [113]. Electrical circuits have been the basis for these lumped models, providing a straightfor-

ward analogy where current represents arterial blood flow and voltage represents arterial pressure. Resistive units become analogous to arterial and peripheral resistances occurring as a result of viscous dissipation while capacitors represent the volumetric compliance of the vessels which allows them to store large amounts of blood. Inductors, when present, represent the inertia of blood.

The WK model was originally developed by Stephen Hales in 1733 [66] and formalized by Otto Frank in 1899 [53]. Hales described his theory on blood flow in the heart and systemic arteries, basing this theory on an observation of an old fire engine with a pump fire hose (see Figure 4.5). The German word “Windkessel” translates as “air chamber” but has been taken to imply an elastic reservoir. When the air chamber is full, high pressure drives the water out in a constant stream, analogous to the left ventricle where the blood pressure ranges from low (nearly 0 mmHg) to a high of approximately 120 mmHg, at which point the blood is ejected into the aorta. The analogy presented by Hales resulted in the quantitative formulation by Frank of the two-element WK model, consisting of a single resistor and a single capacitor in parallel. This model can also be used to describe blood flow in the systemic arteries without explicitly including the heart, even though it was intended to model the ventricle and the aorta. Without the heart, the two elements, capacitor and resistor, represent the compliance of large arteries and the resistance of small arteries and arterioles, respectively. Until this point, hypertension research focused mainly on peripheral resistance while neglecting arterial compliance. However, in 1997, it was shown that another major predictor of cardiovascular function is pulse pressure [20, 101]. This observation revealed the importance of arterial compliance, particularly in cases of hypertension associated with aging. Similarly, 0-D lumped parameter models relating pressure and flow are based on WK elements.

This two-element WK model explained aorta pressure decay during diastole but fell short in representing pressure during systole, and therefore it was soon extended into a three-element model which adds an extra resistor into the circuit. It is thought that this resistor represents the characteristic impedance of the large compliance vessels, namely the aorta. The three-element WK model produces realistic blood flow and pressure waveforms and provides a good fit to experimental data but has been shown to overestimate arterial compliance and underestimate aortic characteristic impedance [140]. Further expansion into a four-element model has proven to be slightly more accurate [84], amending the previous model by introducing an inductor. However, Westerhof et al. [179] has discussed the

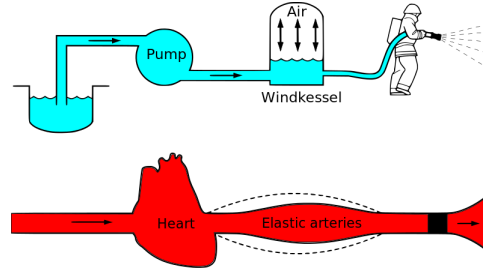


**Figure 4.5** The WK analogy. The heart (pump) delivers blood (water) to the distensible arteries (air chamber) which act as a reservoir until a high pressure drives the blood (water) further downstream. Image created for Wikipedia Commons by Kurzon.

shortcomings of the four-element model, namely that the inertance of blood is very difficult to estimate and that an argument can be made to prefer the three-element WK. Segers et al. [140] has also discussed how increasing the WK model complexity improves fitting results but at the cost of parameters being less physiologically defined. For this reason, the three-element WK model continues to be the most common, useful, and simplistic terminal boundary condition for small vessels with each element maintaining a physiological significance.

*Structured tree.* The structured tree was introduced by Olufsen [111]. This approach truncates the arterial network after the first few generations of large arteries and the remaining small arteries and arterioles provide outflow boundary conditions for the upstream large arteries [111, 112, 114]. Small arteries and arterioles are modeled by a binary asymmetric structured tree where each vessel in the tree is considered as a straight, compliant tube. However, the structured tree bases geometry on general statistical relationships based on literature values. Geometry is based on the parent vessel radius  $r_p$  with the radii of the left- and right-daughter vessels set as  $r_L = \alpha r_p$  and  $r_R = \beta r_p$ , respectively, where  $\alpha$  and  $\beta$  are bifurcation ratios with  $\beta = (1 - \alpha^\xi)^{1/\xi}$  given by Murray's law where typically  $\xi \approx 3$ . The length of each vessel segment is proportional to the radius such that the length-to-radius ratio is 50. The structured tree does retain detailed characteristics of wave propagation, including a phase lag between flow and pressure. Steele [147] and Cousins [42] have each expanded Olufsen's original structured tree to include tiered values based on terminal radius size for the length-to-radius ratio, blood viscosity, and branching parameters. Cousins [42] also used structured tree impedance to determine WK parameters in elastic vessels. However, Du et al. [47] note that there is currently a lack of validation studies for

the structured tree model.

### 4.3.2 Outflow boundary conditions

As previously discussed, the three-element WK model (shown in Figure 4.6) is the most popular terminal boundary condition due to each element corresponding to a physiological significance:  $R_1$  as the characteristic impedance,  $R_2$  as the total peripheral resistance, and  $C$  as the arterial compliance. The characteristic impedance and total arterial resistance are in the same units so oftentimes, the characteristic impedance is incorrectly referred to as a proximal vascular resistance. Although the units remain unchanged, the physical significance changes. The characteristic impedance is the resistance of a vascular bed to pulsatile flow in the absence of pulse wave reflections and is influenced by the dimensions and wall properties of large, proximal arteries. The vascular resistance is related to the number and size of small, peripheral vessels further down the network (and represented by the distal resistor in the WK model.) Based on the structure of the three-element WK model and its analogous counterpart in electrical circuits, we can derive the differential equation corresponding to the model.

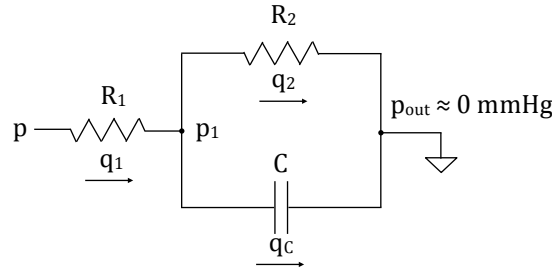


**Figure 4.6** Diagram depicting the three-element WK model. The model consists of a proximal resistor (or characteristic impedance)  $R_1$ , arterial compliance  $C$ , and a distal resistor (or total peripheral resistance)  $R_2$ .  $p$  and  $q$  are the pulsatile pressure and flow, respectively, at the end root of each terminal vessel. We note that the system is grounded to a point at which the pressure is approximately 0 mmHg. This accounts for all downstream resistance from the narrowing vasculature.

Pressure, flow, and resistance are related via (2.1.1). Through (2.1.1), Kirchhoff's current

law, and some basic knowledge of circuits, we obtain the following relations:

$$q_1 = q_2 + q_C$$

$$q_C = C \frac{dp_1}{dt}$$

$$p = q_1 R_1 + p_1$$

$$p_1 = q_2 R_2.$$

From this, we derive the equation for the three-element diagram demonstrated in Figure 4.6.

$$\begin{aligned} q_1 &= \frac{p_1}{R_2} + C \frac{dp_1}{dt} \\ &= \frac{p - R_1 q_1}{R_2} + C \left( \frac{dp}{dt} - R_1 \frac{dq_1}{dt} \right) \\ &= \frac{p}{R_2} - \frac{R_1}{R_2} q_1 + C \frac{dp}{dt} - R_1 C \frac{dq_1}{dt}. \end{aligned}$$

Upon rearranging the terms and allowing  $q_1 = q$  for simplicity, we obtain the commonly found equation for the three-element WK model:

$$\frac{dp}{dt} = R_1 \frac{dq}{dt} - \frac{p}{R_2 C} + \frac{R_1 + R_2}{R_2} \frac{q}{C}. \quad (4.3.2)$$

Many approaches have been put forward to estimate the parameter values in the three-element WK model. Because of their physiological significance, these approaches have all stemmed from measurements in data. Most commonly [3, 5, 6, 75, 103, 143], the total network resistance ( $R_T = R_1 + R_2$ ) is calculated as

$$R_T = \frac{\bar{p} - p_{\text{tissue}}}{\bar{q}} \quad (4.3.3)$$

where  $\bar{p}$  and  $\bar{q}$  are the mean pressure and flow, respectively, and  $p_{\text{tissue}}$  is often taken to be 0 mmHg. This leads to the question of determining  $R_1$  and  $R_2$  given  $R_T$ . Raines et al. [128] have cited the works of McDonald and Attinger [99] who estimated the ratio  $R_1/R_T$  as 0.2.



This estimation was based on studying arterial pulse wave propagation in canines and has been arbitrarily used in previous studies [16, 128, 149]. Reymond et al. [132] have stated that  $R_1/R_T$  ranged from 0.05 to 0.40 based on minimizing wave reflections. Du et al. [47], Xiao et al. [182], and Ismail et al. [75] have approximated

$$R_1 = \frac{\rho c_d}{A_d}$$

where  $c_d$  and  $A_d$  are the wave speed and cross-sectional area of the vessel at diastolic pressure. However, all of these studies with the exception of [132] were based on elastic wall models. Since the WK model accounts for energy dissipation in large vessels as well as small vessels, these approximations are not valid for viscoelastic wall models which provide higher levels of energy dissipation upstream.

As a point of departure from these approaches, we estimate  $R_1/R_T$  as a function of viscoelasticity, branching parameters, vessel stiffness, and terminal radius (see Chapter 7).

Estimation of the arterial compliance has proven to be much more difficult. Several methods have been put forward ranging from a simple time constant calculation to integral estimation. The most prevalent of the suggested methods relies heavily upon an exponential shaped diastolic pressure decay with

$$p - p_{out} = (p_0 - p_{out})e^{-t/\tau}$$

where  $\tau = R_T C_T$  is the time constant associated with the exponential decay and  $p_0$  is a reference pressure. This can often be distorted by wave reflections that can greatly affect the time constant and, furthermore, the estimated arterial compliance. This method was introduced by Alastruey et al. [6] in which  $R_T C_T$  is assumed to be a time constant of approximately 1.34 seconds, calculated based on the exponential decay that is present in the diastolic pressure curve. Although this method is known for its simplicity, the time constant associated with different vessels varies throughout a network, as discussed by Xiao et al. [182] who found the time constant  $\tau$  to be closer to 1.79 seconds. Thus, using the same time constant through a network proves inaccurate. Molino et al. [104] also used the time constant method to find the arterial compliance and verified their results by performing a linear regression on the logarithmic pressure values which resulted in a line with slope  $-1/\tau$ .

Xiao et al. [182] and Ismail et al. [75] also discussed another approach to calculate  $C_T$

based on Ohm's Law which approximates  $C_T = \frac{dV}{dp}$  as

$$C_T = \frac{q_{max} - q_{min}}{p_s - p_d} \Delta t$$

where  $V$  is the vessel fluid volume,  $q_{max}$  and  $q_{min}$  are the maximum and minimum flows at the inlet,  $p_s$  and  $p_d$  are the systolic and diastolic pressures, and  $\Delta t$  is the time difference between maximum and minimum flow values.

Shim et al. [143] introduced yet another method to calculate total arterial compliance. This method has been named the “integral method” because compliance is calculated using numerical integration of the WK model (equation 4.3.2) in the time domain. Compliance is calculated by the following equation during the earliest phase of ejection, taking into account both the root pressure and flow signals:

$$C_T = \frac{\int_{t_1}^{t_2} p_{avg}(t) dt - (R_1 + R_2) \int_{t_1}^{t_2} q_{avg}(t) dt}{R(p_{avg}(t_1) - p_{avg}(t_2)) - R_1 R_2 (q_{avg}(t_1) - q_{avg}(t_2))}. \quad (4.3.4)$$

### 4.3.3 Inflow boundary conditions

There are two natural choices for inlet boundary conditions to the network, a prescribed pressure or a prescribed flow waveform. Pressure as an input is deemed a logical choice given the availability of pressure recordings in the ascending aorta in this study. However, Anliker et al. [9] discussed the disadvantage of using pressure due to the inability to predict realistically observed flow profiles. Oftentimes, using pressure as an input produces “positive and negative flow velocities at the root of the aorta during the latter two-thirds of the cardiac cycle when the aortic valve is normally closed.” This has mainly been attributed to lack of precision of physiological pressure measurements. Small changes in pressure contribute to drastic changes in flow, thus necessitating a higher degree of accuracy for the pressure data.

A flow profile prescribed at the network inlet is an equally natural choice from a physiological standpoint. The flow profile determines cardiac output and pulse rate, both of which are important parameters. Our particular data, as discussed in Section 3.2, does not provide flow measurements so we developed a flow profile based on pressure-area measurements. Our initial estimation for a flow profile is discussed in [16], but collaborative work is ongoing for determining flow waveforms from an inverse problem perspective [12].

#### 4.3.4 Junctions conditions

In addition to prescribing an inlet to the network and outflow conditions at terminal branches, each vessel in the middle of the geometry requires an inflow boundary condition as well as an outflow condition. These are provided by assuming conservation of flow and continuity of pressure, i.e.

$$q_p(L_p, t) = \sum_{i=1}^n q_{d_i}(0_{d_i}, t) \quad \text{and} \quad p_p(L_p, t) = p_{d_i}(0_{d_i}, t)$$

where the subscript  $p$  denotes the parent vessel of length  $L_p$  and subscript  $d_i$  denotes the  $i$ th of  $n$  daughter vessels with  $i = 1, 2, \dots, n$ . It should be noted that for most physiological geometries,  $n = 2$ . Alternatively, Bernoulli's equation can be used to prescribe pressure at junctions.

*Minor losses*, or the small amounts of energy loss associated with curvature or junctions, were incorporated by Olufsen et al. [112] as well as others [147]. However, because these losses do not play a significant role in flow distribution of healthy or hypertensive networks, their affects will be neglected. For further information on minor losses in a 1-D model, the reader is referred to [112] and [147].

---

## Chapter 5

---

### Wave Intensity Analysis

The shape and magnitude of the blood pressure pulse waveform is an important indicator for assessing cardiovascular diseases such as hypertension [125]. Wave reflections, originating from junctions and other discontinuities in arterial networks, significantly contribute to the shape and magnitude of the observed pressure waveform. Analyzing these waveforms provides further insight into the underlying mechanisms by which the pressure pulse is shaped under normal and abnormal conditions. This can reveal crucial information about the functioning of the circulatory system or different disease states associated with hypertension.

Wave that propagate from the heart toward the periphery are termed *forward* waves while those originating in the blood vessels traveling towards to heart are called *backward* waves. One technique used to decompose a waveform into forward and backward waves in the time domain given the pulse wave velocity (PWV) is wave intensity analysis (WIA). WIA quantifies and identifies the types and directions of local arterial waves as forward or backward compressing or decompressing waves [119]. This method is based on the method of characteristics solution to the 1-D equations for blood flow (4.1.21).

With pressure and velocity time series from a single location, the corresponding wave intensity profile can be produced. Several studies have analyzed the wave intensity profiles from systemic arteries [76, 77, 79, 109, 154] under healthy and diseased states. However, these studies used *in vivo* pressure and velocity data which is measured invasively and difficult to accurately obtain. Other studies have applied WIA to numerically generated

waveforms from computational models [2, 4, 7] which we intend to do here.

## 5.1 Calculating WIA

The pressure and velocity waveforms are discretized into infinitesimal wave elements in  $(x, t)$  space,  $dp$  and  $du$ , respectively. Note that we solve the governing equations (4.1.21) for volumetric flow, pressure, and area and can calculate velocity  $u$  as  $u(x, t) = q(x, t)/A(x, t)$ . Waveforms are classified as compression waves if  $dp > 0$  corresponding to an increase in pressure whereas  $dp < 0$  refers to a decompression wave or a decrease in pressure. Similarly,  $du > 0$  shows an accelerating wave and  $du < 0$  shows a decelerating wave. The net wave intensity  $dI$  for a given location is defined as the product of infinitesimal wave elements, i.e.

$$dI = dp \, du, \quad (5.1.1)$$

defined in units of  $\text{Wm}^{-2}$ . The wave intensity dictates whether a wave is predominantly forward ( $dI > 0$ ) or backward propagating ( $dI < 0$ ). A summary of wave types and directions is shown in Table 5.1.

**Table 5.1** WIA table showing type and direction of dominating waveforms. Corresponding discretized WIA terminology is given in parenthesis.

$dp \, (\delta p_i)$	wavefront	$du \, (\delta u_i)$	wave type	$dI \, (W_i^I)$	wave type
$> 0$	compression	$> 0$	accelerating	$> 0$	forward compression
$< 0$	decompression	$< 0$	decelerating	$> 0$	forward decompression
$> 0$	compression	$< 0$	decelerating	$> 0$	backward compression
$< 0$	decompression	$> 0$	accelerating	$> 0$	backward decompression

From computational models where the waveforms are discretized into  $N$  points over a cardiac cycle of length  $T$  seconds, these infinitesimal wave elements are described as the change in pressure or velocity over a sufficiently small sampling time  $\delta t = T/N$  [120]. Simply replacing the infinitesimal wave elements with differences makes the magnitude of the wave intensity depend upon the time discretization. This is avoided by using a time-

normalized definition [130], i.e.

$$W_i^I = \frac{\delta p_i}{\delta t} \frac{\delta u_i}{\delta t}, \quad (5.1.2)$$

where  $i \in [0, N]$  and  $W_i^I$  is in units of  $\text{Wm}^{-2}\text{s}^{-2}$ . The wave intensity in (5.1.2) does not hold the analogy with physical intensity but still retains its ability to identify the direction of local waves. In this case,  $W_i^I$  only identifies the net effect of the forward and backward waves. The contributions from forward and backward waves are determined by decomposing  $W_i^I$  into forward and backward components which requires the knowledge of the local PWV.

The solution of (4.1.21) by the method of characteristics leads to the decomposition of waveforms into their forward and backward running components, i.e.

$$\delta p_i^\pm = \frac{1}{2} (\delta p_i \pm \rho c(p_i) \delta u_i) \quad \text{and} \quad \delta u_i^\pm = \frac{1}{2} \left( \delta u_i \pm \frac{\delta p_i}{\rho c(p_i)} \right). \quad (5.1.3)$$

More details on deriving these components can be found in [125]. The ‘+’ and ‘−’ signs denote the properties associated with the forward and backward waves, respectively, while the computed PWV  $c$  is approximated as

$$c(p) = \sqrt{\frac{A}{\rho} \frac{\partial p}{\partial A}}. \quad (5.1.4)$$

Thus, a forward pressure wave is a compression wave if  $\delta p_i^+ > 0$  and a decompression wave if  $\delta p_i^+ < 0$ . Similarly, the backward pressure wave is a compression wave if  $\delta p_i^- > 0$  or decompression if  $\delta p_i^- < 0$ . From (5.1.3) the pressure and velocity waveforms can be separated into its forward (+) and backward (−) components via

$$p_\pm(t) = p_0 + \int_{t-T}^T dp_\pm \quad \text{and} \quad u_\pm(t) = u_0 + \int_{t-T}^T du_\pm \quad (5.1.5)$$

where  $p_0$  and  $u_0$  are the pressure and velocity at the end of diastole, respectively.

---

## Chapter 6

---

# Numerical Methods

In Section 4.1.2 we saw that the fluid dynamics equations used to govern blood flow in large arteries are quasilinear and hyperbolic in nature. These equations do not have an analytical solution and thus an algorithm must be used to find an approximate solution. There are several numerical methods that can be implemented, ranging from a first-order finite difference scheme to the finite element method to a spectral scheme. Our simulations are based on the discontinuous Galerkin method in time, a specific formulation of the finite element method where the basis function and weight functions are chosen to be the same.

### 6.1 Literature review

There are many approaches for the numerical solution of the 1-D fluid dynamics model (see Table 6.1). Some [9, 138, 144, 149, 151] have used the method of characteristics to study wave propagation in the arteries while others [51, 111, 128, 132, 134, 137] have used implicit finite difference methods. Although finite difference methods (FDM) are known for their simplicity in implementation, finite element methods are better equipped to handle complicated geometries on a grander scale. Because we are considering a 1-D model, the geometry is easily discretized in either numerical scheme and thus either method would serve well. However, with regards to boundary conditions, FEM is more flexible in dealing

with complicated boundary conditions and thus it has become the most common method for solving blood flow equations.

As such, many [5, 25, 51, 54, 97, 106, 141, 142, 148, 172, 174, 182] have opted to use FEM to solve the equations governing 1-D blood flow. Most [97, 106, 141, 148, 172, 174] of these studies have been based on ideas developed by Christie et al. [39] who first introduced the discontinuous Galerkin (DG) scheme as it relates to fluid dynamics (Lasaint and Raviart [89] had previously introduced it in the context of neutron transport) and Hughes et al. [33, 69, 71, 72] who developed many methods to ensure the stabilization of solutions to problems such as this. Others [5, 25, 54, 142, 182] implement a DG scheme with a spectral/*hp* spatial discretization that involves the solution of Riemann problems at the interfaces within each artery, at each boundary, and at the junctions. These numerical methods generally use a second-order Adams-Bashford scheme for the time-integration.

Boileau et al. [30] compares the results from six numerical schemes commonly used for 1-D blood flow modeling: discontinuous Galerkin, locally conservative Galerkin, Galerkin least-squares finite element method, finite volume method, finite difference MacCormack method, and a simplified trapezium method. Their study concludes that when modeling 1-D blood flow dynamics, all numerical methods aforementioned show good agreement in their abilities to capture the main features of pressure, flow, and area waveforms in large arteries.

**Table 6.1** Summary of numerical methods implemented by references to solve 1-D fluid models. MoC: method of characteristics, FDM: finite difference method, FEM: finite element method, DG: discontinuous Galerkin.

MoC	FDM	FEM	FEM-DG	spectral/ <i>hp</i>	reference
x	x	x x	x	x	[9], [138], [144], [149], [151], [1], [30] [51] [111], [128], [132], [134], [137], [30] [5], [25], [51], [54], [142], [182], [30] [16], [97], [106], [141], [148], [172], [174], [30] [5], [25], [54], [142], [182]



## 6.2 Finite element method

The finite element method (FEM) is a popular technique used to compute accurate solutions to partial differential equations (PDEs). Many mathematical models in the physical and interdisciplinary sciences are formulated with PDEs, thus making the finite element method an essential mathematical technique.

In short, the FEM reduces a boundary value problem for a linear PDE to a system of linear equations written in differential matrix-vector form as  $\mathbf{KU} = \mathbf{F}$  that must be solved [58]. The differential matrix-vector form is also known as the *strong form* of the PDE and this will be derived for the problem at hand in Section 6.3. There are many different algorithms that can be used to solve  $\mathbf{KU} = \mathbf{F}$ , but in solving these equations, we make approximations and thus we end up deriving and solving what is known as the *weak form* (Section 6.4) to a specified degree of accuracy. The weak form solves an integrable function rather than solving the differential equation given by the strong form.

We have inherited a stabilized space-time FEM based on the discontinuous Galerkin method in time that was developed in previous works by Wan et al. [172], Steele [147, 148] and Vignon-Clementel [165]. Further details on this method can be found in [72, 172]. The spatial discretization uses continuous linear polynomials whereas the temporal discretization is defined by piecewise constant functions. The temporal discretization scheme may also be referred to as a backward Euler scheme but this particular solver has been historically referred to as a discontinuous Galerkin method.

Before defining the matrix-vector equation, the domain of each problem (in our case, each vessel), is divided into *finite elements*, in the following denoted as *elements*, defined by a finite number of *nodes*. These elements and nodes define the *mesh* along which the solution is approximated. As the number of nodes increases, the approximated solution becomes more accurate but at the price of increasing computational time. The vessels will be divided into  $e$  elements each, and because we are using a 1-D model in the axial direction, each element is associated with two nodes, denoting the beginning and the end. Element lengths are determined by the length of a given vessel divided by the number of specified elements,  $e$ . This produces an equally spaced mesh for each individual vessel in consideration but the element sizes vary between vessels of different lengths.

### 6.3 Strong form

In contrast to many previous studies, this formulation uses pressure  $p$  and flow  $q$  to determine area  $A$  through a constitutive equation given by the specified wall model. We first derive the strong form of our system of equations. It should be noted that solving these equations exactly is impossible and as such, we approximately solve the weak form (found in the next section) which provides an accurate estimation to the solution of this problem.

First note that the derivative of area with respect to  $x$  can be expanded as

$$\frac{\partial A}{\partial x} = \frac{\partial A}{\partial p} \frac{\partial p}{\partial x} + \frac{\partial A}{\partial x}.$$

Other wall model derivatives can be found in Appendix B. We can then rewrite our system of equations (4.1.21) in quasi-linear matrix form:

$$\mathbf{E} \frac{\partial \mathbf{U}}{\partial t} + \mathbf{B} \frac{\partial \mathbf{U}}{\partial x} = \mathbf{G} \quad (6.3.1)$$

where

$$\mathbf{U} = \begin{bmatrix} U_1 \\ U_2 \end{bmatrix} = \begin{bmatrix} p \\ q \end{bmatrix}, \quad (6.3.2)$$

$$\mathbf{E} = \begin{bmatrix} \frac{\partial A}{\partial p} & 0 \\ 0 & 1 \end{bmatrix}, \quad \mathbf{B} = \begin{bmatrix} 0 & 1 \\ \frac{A}{\rho} - \frac{\gamma+2}{\gamma+1} \left( \frac{q}{A} \right)^2 \frac{\partial A}{\partial p} & \frac{2q}{A} \left( \frac{\gamma+2}{\gamma+1} \right) \end{bmatrix}, \text{ and} \quad (6.3.3)$$

$$\mathbf{G} = \begin{bmatrix} 0 \\ -2(\gamma+2)\pi v \frac{q}{A} + \frac{\gamma+2}{\gamma+1} \left( \frac{q}{A} \right)^2 \frac{\partial A}{\partial x} \end{bmatrix}.$$

### 6.4 Weak form and FEM discretization

Following the case for solving general PDEs, the weak formulation is as follows (summarized from [147, 165]): Let  $\mathbf{W} = [W_1, W_2]^T$  be our test function where  $W_1, W_2 \in \mathcal{C}_0^\infty$ . Thus

$W_1(0) = W_1(L) = W_2(0) = W_2(L) = 0$ . We wish to find  $\mathbf{U}$  such that  $\forall \mathbf{W}^\top$  as defined above,

$$\int_0^L \int_0^T \left( \mathbf{W}^\top \mathbf{E} \frac{\partial \mathbf{U}}{\partial t} + \mathbf{W}^\top \mathbf{B} \frac{\partial \mathbf{U}}{\partial x} - \mathbf{W}^\top \mathbf{G} \right) dt dx = 0.$$

Using integration by parts, this can be rewritten as

$$\begin{aligned} \int_0^L \int_0^T \left( -\frac{\partial \mathbf{W}^\top \mathbf{E}}{\partial t} \mathbf{U} + \mathbf{W}^\top \mathbf{B} \frac{\partial \mathbf{U}}{\partial x} - \mathbf{W}^\top \mathbf{G} \right) dt dx \\ + \int_0^L \left( \mathbf{W}^\top(x, T) \mathbf{E}(x, T) \mathbf{U}(x, T) - \mathbf{W}^\top(x, 0) \mathbf{E}(x, 0) \mathbf{U}(x, 0) \right) dx = 0. \end{aligned}$$

Approximating  $\mathbf{U}$  and  $\mathbf{W}$  by piecewise constants in time and after discretizing in time ( $t_n \leq t \leq t_{n+1}$ ),

$$\begin{aligned} \int_0^L \int_{t_n}^{t_{n+1}} \left( -\frac{\partial \mathbf{W}^\top \mathbf{E}}{\partial t} \mathbf{U} + \mathbf{W}^\top \mathbf{B} \frac{\partial \mathbf{U}}{\partial x} - \mathbf{W}^\top \mathbf{G} \right) dt dx \\ + \int_0^L \left( \mathbf{W}^\top(x, t_{n+1}) \mathbf{E}(x, t_{n+1}) \mathbf{U}(x, t_{n+1}) - \mathbf{W}^\top(x, t_n) \mathbf{E}(x, t_n) \mathbf{U}(x, t_n) \right) dx = 0. \end{aligned}$$

By using a piecewise constant approximation in time for  $\mathbf{W}^\top$ , this can be further simplified to

$$\Delta t_n \int_0^L \left( \mathbf{W}^\top \mathbf{B} \frac{\partial \mathbf{U}^{n+1}}{\partial x} - \mathbf{W}^\top \mathbf{G} \right) dx + \int_0^L \mathbf{W}^\top (\mathbf{E}^{n+1} \mathbf{U}^{n+1} - \mathbf{E}^n \mathbf{U}^n) dx$$

Here, the superscripts  $n$  and  $n+1$  correspond to the solution at times  $t_n$  and  $t_{n+1}$ , respectively, with  $\Delta t_n = t_{n+1} - t_n$  being the time step. To facilitate convergence, we will augment these equations with a stabilization term.

Let  $\mathbf{C}$  be a matrix such that  $\mathbf{C} = \mathbf{C}(\mathbf{U})$  where  $\mathbf{C}\mathbf{U} = \mathbf{G}$  with  $\mathbf{U}$  and  $\mathbf{G}$  as previously defined in (6.3.2) and (6.3.3). Thus, we want to find  $\mathbf{C}$  such that

$$\mathbf{C} \begin{bmatrix} p \\ q \end{bmatrix} = \begin{bmatrix} 0 \\ -2(\gamma+2)\pi v \frac{q}{A} + \frac{\gamma+2}{\gamma+1} \left( \frac{q}{A} \right)^2 \frac{\partial A}{\partial x} \end{bmatrix}$$

where  $p = U_1$  and  $q = U_2$ . Writing  $\mathbf{C}$  as a function of  $\mathbf{U}$ , we find

$$\mathbf{C}(\mathbf{U}) = \begin{bmatrix} 0 & 0 \\ 0 & -2(\gamma+2)\pi v \frac{1}{A} + \left(\frac{\gamma+2}{\gamma+1}\right) \frac{q}{A^2} \frac{\partial A}{\partial x} \end{bmatrix}.$$

Given this definition of  $\mathbf{C}(\mathbf{U})$ , we define a matrix differential operator by

$$\mathcal{L}(\mathbf{U}) = \mathbf{E}(\mathbf{U}) \frac{\partial}{\partial t} + \mathbf{B}(\mathbf{U}) \frac{\partial}{\partial x} - \mathbf{C}(\mathbf{U}).$$

In the case of a piecewise constant in time and a piecewise linear approximation in space,  $\mathcal{L}(\mathbf{U})\mathbf{U}$  can be written as

$$\begin{aligned} \mathcal{L}(\mathbf{U})\mathbf{U} &= \mathbf{B}(\mathbf{U}) \frac{\partial \mathbf{U}}{\partial x} - \mathbf{C}(\mathbf{U})\mathbf{U} \\ &= \mathbf{B}(\mathbf{U}) \frac{\partial \mathbf{U}}{\partial x} - \mathbf{G}(\mathbf{U}). \end{aligned}$$

Applying the matrix differential operator to our test function vector,

$$\mathcal{L}(\mathbf{U})^T \mathbf{W} = \mathbf{B}(\mathbf{U})^T \frac{\partial \mathbf{W}}{\partial x} - \mathbf{C}(\mathbf{U})^T \mathbf{W}.$$

The domain is then discretized into elements  $\Omega_i$  where  $1 < i < J$ , and  $J$  is the total number of elements. A stabilization term is added to provide least-squares control of the residual [73] in the form

$$\Delta t_n \sum_i \int_{\Omega_i} (\mathcal{L}(\mathbf{U})^T \mathbf{W})^T \tau (\mathcal{L}(\mathbf{U})\mathbf{U}) dx$$

where the summation ranges over the element interiors and  $\tau = \tau(\mathbf{U})$  is the stabilization matrix [147, 165, 172] defined by

$$\tau = \left[ \frac{2}{\Delta t_n} \mathbf{I} + \frac{2}{h} |\mathbf{B}| + |\mathbf{C}| \right]^{-1}.$$

The absolute value of a  $2 \times 2$  matrix  $\mathbf{Z}$  can be obtained from the Cayley-Hamilton theorem [147, 148, 165]:

$$|\mathbf{Z}| = \frac{\mathbf{Z}^2 + \sqrt{\det(\mathbf{Z}^2)} \mathbf{I}}{\sqrt{tr(\mathbf{Z}^2) + 2\sqrt{\det(\mathbf{Z}^2)}}}.$$

Thus, we ultimately want to find  $\mathbf{U}^{n+1}$  such that  $\forall \mathbf{W}$ ,

$$\begin{aligned} \Delta t_n \int_0^L \mathbf{W}^\top \mathbf{B} \frac{\partial \mathbf{U}^{n+1}}{\partial x} - \mathbf{W}^\top \mathbf{G} \, dx + \int_0^L \mathbf{W}^\top (\mathbf{U}^{n+1} - \mathbf{U}^n) \, dx \\ + \Delta t_n \sum_i \int_{\Omega_i} \left( \mathbf{B}^\top \frac{\partial \mathbf{W}}{\partial x} - \mathbf{C}^\top \mathbf{W} \right)^\top \tau \left( \mathbf{B} \frac{\partial \mathbf{U}^{n+1}}{\partial x} - \mathbf{G} \right) \, dx = 0, \end{aligned}$$

or

$$\begin{aligned} \Delta t_n \int_0^L \mathbf{W}^\top \mathbf{B} \frac{\partial \mathbf{U}^{n+1}}{\partial x} - \mathbf{W}^\top \mathbf{G} \, dx + \int_0^L \mathbf{W}^\top (\mathbf{U}^{n+1} - \mathbf{U}^n) \, dx \\ + \Delta t_n \sum_i \int_{\Omega_i} \left( \frac{\partial \mathbf{W}^\top}{\partial x} \mathbf{B} - \mathbf{W}^\top \mathbf{C} \right) \tau \left( \mathbf{B} \frac{\partial \mathbf{U}^{n+1}}{\partial x} - \mathbf{G} \right) \, dx = 0. \end{aligned}$$

For simplicity, the  $\mathbf{U}^{n+1}$  argument in  $\mathbf{B}$ ,  $\mathbf{C}$ , and  $\mathbf{G}$  is suppressed.

By assuming there are  $n$  nodal points in our spatial discretization, the vector fields  $\mathbf{W}$  and  $\mathbf{U}^{n+1}$  are written using the usual piecewise linear shape functions  $N_\alpha(x)$ :

$$\mathbf{W} = \sum_{\alpha=1}^n N_\alpha \mathbf{C}_\alpha \quad \text{and} \quad \mathbf{U}^{n+1} = \sum_{\beta=1}^n N_\beta \mathbf{U}_\beta^{n+1}.$$

A vector valued function can be written on each node  $\alpha = 1, 2, \dots, n$  defined by

$$\begin{aligned} \mathcal{R}_\alpha(\mathbf{U}^{n+1}) = \Delta t_n \int_0^L \left( N_\alpha \mathbf{C}_\alpha^\top \sum_\beta \frac{\partial N_\beta}{\partial x} \mathbf{B} \mathbf{U}_\beta^{n+1} - N_\alpha \mathbf{C}_\alpha^\top \mathbf{G} \right) \, dx \\ + \int_0^L \left( N_\alpha \mathbf{C}_\alpha^\top \sum_\beta N_\beta (\mathbf{U}_\beta^{n+1} - \mathbf{U}_\beta^n) \right) \, dx \\ + \Delta t_n \sum_i \int_{\Omega_i} \left( \frac{\partial N_\alpha}{\partial x} \mathbf{C}_\alpha^\top \mathbf{B} - N_\alpha \mathbf{C}_\alpha^\top \mathbf{C} \right) \tau \left( \mathbf{B} \sum_\beta \frac{\partial N_\beta}{\partial x} \mathbf{U}_\beta^{n+1} - \mathbf{G} \right) \, dx = 0 \end{aligned}$$

which can be further simplified to

$$\begin{aligned}
\mathcal{R}_\alpha(\mathbf{U}^{n+1}) &= \Delta t_n \int_0^L \left( N_\alpha \sum_\beta \frac{\partial N_\beta}{\partial x} \mathbf{B} \mathbf{U}_\beta^{n+1} - N_\alpha \mathbf{G} \right) dx \\
&+ \int_0^L \left( N_\alpha \sum_\beta N_\beta (\mathbf{U}_\beta^{n+1} - \mathbf{U}_\beta^n) \right) dx \\
&+ \Delta t_n \sum_i \int_{\Omega_i} \left( \frac{\partial N_\alpha}{\partial x} \mathbf{B} - N_\alpha \mathbf{C} \right) \tau \left( \mathbf{B} \sum_\beta \frac{\partial N_\beta}{\partial x} \mathbf{U}_\beta^{n+1} - \mathbf{G} \right) dx = 0.
\end{aligned}$$

A Newton-Raphson method is implemented to solve the nonlinear system. It is facilitated by using the following iterative scheme:

$$\begin{aligned}
\sum_\beta \tilde{\mathbf{K}}_{\alpha\beta}^{n+1,j} \partial \mathbf{U}_\beta^{n+1,j+1} &= -\mathcal{R}_\alpha^{n,j} \\
\mathbf{U}_\beta^{n+1,j+1} &= \mathbf{U}_\beta^{n+1,j} + \partial \mathbf{U}_\beta^{n+1,j+1}
\end{aligned}$$

where  $j$  represents the  $j^{th}$  iteration. In our Newton-Raphson method,  $\tilde{\mathbf{K}}_{\alpha\beta}$  is given by

$$\begin{aligned}
\tilde{\mathbf{K}}_{\alpha\beta} &= \frac{\partial \mathcal{R}_\alpha}{\partial \mathbf{U}_\beta^{n+1}} \\
&= \Delta t_n \int_0^L \left( N_\alpha \mathbf{B} \frac{\partial N_\beta}{\partial x} - N_\alpha \mathbf{C} N_\beta \right) dx \\
&+ \int_0^L N_\alpha \mathbf{I} N_\beta dx \\
&+ \Delta t_n \sum_i \int_{\Omega_i} \left( \frac{\partial N_\alpha}{\partial x} \mathbf{B} - N_\alpha \mathbf{C} \right) \tau \left( \mathbf{B} \frac{\partial N_\beta}{\partial x} - \mathbf{C} N_\beta \right) dx.
\end{aligned}$$

Upon convergence by the solver (to a chosen tolerance), the scheme is advanced in time to solve for each successive time step, which is initialized by the solution from the previous time step.

This numerical scheme has been utilized for multiple boundary conditions (pure resis-

tor, three-element WK) and previously verified by Vignon-Clementel [165] when solving for  $A$  and  $q$  then using  $A$  to obtain  $p$ . In doing so, she observed good numerical convergence and stability properties. Additionally, the relationships prescribed by the boundary conditions were numerically satisfied and results accounted for conservation of mass between the inlets and outlets. Steele et al. [148] validated this scheme in this formulation for a linear and nonlinear viscoelastic wall model.

## 6.5 Convergence of the solver

We consider pulsatile flow in a single straight and single tapered vessel with a prescribed inflow profile and a 3-element WK model at the outlet with constant parameter values. We increase the number of elements (spatial discretization) and number of time steps per period (temporal discretization) to study convergence of the solver for both tapered and non-tapered vessels.

### 6.5.1 Non-tapered vessel

The following simulations were performed on a straight (non-tapered) vessel that is 16 centimeters long with a proximal and distal radius of 0.905 centimeters. The geometry was chosen to mimic the proximal descending aorta. Results are shown in the middle of the vessel for pressure, area, and flow. First, we study convergence with the linear elastic wall model (4.2.5). By varying the number of elements while maintaining the number of time steps at 1200 time steps per period, our results have converged for all elements. Next, we investigate convergence in the temporal domain. By fixing the number of elements at 12 while changing the number of time steps, we note that our results do not begin to converge until 800 time steps per period. Thus, we must consider 800 or more time steps per period in order to achieve temporal convergence. This falls within the Courant-Friedrichs-Lewy (CFL) condition which must be satisfied to guarantee convergence for the FDM when solving hyperbolic PDEs. The CFL condition has the following form

$$c \frac{\Delta t}{\Delta x} \leq 1 \quad (6.5.1)$$

where  $c$  is the wave speed and  $\Delta t$  and  $\Delta x$  correspond to the time step and interval length in the solver, respectively. Our wave speed  $c$  is approximately 550 cm/s,  $\Delta t = 0.53$  s/800

(period length is 0.53 s), and  $\Delta x = 16 \text{ cm}/12$ . Equation (6.5.1) is evaluated as

$$550 \text{ cm/s} \frac{0.53 \text{ s}/800}{16 \text{ cm}/12} = 0.4858 \leq 1$$

and thus the CFL condition is also met.

The temporal residual errors were calculated as the maximum relative error (infinity norm) between the current time step and the finest time step, i.e.

$$e_{\xi_i} = \max \frac{\xi_i - \xi_{9600}}{\xi_{9600}} \quad (6.5.2)$$

where the number of time steps per period  $i = \{200, 400, 800, 1200, 2400, 4800\}$  and  $\xi = \{p, A\}$ . Spatial residual errors were calculated in a similar fashion:

$$E_{\xi_j} = \max \frac{\xi_j - \xi_{200}}{\xi_{200}} \quad (6.5.3)$$

where the number of elements  $j = \{6, 12, 24, 50, 100\}$  and  $\xi$  is as previously defined. Results for the spatial and temporal pressure and area error norms are shown in Figure 6.1.

Next, the Kelvin viscoelastic wall (shown in Table 4.3) is imposed on the straight vessel. The vessel has the same radius and length as in the previous case. To show convergence in space for the viscoelastic wall model, we use 1200 time steps per period while varying the number of elements. We show temporal convergence by maintaining 12 elements and varying the time steps per period, exactly as done in the previous elastic case. Again, we see that we have spatial convergence for any number of elements while we must use at least 800 time steps per period to achieve temporal convergence. Thus, for both elastic and viscoelastic wall models in a straight vessel, we find the same convergence criteria. Error norms were calculated by (6.5.2) and (6.5.3) and results are shown in Figure 6.2.

### 6.5.2 Tapered vessel

Because arteries naturally taper *in vivo*, we want to ensure that our numerical solutions also converge for tapered vessels. The vessel studied here is 16 centimeters long and tapers from a radius of 1.05 centimeters at the inlet to 0.805 centimeters at the outlet. The same inflow and outflow boundary conditions and parameters used in the straight vessel (Section 6.5.1) are prescribed in this case.



We study the convergence with an elastic wall model in the case of a tapering vessel. A similar procedure is followed as in Section 6.5.1; the number of elements varies while maintaining the number of time steps (800 per period). It is evident in Figure 6.3 that tapering plays a role in computational convergence. A minimum of 50 elements must be used before the solver shows convergence. This is significantly more than in the non-tapered elastic vessel case presented in Section 6.5.1. We investigate convergence in the temporal domain by maintaining the number of elements (12) while changing the number of time steps, we see that our results do not begin to converge until 800 time steps per period. Thus for 1200 or more time steps per period, we have shown convergence temporally (Figure 6.3). The temporal and spatial residual errors were calculated and results for the error norms are shown in Figure 6.3.

Our last convergence evaluation is for a tapered vessel with a viscoelastic wall given by the Kelvin model (Table 4.3). The vessel has the same radius and length as previously studied with the elastic model. The elastic case for the tapered vessel shows convergence after 1200 time steps per period. Thus, to show convergence in space, we use 1200 time steps per period while varying the number of elements. As shown in Figure 6.4, we see convergence at 100 elements. Thus, viscoelastic vessels require a finer spatial mesh to achieve convergence. Likewise, we maintain the number of elements while varying the time steps per period to show convergence in the temporal direction (Figure 6.4). We see the solver begins to converge for 800 time steps per period. Based on the temporal and spatial convergence criteria, we see that if we use 1200 time steps and 100 elements, our computations converge for any vessel geometry (nontapered or tapered) with any linear wall model (elastic or viscoelastic).

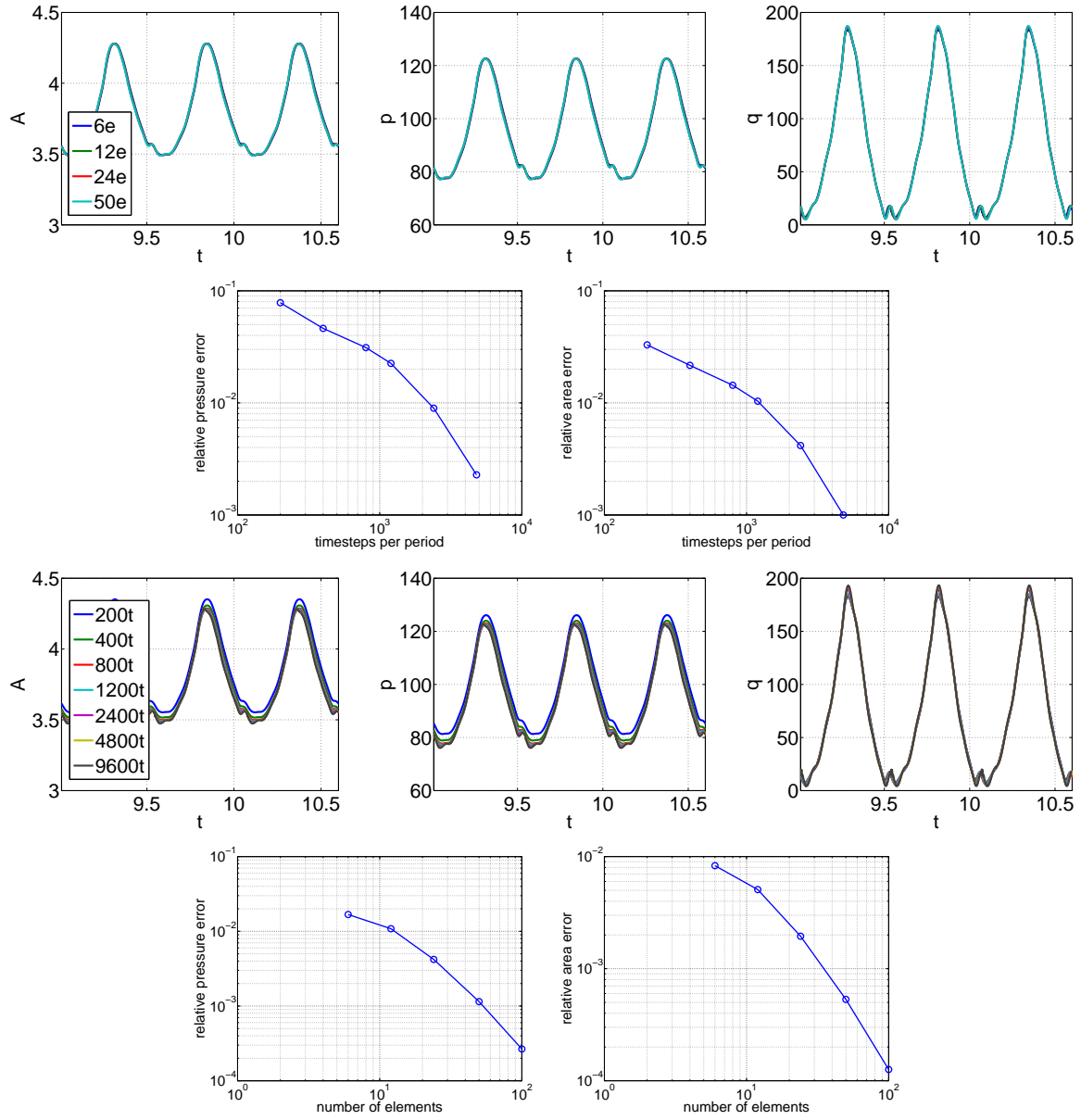


**Figure 6.1** (1st row) Maintaining the time steps per period (1200) converges for any number of elements. This shows spatial convergence for a straight elastic vessel. (2nd row) The temporal residual errors shown for pressure and area of an elastic non-tapered vessel on a log-log plot. (3rd row) The vessel is discretized spatially into 12 elements while increasing the time steps per period: 200, 400, 800, 1200, 2400, 4800, 9600. It is apparent that the solutions corresponding to 800, 1200, 2400, 4800, and 9600 time steps are the same, thus signifying temporal convergence of the solver. (4th row) The spatial residual errors shown for pressure and area of an elastic non-tapered vessel on a log-log plot.

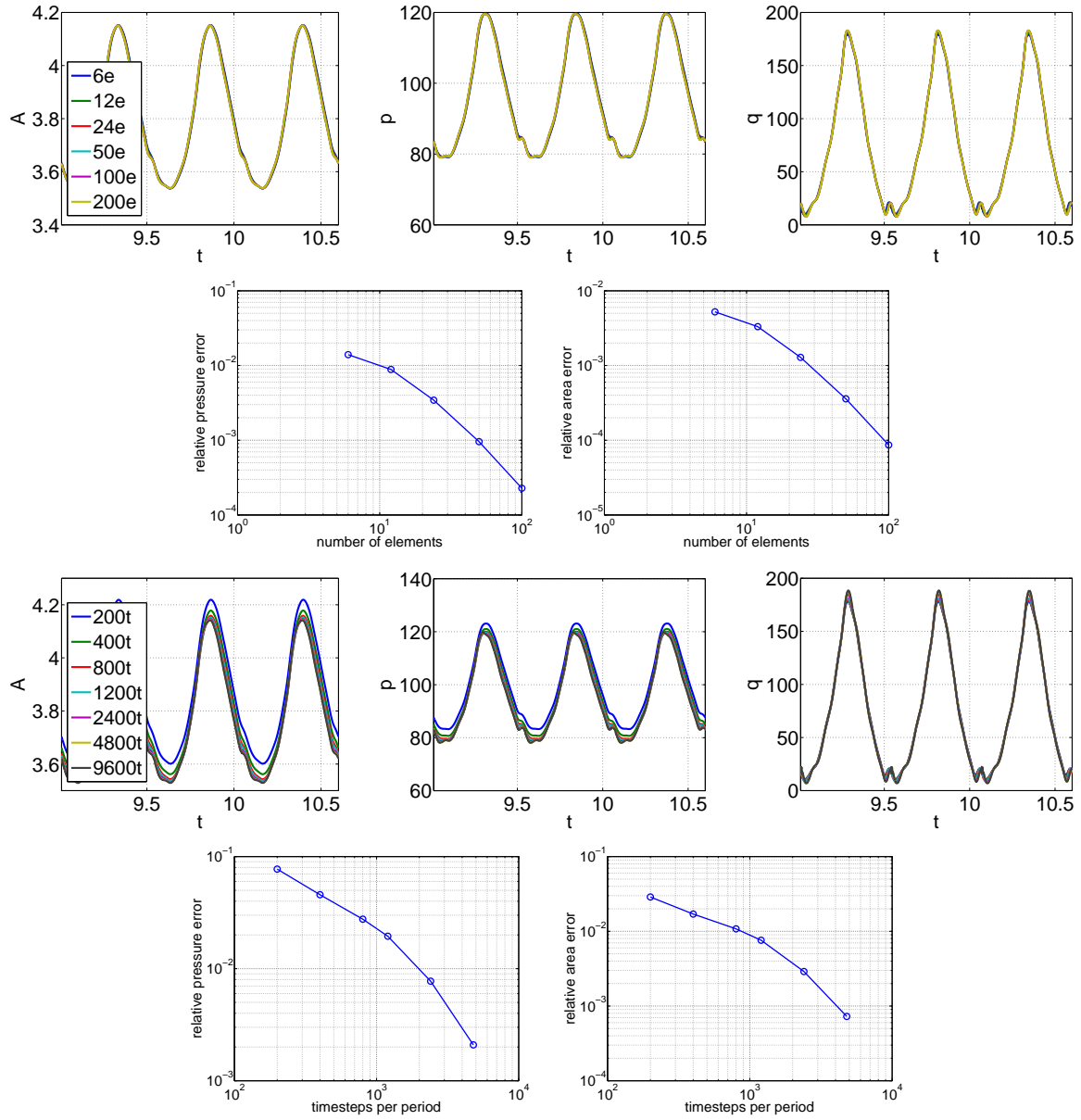


**Figure 6.2** (1st row) Convergence in space for the viscoelastic wall model for a non-tapered vessel with 1200 time steps per period. Although we change the number of elements (spatial mesh), we obtain the same results thus signifying convergence. (2nd row) The spatial residual errors shown for pressure and area of a viscoelastic non-tapered vessel on a log-log plot. (3rd row) Temporal convergence for the viscoelastic wall model with a non-tapered vessel discretized spatially into 12 elements. If each period is discretized into 800 or more time steps, we see convergence of the solver. (4th row) The temporal residual errors shown for pressure and area of a viscoelastic non-tapered vessel on a log-log plot.

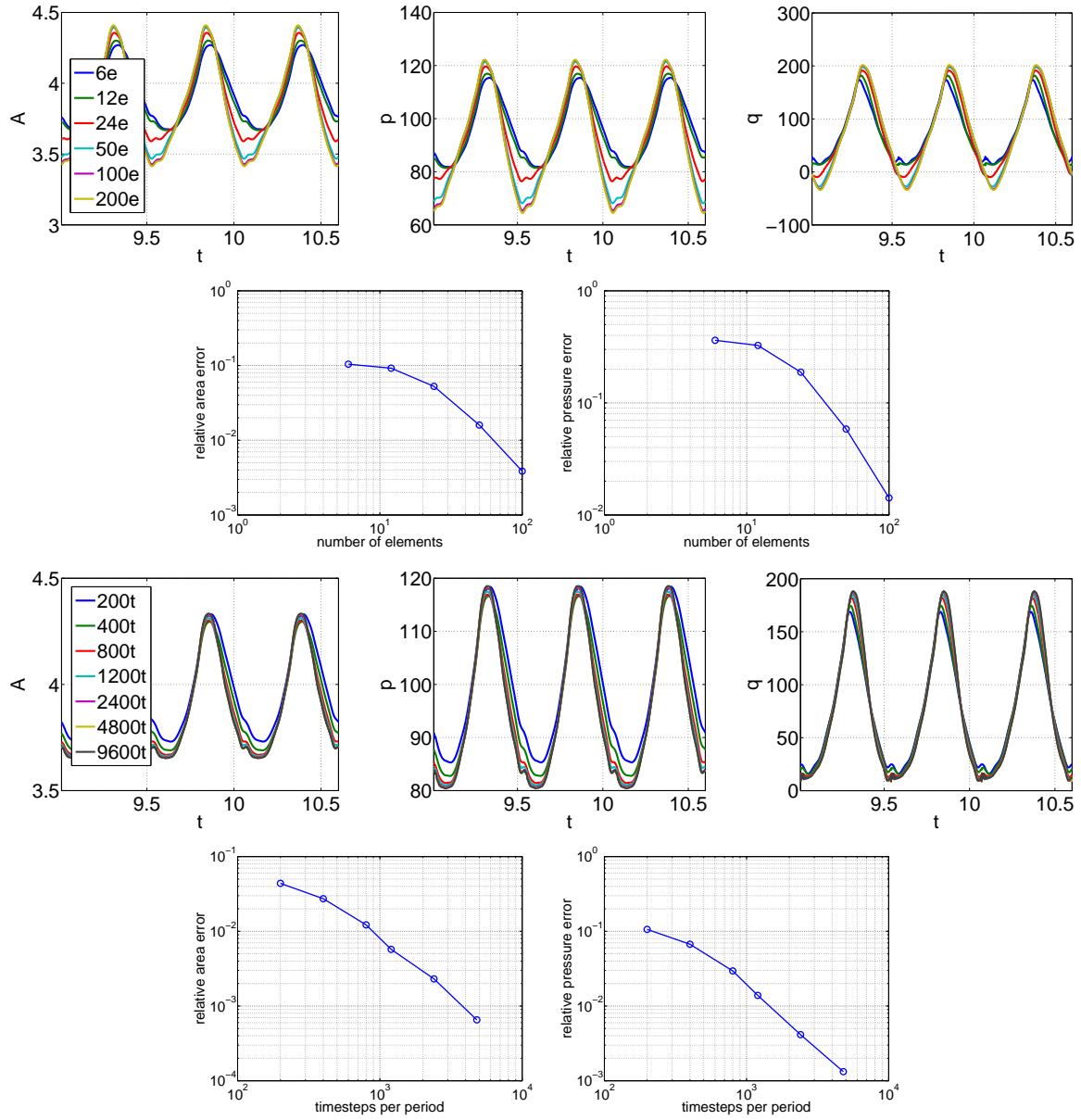


**Figure 6.3** (1st row) Maintaining the time step at 800 per period, we obtain approximately the same results for 50, 100, or 200 elements. Thus, signifying spatial convergence for 50 or more elements in an elastic tapering vessel. (2nd row) The spatial residual errors shown for pressure and area of an elastic tapered vessel on a log-log plot. (3rd row) The number of elements remains fixed at 12 per vessel while the time steps are 200, 400, 800, 1200, 2400, 4800, 9600 per period. It is apparent that the solutions corresponding to 1200, 2400, 4800, and 9600 time steps are the same, thus signifying temporal convergence of the solver. (4th row) The temporal residual errors shown for pressure and area of an elastic tapered vessel on a log-log plot.

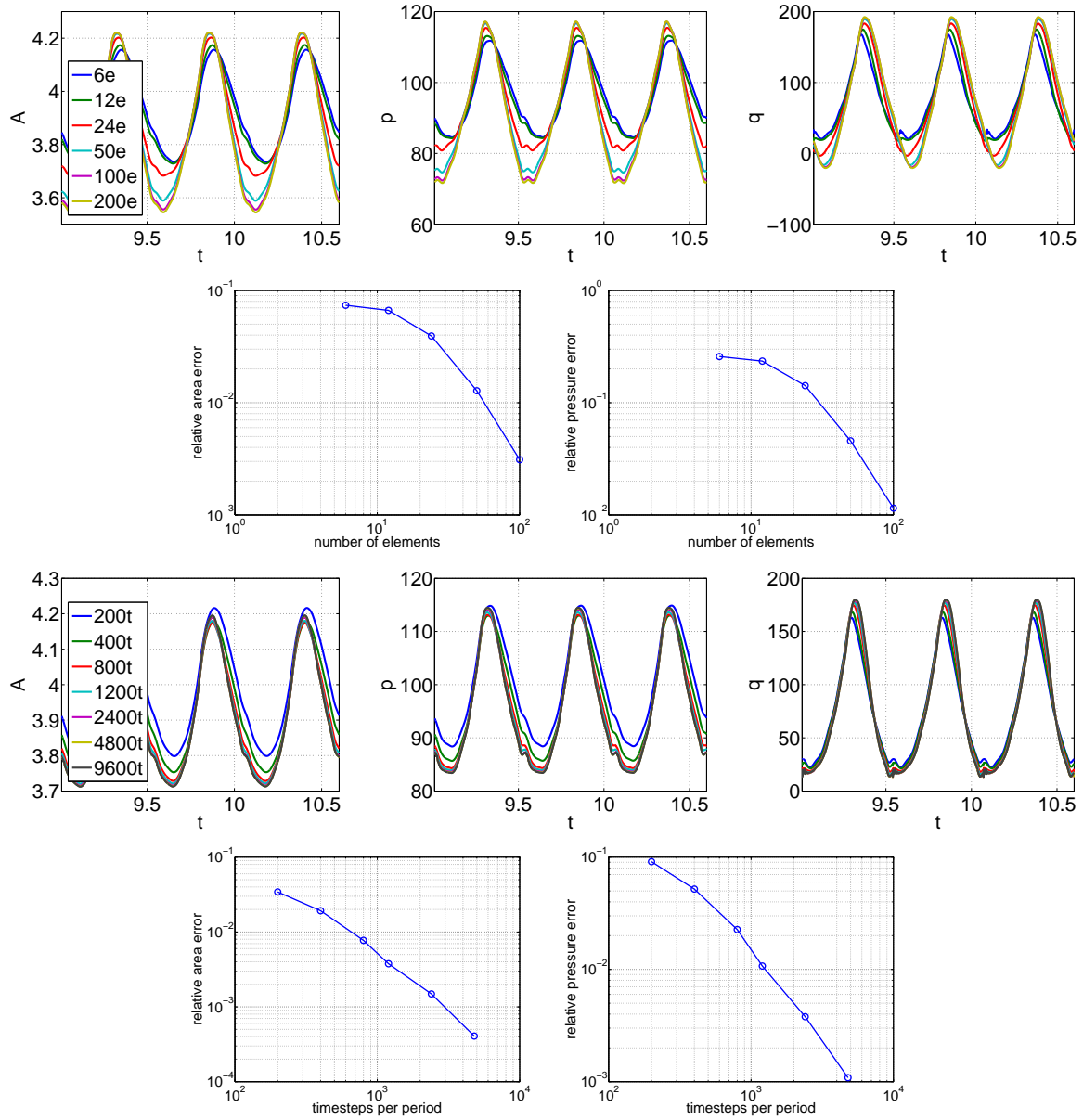


**Figure 6.4** (1st row) Convergence in space for the viscoelastic wall model in a tapered vessel. Although we change the number of elements (spatial mesh), we obtain the same results for 100+ elements, thus signifying convergence. (2nd row) The spatial residual errors shown for pressure and area of a viscoelastic tapered vessel on a log-log plot. (3rd row) Temporal convergence for the viscoelastic wall model with a tapered vessel discretized spatially into 12 elements. (4th row) The temporal residual errors shown for pressure and area of a viscoelastic tapered vessel on a log-log plot.

---

# Chapter 7

---

## Results

This chapter presents results related to parameter estimation within the 0-D wall models as well as results from 1-D elastic (Section 7.3) and viscoelastic (Section 7.4) network simulations. The WIA results corresponding to the results in Sections 7.3 and 7.4, are shown and discussed in Section 7.5.

### 7.1 Parameter estimation

As discussed in Section 4.2, the wall models describe vessel distention as a function of arterial blood pressure. This relation then characterizes the mechanical wall properties via a set of parameter values [159]. Using the data available, we determine the biomechanical properties through this pressure-area relation for each individual sheep.

Using measured blood pressure as an input for each vessel segment, parameters specifying wall properties were estimated by minimizing the least squares error  $J$  between measured  $a(t_j)$  and computed  $A(t_j; \lambda)$  values of the cross-sectional area, where  $\lambda$  is the parameter vector associated with each wall model (computed using (4.2.33)). The cost function  $J$  is given by

$$J(\lambda) = \frac{1}{n - n_p} \sum_{j=1}^n |A(t_j; \lambda) - a(t_j)|^2, \quad (7.1.1)$$

where  $J$  is scaled by the difference between the number of data points in the time series

and the number of parameters in the wall model  $n - n_p$  ( $n_p = 2$  for the elastic and  $n_p = 4$  for the viscoelastic model). Optimizations were performed using Matlab's Nelder Mead method, with a maximum of  $10^8$  function evaluations, a tolerance of  $10^{-9}$ , and a maximum of 10000 iterations on an iMac 2.8 GHz Intel Core i7. Appendix D contains more information on the Nelder Mead method. For the 0-D elastic model, optimization took approximately 1.65 seconds per data set, while for the 0-D Kelvin model optimization took approximately 133 seconds per data set. To ensure that estimated minimum values are within physiological range, initial parameter estimates were set based on literature values. Wall thickness  $h$  was determined by the calculated values as given in Table 7.1 while  $E$ ,  $r_0$ ,  $A_1$ , and  $b_1$  were optimized. Initial parameter values for  $E$  were obtained from Fung's estimates [55, 56],  $r_0$  was initialized using the measured diastolic radius for each vessel, and the viscoelastic parameters  $A_1^i = 0.05$  and  $b_1^i = 0.025$  were chosen based on our previous study [16, 160]. Optimizations were repeated twice for each dataset to ensure the parameter values were independent of the initial parameter vector. For the second optimization, initial parameter values were doubled relative to the original values to ensure that both optimizations gave the same estimated parameter values. Optimizations were first carried out for the elastic model and subsequently for the viscoelastic model. Estimated parameter values for Young's modulus  $E$ , the zero-strain radius  $r_0$ , and viscoelastic parameters  $A_1$  and  $b_1$  as well as measured values for  $h$  and  $r_0$  are given in Table 7.1. Note that parameter values vary between the elastic and viscoelastic wall. This is due to the deformation that the viscoelastic wall accounts for through  $A_1$  and  $b_1$  where the elastic wall is purely deformed based on  $Eh$  and  $r_0$ .

### 7.1.1 Vessel stiffness and unstressed vessel radii

To determine how vessel stiffness increases with vessel caliber, similar to [112, 114] we plotted optimized values  $Eh/r_0$  as a function of  $r_0$  for all vessels. This pressure-area fit was performed twice: once for the elastic network where we sought a relation for the stiffness of large arteries (vessels for which  $r_0 > 0.8$  cm) and once where we utilized all sheep data as well as data from Olufsen's dissertation. In both scenarios, following Olufsen [112, 114], we assumed that vessel stiffness tapered exponentially following

$$\frac{Eh}{r_0} = k_1 e^{k_2 r_0} + k_3. \quad (7.1.2)$$

**Table 7.1** Average geometric and mechanical optimized parameters for the elastic and viscoelastic wall models. Results are presented as mean  $\pm$  standard deviation. For all segments,  $n = 11$ ,  $h$  is the wall thickness,  $r_0$  is the zero-strain radius,  $E$  is the Young's modulus, and  $A_1$  and  $b_1$  are the viscoelastic relaxation parameters. Parameters noted n.d. are non dimensional.

Elastic Model	$h$ (cm) meas	$r_0$ (cm) meas	$r_0$ (cm)	$E$ (mmHg)
Ascending Aorta (AA)	$1.26 \pm 0.16$	$0.936 \pm 0.062$	$0.996 \pm 0.060$	$574 \pm 95$
Proximal Desc Aorta (PD)	$1.10 \pm 0.04$	$0.886 \pm 0.025$	$0.902 \pm 0.190$	$844 \pm 87$
Medial Desc Aorta (MD)	$1.06 \pm 0.04$	$0.856 \pm 0.037$	$0.876 \pm 0.021$	$918 \pm 126$
Distal Desc Aorta (DD)	$0.78 \pm 0.07$	$0.825 \pm 0.010$	$0.830 \pm 0.009$	$2282 \pm 264$
Femoral Artery (FA)	$0.31 \pm 0.02$	$0.281 \pm 0.018$	$0.281 \pm 0.013$	$2634 \pm 353$
Brachiocephalic Trunk (BT)	$0.91 \pm 0.04$	$0.890 \pm 0.094$	$0.897 \pm 0.039$	$943 \pm 112$
Carotid Artery (CA)	$0.38 \pm 0.01$	$0.406 \pm 0.021$	$0.406 \pm 0.001$	$10176 \pm 732$

Kelvin Viscoelastic Model	$r_0$ (cm)	$E$ (mmHg)	$A_1$ (n.d.)	$b_1$ (s <sup>-1</sup> )
Ascending Aorta (AA)	$0.973 \pm 0.058$	$480 \pm 68$	$0.555 \pm 0.134$	$0.0524 \pm 0.008$
Proximal Desc Aorta (PD)	$0.890 \pm 0.018$	$732 \pm 76$	$0.573 \pm 0.189$	$0.0439 \pm 0.008$
Medial Desc Aorta (MD)	$0.864 \pm 0.021$	$780 \pm 104$	$0.650 \pm 0.197$	$0.0442 \pm 0.010$
Distal Desc Aorta (DD)	$0.826 \pm 0.008$	$2044 \pm 167$	$0.746 \pm 0.238$	$0.0362 \pm 0.012$
Femoral Artery (FA)	$0.279 \pm 0.013$	$2355 \pm 388$	$0.750 \pm 0.209$	$0.0359 \pm 0.011$
Brachiocephalic Trunk (BT)	$0.878 \pm 0.040$	$765 \pm 92$	$0.606 \pm 0.054$	$0.0531 \pm 0.007$
Carotid Artery (CA)	$0.405 \pm 0.010$	$9080 \pm 898$	$0.543 \pm 0.093$	$0.0402 \pm 0.008$

Mean values were calculated over all datasets excluding outlying measurements (shown in Figure 7.5). The following measurements were determined to be outliers: BT (blue), AA (purple), DD (blue, cyan), CA (red, green, pink).

For the large sheep artery data (see Figure 7.1), the parameters were determined as  $k_1 = 4.5 \times 10^8$  mmHg,  $k_2 = -15.53\text{cm}^{-1}$ , and  $k_3 = 541$  mmHg by best fitting the single vessel values (Table 7.1). With these values, this relation exhibits a poor fit to stiffness values found in the CA and FA. Moreover, we were able to compare the estimated  $r_0$  values against those measured *ex vivo* and found that the two were indistinguishable.

We constructed a linear relation (shown in Figure 7.2) between the measured diastolic radius and the unstressed radius that holds for all arteries in this study. This relation was not used in this study but could be used in future studies to predict zero-strain radii since these are typically not measured experimentally. In fact,  $r_0$  could only be measured in this case because data were obtained *ex vivo*. Many network models are set up and compared with *in vivo* data where the zero-strain radii cannot be measured. For such studies, the relation found here could be used, assuming that the relation between zero-strain and diastolic radii are the same *ex vivo* and *in vivo*.



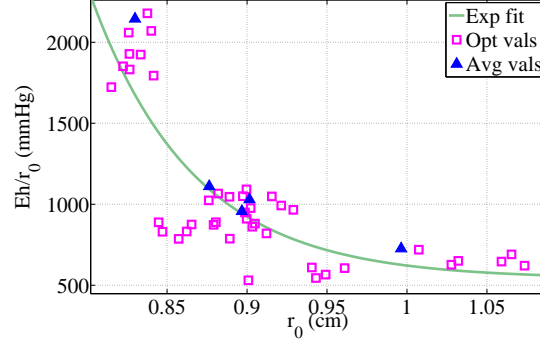


**Figure 7.1** Elastic modulus and zero-strain radius optimized values (pink squares) for larger arteries with radius  $> 0.8$  cm. An exponential decay function (green) given by (7.1.2) was fitted through these points. Average values of  $Eh/r_0$  for each vessel are marked with blue triangles. Values defining the exponential fit are  $k_1 = 4.5 \times 10^8$  mmHg,  $k_2 = -15.53$  cm $^{-1}$ , and  $k_3 = 541$  mmHg.

For viscoelastic networks (Section 7.4) where stiffness was allowed to vary as a function of radius, we appended our data set with the values found in Olufsen's dissertation [112]. Olufsen's data were digitized using Plot Digitizer, scaled to the appropriate units, and augmented with the sheep data for vessel stiffness and radius. A single exponential function that describes stiffness as a function of radius for arteries of any size is shown in Figure 7.3 where  $k_1 = 4.7 \times 10^8$  mmHg,  $k_2 = -25.23$  cm $^{-1}$ , and  $k_3 = 756$  mmHg.

## 7.2 Network geometry extracted from *ex vivo* experimental measurements

The network is composed of the fourteen largest ovine arteries, of which seven represent the vessels excised from each of the eleven sheep (see Figure 7.4). The seven vessels from which pressure-area measurements were taken include the AA, PA, MA, DA, BT, CA, and FA. In addition, we included major vessels required to ensure an accurate distribution of flow. Additional proximal arteries included in the network model were the RA, the CM arteries. These vessels are important due to the large amount of flow that they carry. At rest the renal system receives about 20% of cardiac output, while the celiac and superior mesenteric vessels receive about 25% of the cardiac output [31, 82, 146]. Since the model was 1-D and these two groups of vessels are located at close proximity, we have modeled each group as

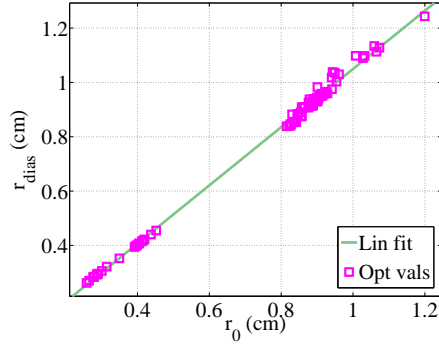


**Figure 7.2** Measured diastolic radius values plotted against the theoretical, optimized elastic zero-strain radius (pink squares) for each sheep in each vessel. Results are shown prior to averaging with the linear fit (green)  $r_{\text{dias}} = 1.1r_0 - 0.02$ .

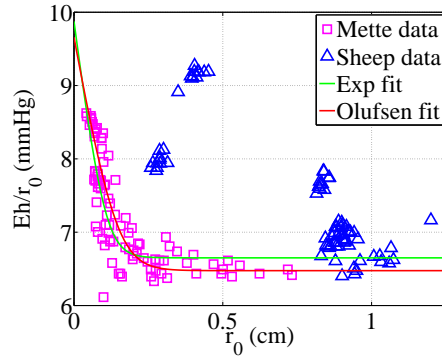


**Figure 7.3** Exponential decay function as the best fit for all data points on a semi-log graph. Digitized data from Olufsen's dissertation are shown by the magenta squares and sheep data is given by blue triangles. Exponential decay function parameters are  $k_1 = 4.7 \times 10^8$  mmHg,  $k_2 = -25.23$   $\text{cm}^{-1}$ , and  $k_3 = 756$  mmHg. The previous exponential fit found by Olufsen [111] is shown in red.

one vessel with a diameter reflecting the combined area of the vessels in the group. Additional distal branches include the left and right iliac artery and the median sacral artery, which regulates blood flow to the tail and the posterior surface of the rectum. The inferior mesenteric artery is known to branch off before the iliac bifurcation. Given its relatively close proximity to the tail and the fact that we have no data for this vessel, in the model, this vessel is combined with the median sacral artery (IT).

It is well known that the larger arteries, in particular the aorta, taper along their length [31].

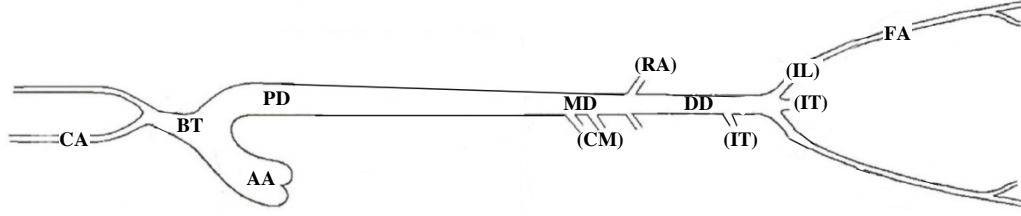


**Figure 7.4** The network geometry. The seven arteries from which pressure-area measurements have been taken are marked with letters (AA, BT, CA, PD, MD, DD, FA), while other major vessels are marked with letters in parenthesis (CM, RA, IL, IT). In the model, the renal arteries and the celiac and mesenteric arteries were each combined into a single vessel, and the carotid, iliac, and femoral bifurcations were modeled as symmetric.

To account for the taper we modeled the zero-strain radius  $r_0$  as

$$r_0(x) = r_{\text{prox}} \left( \frac{r_{\text{dist}}}{r_{\text{prox}}} \right)^{x/L}, \quad (7.2.1)$$

where  $x$  ( $0 \leq x \leq L$ ) is the position along the vessel of length  $L$  and  $r_{\text{prox}}$  and  $r_{\text{dist}}$  are the proximal and distal unstressed radii, respectively [111]. For the aorta, which is composed of four individual segments, the distal unstressed radius for each segment was set as the inlet radius of the successive segment. For each segment,  $r_{\text{prox}}$  and  $r_{\text{dist}}$  were determined using (7.2.1) combined with estimated values (see Table 7.1). For the CA, IL, and the external FA, where only one estimated value was available, we imposed a 5% taper of the unstressed radius between the proximal and distal vessel ends as found in [111]. The short vessels, the BT, RA, CM, as well as the IT, were assumed straight. No experimental data were available to define vessel lengths since each experimental study was performed *ex vivo* in a 6 cm segment extracted from the network. To ensure an adequately defined network, as shown in Table 7.2, average anatomic data were used to define lengths of each vessel segment [31, 82, 146].

When defining unstressed radii for vessels where no data were available, we used approximations from anatomic data, ensuring that junctions were designed to satisfy the constraint that the sum of the area of the daughter vessels exceeds the area of the parent vessel [111], i.e.

$$A_p(L, t) < \sum_i A_{d_i}(0, t).$$

The subscript  $p$  denotes the parent vessel associated with subsequent daughter vessels  $d_i$  such that  $A_p(L, t) > A_{d_i}(0, t)$  for each  $i = 1, 2, 3$ .

**Table 7.2** Vessel dimensions and flow distribution. For each vessel segment shown in Figure 7.4, the table specifies length, proximal and distal unstressed radius (all in cm), as well as the distribution of flow to the vessel segment [31, 82, 146]. The total cardiac output was set at 66.9 mL/s [40]. Unstressed vessel radii were averaged from optimal values presented in Table 7.1.

artery	abbreviation	length (cm)	proximal $r_0$ (cm)	distal $r_0$ (cm)	flow % of CO
Ascending aorta	AA	6.00	1.06	0.91	100
Brachiocephalic trunk	BT	3.80	0.92	0.92	14
Carotid artery	CA	5.39	0.42	0.40	7
Proximal descending aorta	PD	17.24	0.91	0.88	86
Medial descending aorta	MD	5.00	0.88	0.85	86
Distal descending aorta	DD	8.00	0.85	0.82	41
Renal artery	RA*	5.00	0.63	0.63	20
Celiac & superior mesenteric arteries	CM*	5.47	0.66	0.66	25
Common iliac artery	IL	2.24	0.51	0.28	10.5
Femoral artery	FA	9.40	0.28	0.27	10.5
Inferior mesenteric & median sacral arteries	IT*	4.00	0.54	0.50	20

\* The radius listed for the renal (RA), celiac and superior mesenteric (CM), and the median sacral artery and inferior mesenteric (IT) arteries have been calculated to match the combined area of both vessels in each group, and the flow distribution include flow to all vessels in the group.

## 7.3 Elastic network

As a starting point, the 1-D elastic network was constructed to ensure proof of concept for the simplest case and validate our discrete *ex vivo* data in a network setting. Results are shown below for a network designed to mimic “averaged” ovine arteries using averaged values of  $r_0$  and  $Eh$  based on the optimized parameters found in Section 7.1. Further discussion on the results in this section can be found in [16].

### 7.3.1 Model parameters

The 1-D fluid dynamics model presented herein incorporated a number of parameters including those specifying properties of the fluid, the nature of the flow, the vessel geometry,

the wall properties, and the outflow boundary conditions. Parameters were first calibrated in a fourteen vessel elastic network to validate the geometry and properties against averaged *ex vivo* data. All parameters along with their values and units are listed in Table 7.3. Parameters characterizing properties of the fluid include blood density  $\rho = 1.06$  g/mL and

**Table 7.3** Model parameters. Fluid dynamics parameters were used in both the single vessel (SV) and the network simulations. All vessels are listed in the large network but only terminal vessels require outflow boundary conditions (RCR values). Parameters noted n.d. are non dimensional.

Fluid dynamics parameters			
Fluid density	$\rho$	g/mL	1.06
Kinematic viscosity	$\nu$	g/s/cm	0.049
Velocity profile	$\delta$	n.d.	2

Vessel	$R_1$ (dynes s/cm <sup>5</sup> )	$R_2$ (dynes s/cm <sup>5</sup> )	$C_T$ (cm <sup>5</sup> / dynes)
AA (SV)	392	1320	$7.40 \times 10^{-4}$
AA	-	-	-
BT	-	-	-
CA	5172	20686	$5.18 \times 10^{-5}$
PD	-	-	-
MD	-	-	-
DD	-	-	-
RA	1810	7240	$1.48 \times 10^{-3}$
CM	1448	5792	$1.85 \times 10^{-3}$
IL	-	-	-
FA	3448	13791	$7.77 \times 10^{-5}$
IT	2336	9342	$1.15 \times 10^{-4}$

viscosity  $\nu = 0.049$  g/s/cm [160]. Two parameters were needed to specify the flow,  $\delta$  specifying the velocity profile and the temporal inflow profile applied to the system. In this study we assumed that  $\delta = 2$ , though it is believed [98] that for larger vessels the velocity profile is more blunt, indicating that a larger value may be more appropriate. A generic velocity profile was scaled to give an average adult sheep cardiac output of 70 mL/min [40].

### 7.3.2 Network simulations

Network simulations were performed in a model composed of the fourteen largest ovine arteries with the ascending aorta serving as the inlet to the network. For the network simulations, we applied the temporal inflow profile found in the single vessel simulations presented in the next section and shown in Figure 7.9. Vessel lengths and unstressed radii were set as discussed in Section 7.3.1, while the larger vessels ( $r_0 > 0.8$  cm) were assumed elastic with stiffness predicted using (7.1.2). Constant stiffness (values shown in Table 7.1) was assumed for smaller vessels (CA and FA). Outflow boundary conditions were specified by the 3-element WK model. The total network resistance was set equal to the total resistance of the single vessel segment, split according to flow distributions given in Table 7.2. For each branch  $i$ , the  $R_{1i} = 0.2R_{Ti}$  and  $R_{Ti} = R_{1i} + R_{2i}$  where  $R_{Ti} = \bar{p}_i/\bar{q}_i$ . The total compliance was calculated relative to the total resistance for that branch using Alastruey's equation [3]  $R_{Ti}C_{Ti} = 1.34s$ .

Figure 7.5 shows simulation results in the network. The figure shows temporal flow profiles predicted where measurements were available or at the center of vessel (where no data were available). We also show pressure-area predictions, for vessels where pressure-area measurements were available, and elastic model results are plotted together with the data. It should be noted that these results are shown without optimizing the network model parameters. Note that at all locations, the model predictions closely follow average values from measurements based on. Lastly, Figure 7.6 shows wave propagation of flow and pressure along the aorta. This also demonstrates the adequacy of *ex vivo* data from discrete locations in mimicking network scenarios.

## 7.4 Viscoelastic network

It is evident that there is an increase in the amount of energy dissipated in a network when incorporating viscoelasticity in the wall model. This proves to be a challenge in developing a viscoelastic network and something we aim to investigate. To begin accounting for the energy lost due to viscoelasticity, we construct networks mimicking arterial geometries and determine how boundary conditions can be used to compensate for the energy lost upstream. This section will present small viscoelastic networks that are used to construct a systematic approach for determining outflow parameters as the networks increase in complexity and size.

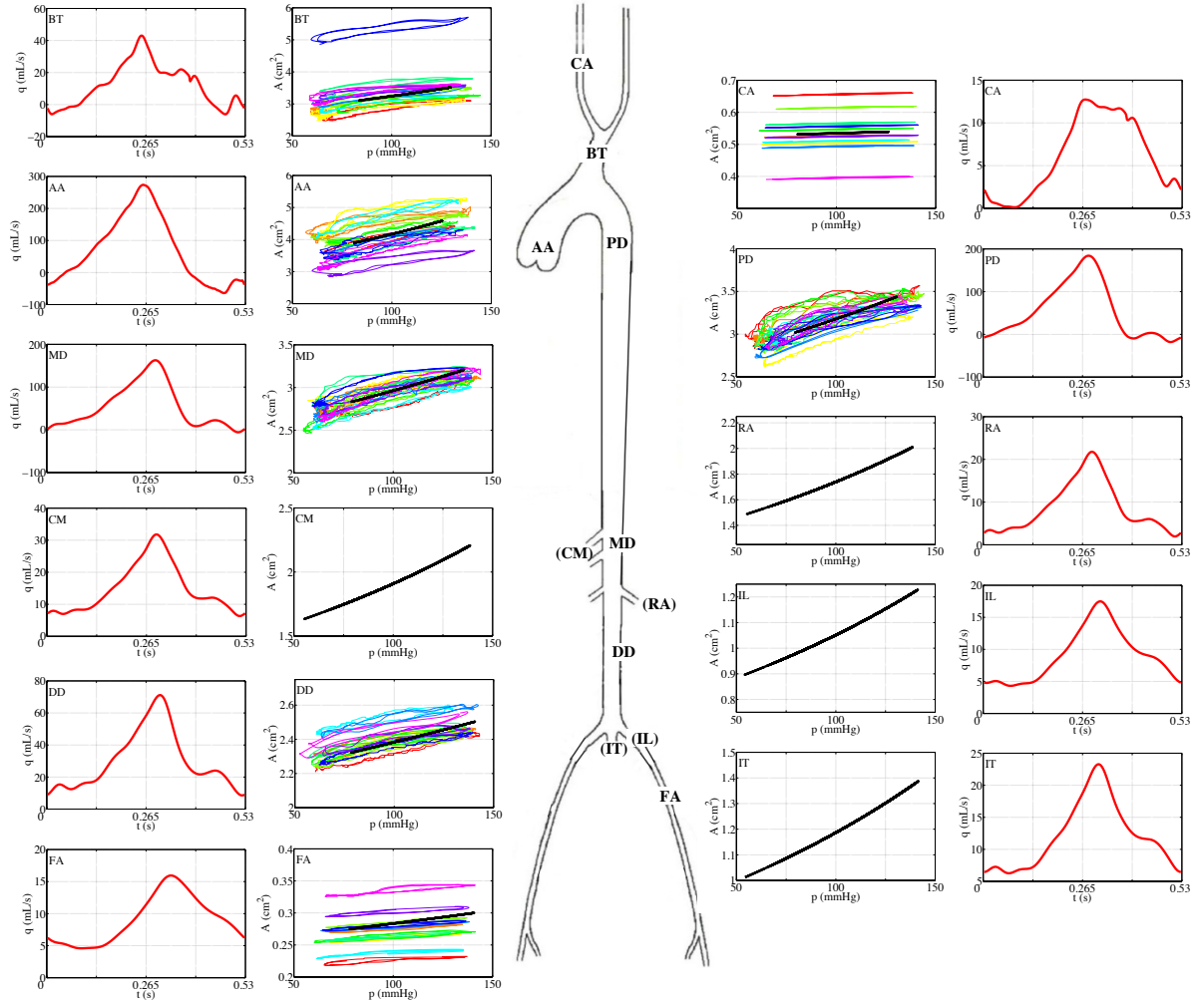


**Figure 7.5** Flow and pressure-area computations and data for each vessel in the network. Different colors show measurements and correspond to individual sheep data. Black lines indicate pressure-area results from the simulations. Data were not available from the CM, RA, IL, IT. A good approximation to the flow distribution in each artery is found in the simulations based on values found in literature [31, 82, 146] and listed in Table 7.2.

As noted by Mahdi et al. [94], the parameters in the 3-element WK model are structurally unidentifiable. This means that the usual parameter estimation routines do not necessarily guarantee uniqueness, and thus we approach the problem of estimating boundary conditions using a manual systematic approach. This is achieved by first estimating the WK parameters as described by McDonald and Attinger [99] and Alastruey [3] which we have shown are valid for elastic networks. The pulse pressure and mean pressure are

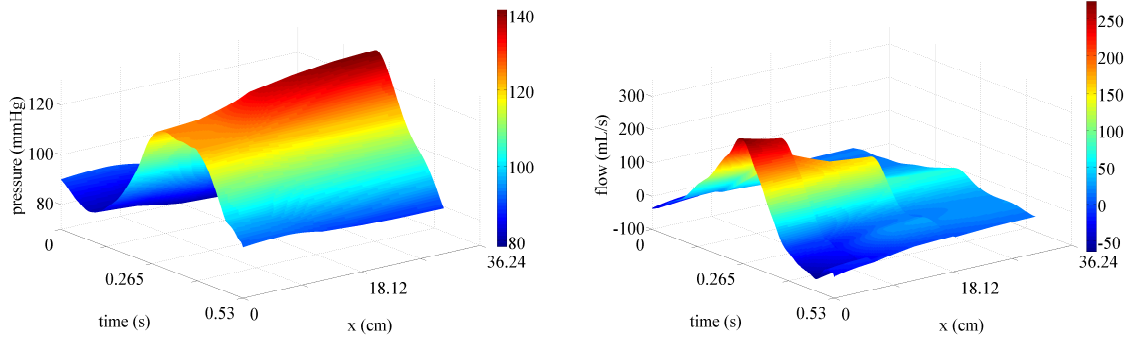


**Figure 7.6** Pressure and flow waveforms along the aorta in an elastic network. Systolic pressure increases progressing toward the periphery.

recorded based on using these outflow values and then adjusted to achieve a pulse and mean pressure of approximately 41 and 97 mmHg, respectively, matching the pulse and mean pressure from one set of sheep data. The first step in this approach, however, is to study the effect each WK parameter has on the system in a single vessel.

### 7.4.1 Single vessel network

A 6 cm straight vessel representative of the ascending aorta is the single vessel we will study (Figure 7.7). Fluid dynamics parameters were set as discussed in Section 7.3 (Table 7.3). The unstressed vessel radius  $r_0$ , vessel stiffness  $E$ , and viscoelastic parameters  $A_1$  and  $b_1$  (listed in Table 7.1) were predicted by minimizing the least squares error (7.1.1) between computed and measured vessel area for data from the ascending aorta in one sheep, see Figure 7.8.

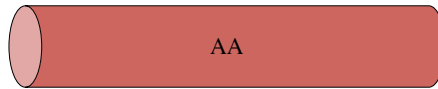


**Figure 7.7** Single non-tapered vessel representative of the ascending aorta where we have assumed a non-tapering vessel. This geometry is used to study the affects of the in- and outflow boundary conditions.

Wall model and viscoelastic parameters were estimated using a 0-D model, minimizing



the least squares area between computed and measured vessel area using blood pressure data as an input, i.e. without accounting for the effect of the fluid flow. No information about flow was available, thus measured blood pressure was applied at the inlet. Initial values for the outflow parameters  $R_1, R_2, C_T$  were set as discussed earlier. The total resistance  $R_T = \bar{p}/\bar{q}$  was predicted from mean pressure over mean flow, set using average values reported in literature for male Merino sheep [40]. The characteristic resistance was initially  $R_1 = \frac{\rho c_0}{A_0}$  [182], a function of  $c_0$  wave speed at diastole, leading to  $R_2 = R_T - R_1$ . Initially,  $C_T$  was predicted from  $R_T C_T = 1.34s$  as suggested by Alastruey et al. [3].

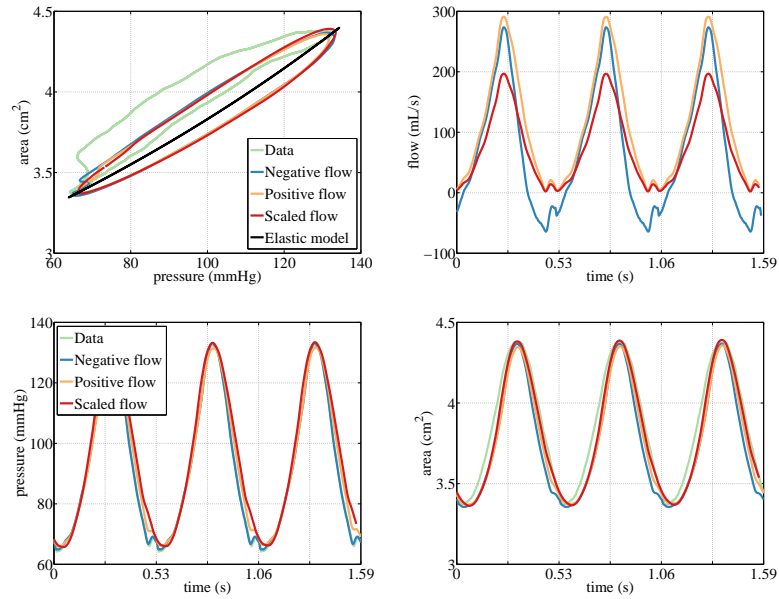


**Figure 7.8** Model predictions in a single vessel (the ascending aorta) mimicking results from a specific sheep. Using one set of data recorded in the ascending aorta, the parameters for the viscoelastic wall model were optimized and then used in the fluids model. The pressure data as the inflow boundary condition produced a negative, unrealistic flow (blue) so parameters were adjusted to produce a non-negative flow (orange) which was used as the inflow boundary condition. This flow had a cardiac output exceeding the values reported in literature thus requiring the flow be scaled (red) and used as the inflow boundary condition. Results from the three inflow boundary conditions (negative, positive, scaled) with the viscoelastic wall model are shown.

To understand how the coupled pressure, area, and flow predicted by the model vary with parameters, we included a number of simulations varying the inflow, outflow param-

eters  $R_i$  and  $C_T$ , and viscoelastic parameters  $b_1, A_1$ .

Based on the pumping of the heart, the most natural inlet boundary condition is to apply flow. For this study, no flow measurements were available. As a result we used measured blood pressure at the inlet and predicted the corresponding flow (shown in Figure 7.8). This flow matches cardiac output  $\bar{q}$  used when setting total resistance  $R_T$  at the vessel outlet, but the flow becomes negative towards the end of diastole. A small negative flow can be expected physiologically, reflecting a reversed flow into the heart upon valve closure [7], though the negative flow obtained using the pressure inlet is too large. As noted by [9], negative flow is often observed when blood pressure is applied at the inlet and can, in part, occur because the model does not perfectly represent the vessel in which data was collected. Errors are expected both in parameter estimates and measurements. To investigate this further, we modified outflow parameters, showing that increasing either  $R_T$ ,  $C_T$ , or a combination of both can lead to simulations in which the flow becomes positive, while area and pressure data are still matched. The parameter modifications led to a flow corresponding to a cardiac output that was too high and the associated parameter values were not physiological. We also tried changing wall parameters (wall stiffness and zero-strain radius), but these variations did not allow us to predict a positive flow while simultaneously being able to accurately predict measured area and pressure. Finally, we showed that it is possible to scale the positive flow, yielding a cardiac output appropriate for sheep, but again, parameter modifications needed to predict measured vessel area were outside the physiological range. This scaled flow (shown in Figure 7.8 by the blue line) is used as our inflow profile throughout the remainder of this thesis.

Next, we analyzed the impacts of modulating outflow boundary conditions using the predicted flow at the inlet. Results of these simulations show that decreasing the total resistance  $R_T$  (by decreasing  $R_2$  while keeping  $R_1$  constant) leads to a decrease in diastolic values, while changing the ratio of  $R_1$  to  $R_2$  maintains the same diastolic value whereas systolic blood pressure is increased. Overall,  $R_1$  has a bigger impact on pulse pressure while  $R_2$  contributes more to determining mean pressure. Results of these studies are shown in Figure 7.9. Additionally, we investigated the effect of changing total outflow compliance compared to changes in vessel stiffness (the inverse of vessel compliance). Results of these simulations (see Figure 7.10) show, as expected, that changing the total compliance downstream impacts the decay during diastole but does not have a major impact on upstream pulse or mean pressure. A smaller value of  $C_T$  gives rise to a faster decay, though the hys-

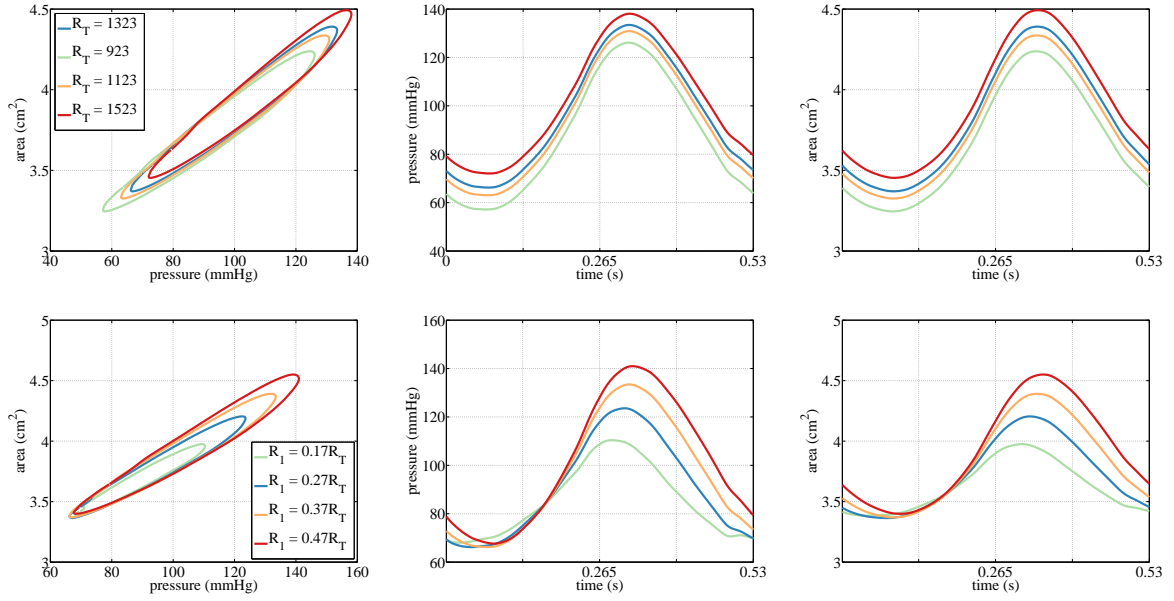


**Figure 7.9** Effect of changing the WK parameters in a single vessel network. If  $R_T$  is decreased (by decreasing  $R_2$ ) for a fixed inflow (top), the loop is shifted down towards the left, i.e. both systolic and diastolic values are decreased. The ratio of the proximal resistor to the total branch resistance is varied (bottom) with a range of  $R_1/R_T = 0.2 = 17$  to  $R_1/R_T = 0.47$ , showing that changing the ratio maintains the diastolic values while varying the systolic values.

teretic loop size does not change significantly. On the other hand, increasing vessel stiffness changes the slope of the pressure-area loop, significantly increasing pulse pressure and with a slight increase in mean pressure. Figure 7.10 shows comparison of changes in downstream compliance compared to changes in vessel stiffness. In addition to actual flow, pressure, and area profiles we also included a graph showing changes in pulse pressure. Finally, we investigated the effect of changing the  $A_1$  parameter which accounts for viscoelasticity in the arterial wall. A purely elastic wall ( $A_1 = 0$ ) produces a larger pulse pressure, thus overshooting both the diastolic and systolic pressure values. Additionally, elastic walls do not demonstrate the experimentally observed pressure-area hysteresis loop, but rather elastic walls provide a simple injective relation between pressure and area as shown in Figure 7.11.

First, we consider a single vessel with varying degrees of viscoelasticity (provided by increasing the  $A_1$  parameter discussed in Section 4.2.) As clearly seen in Figure 7.11, pulse pressure decreases as viscoelasticity increases, causing a similar effect in the area results.

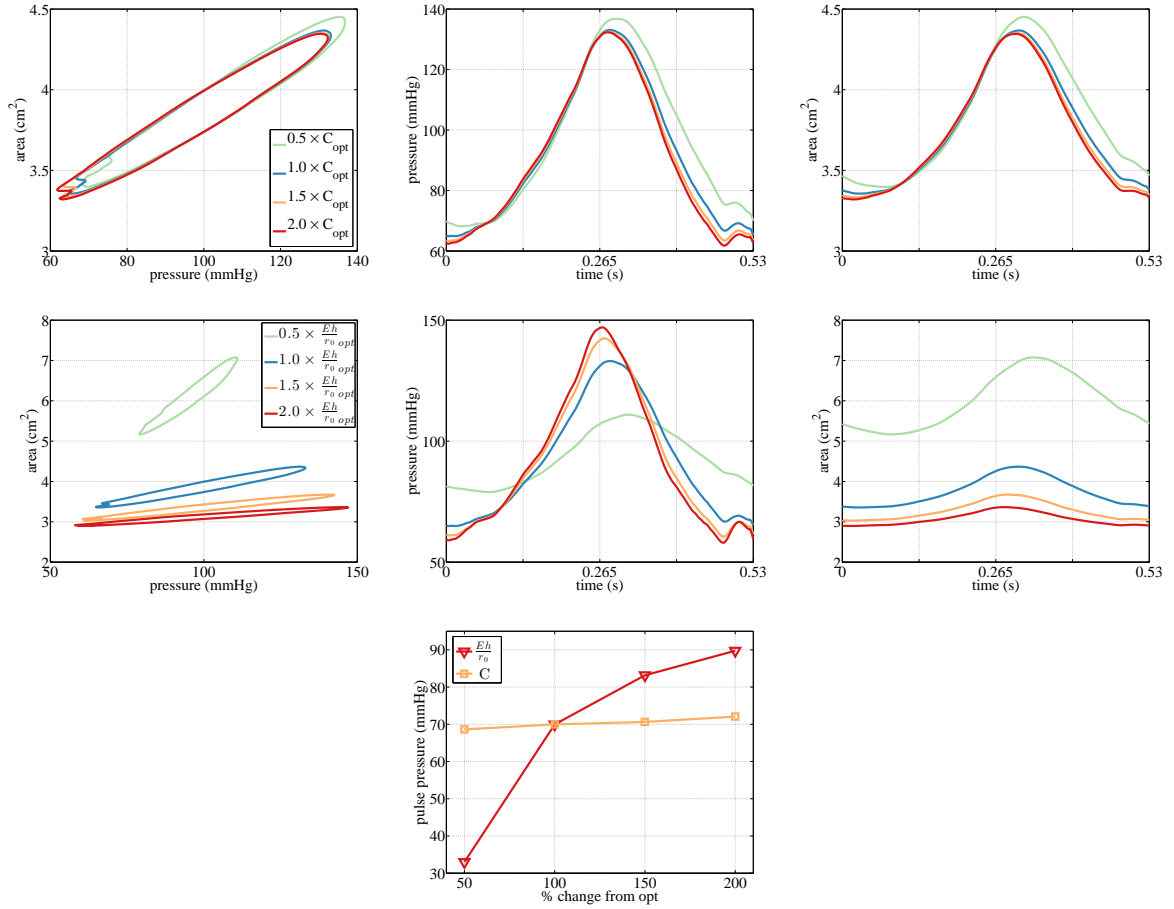


**Figure 7.10** Effect of changing the compliance parameter values. The compliance in the downstream vasculature is represented by the capacitance parameter ( $C$ ) in the WK model. Varying the capacitance in the WK model (top) affects the shape of the diastolic decay while also slightly altering the pulse pressure. Vessel compliance, given by  $Eh/r_0$ , has a much greater effect on the pressure and area results (middle). The differences in pulse pressure observed by varying  $C$  and  $Eh/r_0$  are shown for a quick comparison (bottom).

Because the energy isn't fully recovered after vessel dilation, the lower pressure values are expected. To account for the energy lost due to the wall model, we can adjust the downstream vasculature represented by the 3-element WK model. In our previous study, it was noted that  $R_1$  most closely determines pulse pressure while  $R_2$  dictates mean pressure. Our initial study set out to match these two quantities individually: pulse pressure and mean pressure. Two separate simulations were run: one to match pulse pressure while neglecting mean pressure and vice versa. While matching pulse pressure,  $R_2$  remained constant

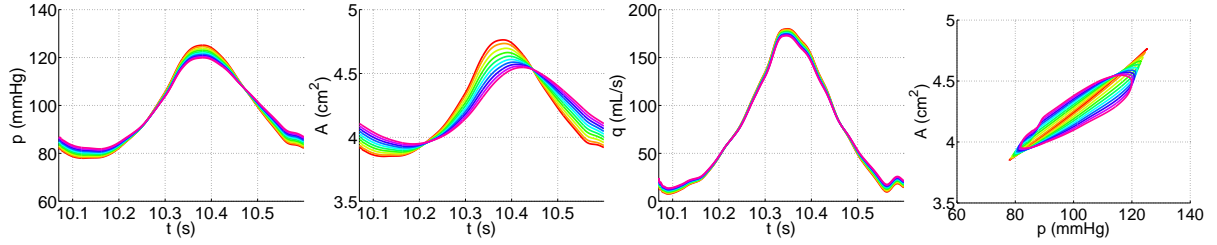


**Figure 7.11** Effect of changing wall viscosity while keeping outflow boundary conditions constant.  $A_1$  ranges from 0 (corresponding to an elastic wall) to 0.867 in spectrum order. As  $A_1$  increases, a decrease in pulse pressure is observed.

while  $R_1$  varied, and while matching mean pressure,  $R_1$  remained constant while  $R_2$  was allowed to change. In both cases, this means that the total resistance fluctuated. Results for matching pulse and mean pressure separately are shown in Figure 7.12.

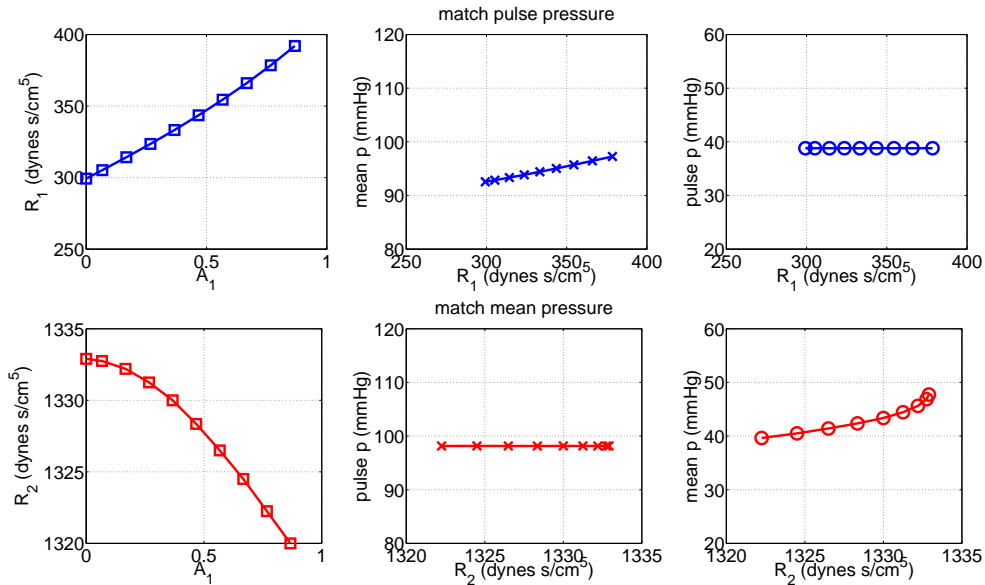


**Figure 7.12** (Top) Results for matching pulse pressure in a single vessel. By increasing the peripheral resistance in the WK model as wall viscoelasticity increases, we are able to obtain the same pulse pressure but mean pressure increases. (Bottom) Results for matching mean pressure in a single vessel. As wall viscoelasticity increases, the distal resistance in the WK model must decrease in order to maintain the same mean pressure. However, this simultaneously leads to an increase in pulse pressure.

The next simulations with the single vessel network sought to match both pulse and mean pressure simultaneously. Although the values used to produce the results in Figure 7.12 could not be directly applied, the same general trend for both  $R_1$  and  $R_2$  was found; as we increased the value of  $A_1$ ,  $R_1$  needed to be increased while  $R_2$  decreased. Of importance to note is that the total resistance,  $R_T$  remained constant despite changing  $R_1$  and  $R_2$  (Figure 7.13).

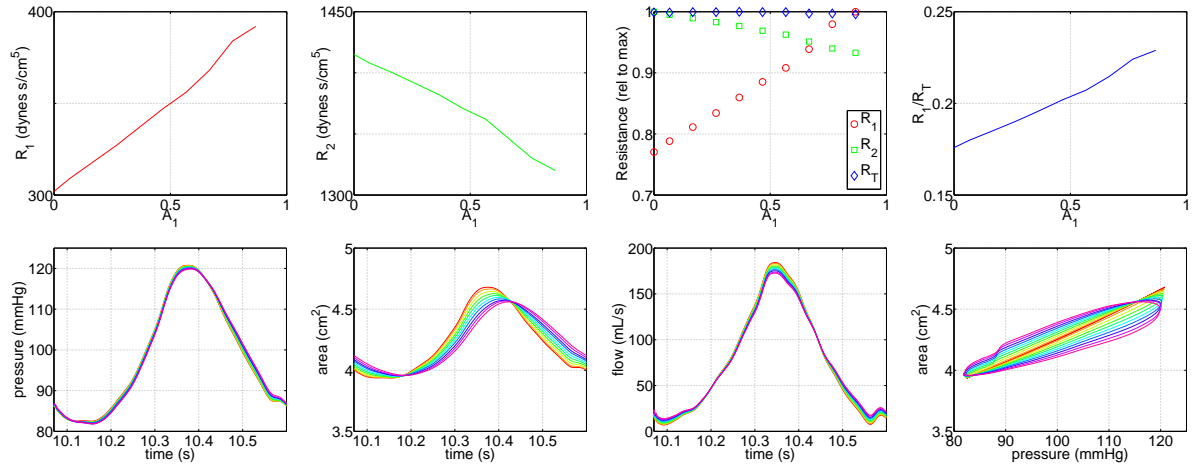


**Figure 7.13** Increasing wall viscoelasticity while maintaining constant pulse and mean pressures requires an increase in proximal resistance and a decrease in distal resistance of the WK model, conserving the total resistance. The  $R_1/R_T$  ratio, previously taken to be 0.2 [99], is directly correlated with wall viscoelasticity. As seen in the left bottom row, matching pulse pressure and mean pressure maintains pressure shape and size.

In the single vessel case, we can see that the previous notions for determining WK parameters no longer apply when viscoelastic wall models are used. Further simulations with larger viscoelastic networks are necessary to truly uncover a systematic approach for finding WK parameters.

## 7.4.2 Symmetric branching networks

We begin the study of viscoelastic networks by examining symmetric bifurcations. Due to the symmetric structure, reflected waves propagate at the same speed from the periphery and thus hit the forward propagating wave at the same location and time. Networks

containing only symmetric bifurcations require the same set of WK parameters applied to each terminal vessel, thus we need only estimate 2 parameters:  $R_1$  and  $R_2$ . We will consider 3 network geometries – 3 vessels, 7 vessels, and 15 vessels (shown in Figure 7.14) – each with a parent vessel whose radius is 0.95 cm. Additionally, we will assume that each bifurcation follows the relation

$$r_p^\zeta = r_{d_1}^\zeta + r_{d_2}^\zeta$$

where  $\zeta = 2.15$  for the 7 vessel and 15 vessel networks. Note that this value differs from Murray's Law which states  $\zeta = 3$ . This is due to values of  $\zeta$  taken from multiple sources [42, 111, 147] based on arterial geometries.

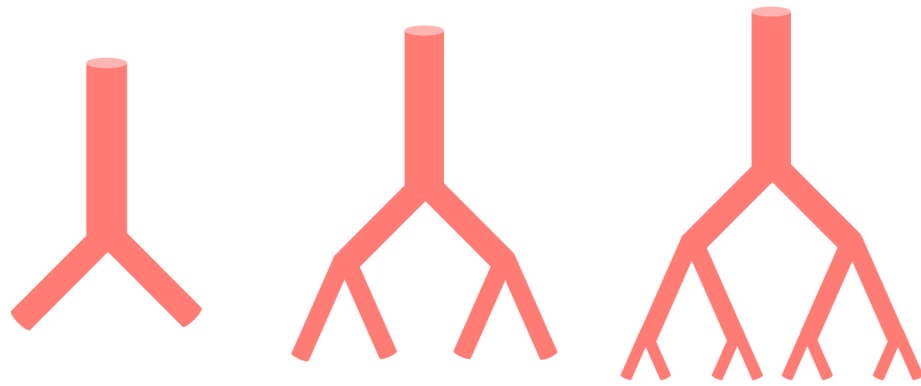


**Figure 7.14** Symmetric geometries used to determine WK parameters in viscoelastic networks. From left to right: 3-, 7-, and 15-vessel networks. Note that these are representative and do not reflect the actual geometries.

#### 7.4.2.1 Constant $Eh/r_0$ values

As we begin to study the 3 vessel symmetric network, different values of  $\zeta$  are chosen to see how this affects the boundary conditions as we increase viscoelasticity;  $\zeta \in \{2, 2.15, 2.32, 2.95, 4.82\}$ , noting that 4.82 is unphysiological and used for purely simulation purposes. As we increase  $\zeta$ , we see that proximal resistance must be increased to maintain pulse and mean pressure values (Figure 7.15). An increase in  $A_1$  requires exponentially greater in  $R_2$  values in order to maintain our pressure waveform while  $R_1$  increases linearly. This causes a drastic de-

crease in our  $R_1/R_T$  ratio, venturing away from the historically used 0.2 [99]. We can write our resistances as functions of  $\zeta$  and  $A_1$ :

$$R_1 = a + bA_1 + c\zeta + dA_1^2 + e\zeta A_1 \quad (7.4.1)$$

$$R_2 = f\zeta \exp(g\zeta A_1^2) + h \exp(k\zeta) \quad (7.4.2)$$

where  $a = 794.3$ ,  $b = 191.1$ ,  $c = 68.6$ ,  $d = -133.4$ ,  $e = 137.5$ ,  $f = 652.3$ ,  $g = 5.0$ ,  $h = 6598$ , and  $k = -0.5$ . Following this study,  $\zeta$  will be fixed at 2.15 for the symmetric branching networks based on the value used in [111].

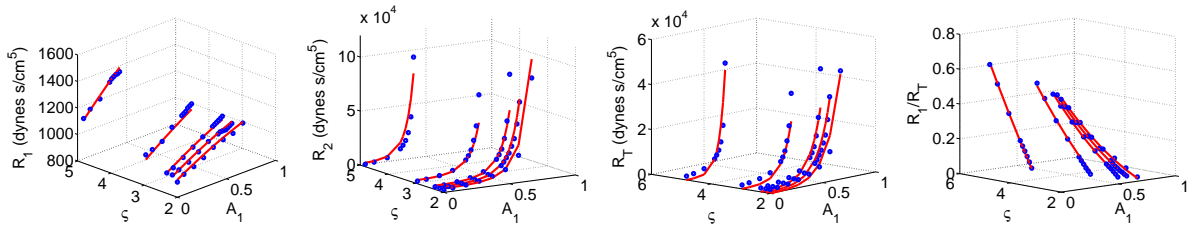


**Figure 7.15**  $R_1$  and  $R_2$  associated with each daughter vessel plotted as functions of  $\zeta$  and  $A_1$ . The total network resistance is defined as  $2R_{T_d}$  where  $R_{T_d} = R_1 + R_2$  as shown in the figures. Red lines show the functions given by (7.4.1) and (7.4.2).

The 7- and 15-vessel network parameters were found in a similar manner, noting that both values of  $R_1$  and  $R_2$  for each individual WK increased as the number of vessels increased. This is logical when considering how total resistance  $R_T$  is calculated in parallel circuits:

$$\frac{1}{R_T} = \sum_{i=1}^n \frac{1}{R_i} \quad (7.4.3)$$

where  $R_i$  are resistors in parallel as shown in Figure 7.16.

Results for individual WK resistances for each of the 3 networks are shown in Table 7.4. It is important to note that values for  $R_1$  and  $R_2$  are valid for each WK element applied to each terminal vessel. These are not the total resistances for the network. Total resistances for the 3 networks are shown as viscoelasticity increases in Figure 7.17. An interesting observation lies in analyzing how  $R_1$  changes in each network; for both the single vessel and the 3-vessel networks,  $R_1$  increases as viscoelasticity increases. We hypothesize that the ter-



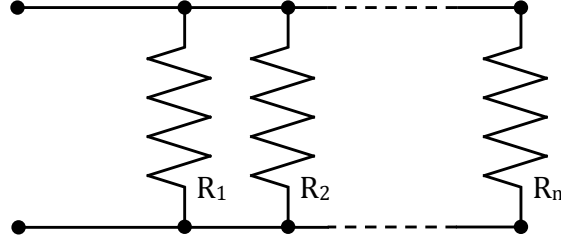


**Figure 7.16** A circuit of resistors  $R_1, R_2, \dots, R_n$  in parallel. The total resistance of the circuit can be calculated using (7.4.3).

terminal vessels are too large and not stiff enough in these networks to account for a realistic network. As more generations are added in the 7- and 15-vessel networks, the terminal vessels decrease in size, providing more resistance to flow by radius size alone.

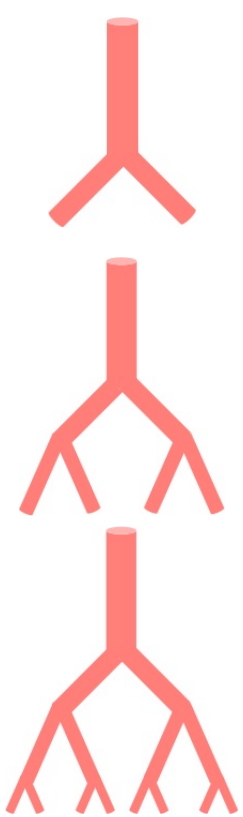
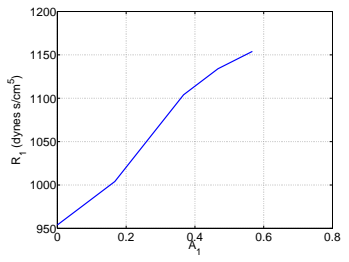
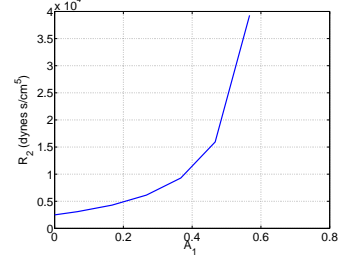
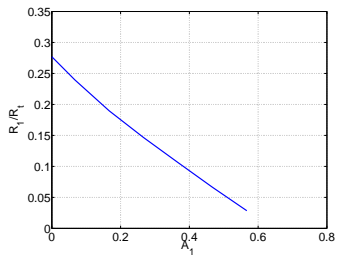
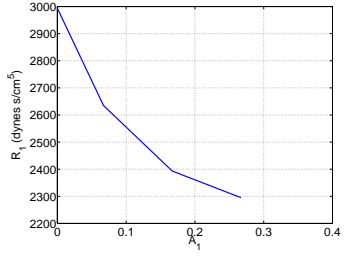
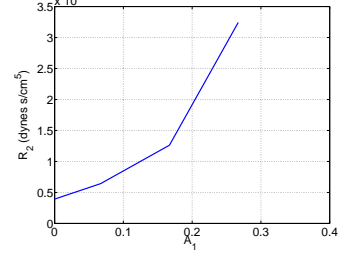
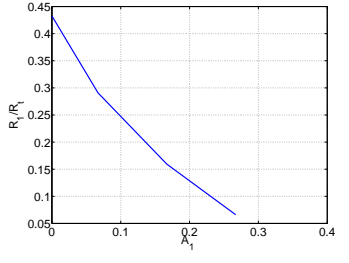
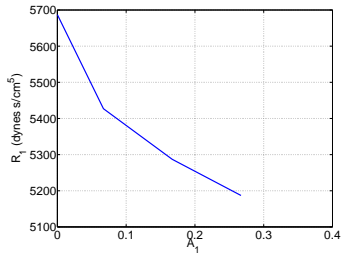
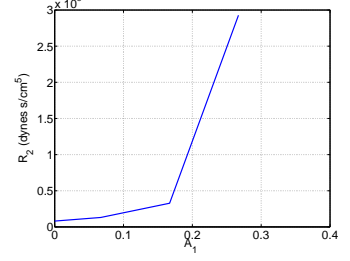
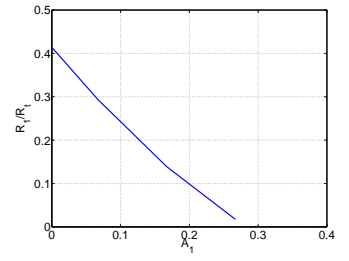
Based on the results shown above for the 3 symmetric geometries, we can determine  $R_1$  and  $R_2$  as functions of  $A_1$  and  $r_0$ . For the symmetric case,  $r_0$  discretely represents the value of  $\zeta$  and the number of viscoelastic vessels in the network structure, i.e. if given  $r_0$ ,  $\zeta$  could be calculated for each generation of branching and the number of vessels in the network could be tallied from this. The formulas found to determine the proximal and distal resistors based on viscoelasticity and root radius are (Figure 7.20)

$$R_1 = a + b r_0 + c A_1 + d r_0^2 + e r_0 A_1 + f A_1^2 \quad (7.4.4)$$

$$R_2 = \tilde{a} \exp(\tilde{b} r_0^2 + \tilde{c} A_1) + \tilde{d} \exp(\tilde{e} A_1^2) \quad (7.4.5)$$

where the parameter values and units are given in Table 7.5. These results are for the simplest case scenario where each bifurcation is symmetric and the elastic modulus-to-radius ratio  $Eh/r_0$  is constant and equal for all vessels.

**Table 7.4** Results for each of the symmetric networks where  $Eh/r_0$  is constant throughout the vasculature. The increasing  $R_1$  trend observed in the single vessel and 3-vessel network changes as more generations are added. However, the trends for  $R_2$  and  $R_1/R_t$  remain the same for the symmetric bifurcating networks.

network	$r_{\text{root}}$ (cm)	$R_1$	$R_2$	$R_1/R_t$
	0.69			
	0.50			
	0.36			

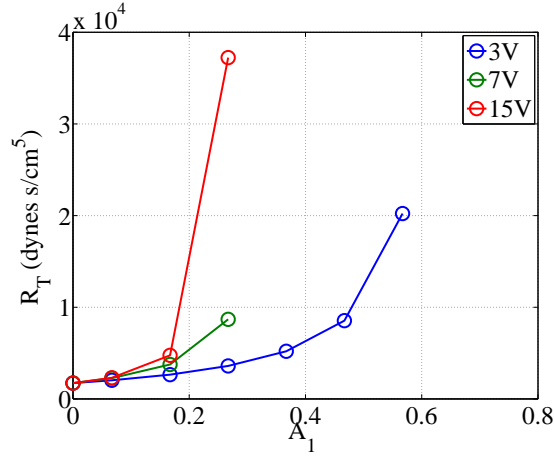


**Figure 7.17** Total resistance in each symmetric network for increasing values of  $A_1$ . It is important to note that when  $A_1 = 0$ , corresponding to a purely elastic wall, the networks have the same total resistance. This supports our hypothesis that as viscoelastic vessels are added into a network, more energy is lost and thus higher resistances are needed at the outflow boundary conditions to account for these losses. The total resistance corresponding to the elastic models matches the total resistance found in the single vessel network and is equal to the mean pressure divided by the mean flow ( $R_T = \bar{p}/\bar{q}$ ).

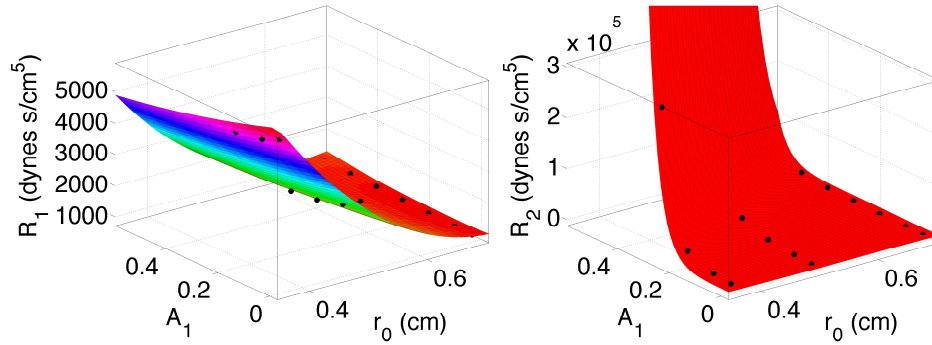


**Figure 7.18**  $R_1$  (left) and  $R_2$  (right) as functions of  $A_1$  and  $r_0$  for symmetric networks where  $Eh/r_0$  is the same in all vessels.  $R_1$  is a second-order polynomial in  $A_1$  and  $r_0$  whereas  $R_2$  is the sum of two exponentials containing  $A_1$  and  $r_0$ . As  $A_1$  increases, we see the exponential increase in  $R_2$  which makes large values of  $A_1$  physiologically unfeasible for the given network setup.

**Table 7.5** Parameter values and units for (7.4.4) and (7.4.5). The notation n.d. indicates non-dimensional quantities.

	$R_1$					
parameter	$a$	$b$	$c$	$d$	$e$	$f$
value	20180	-53550	-5341	37360	7179	1260
	$R_2$					
parameter	$\tilde{a}$	$\tilde{b}$	$\tilde{c}$	$\tilde{d}$	$\tilde{e}$	
value	8039	-26	26	2895	3	

#### 7.4.2.2 Varying $Eh/r_0$ values

Slightly increasing in complexity, we look at the same geometries (3-, 7-, and 15-vessel networks) while  $Eh/r_0$  varies with radius size as given by (7.1.2) and shown in Figure 7.3. Based on this relation, each generation of branching contains vessels of the same stiffness, but stiffness varies between generations, i.e. the higher the generation number, the stiffer vessels are. This is more representative of an actual arterial network where peripheral vessels are stiffer than those proximal to the heart.

The same procedure is used to find the WK models; WK parameters are initially determined as  $R_T = \bar{p}/\bar{q}$  where  $R_1 = 0.2R_T$  and then varied until a mean pressure of 97 mmHg and a pulse pressure of 41 mmHg is obtained.

Smaller, more reasonable resistances are found in this case, further supporting the need to vary vessel stiffness in models of the arterial network. As shown in Table 7.6, all vessels experience similar trends with an increase in viscoelasticity; this is different from the previous case. The ratio  $R_1/R_T$  for the elastic model ( $A_1 = 0$ ) is closer to the estimated value 0.2 by McDonald and Attinger [99] than the ratios relating to constant  $Eh/r_0$  values. However, our hypothesis that the number of vessels increases the energy lost in a network is confirmed by Figure 7.19 which shows the total resistance necessary for each of the three networks.

Similar functions defining  $R_1$  and  $R_2$  based on  $A_1$  and  $r_0$  were found in this case. As evidenced by Section 7.4.2.1, stiffness does play an important role in determining these functions and thus this function is specific for vessels whose stiffness can be modeled us-

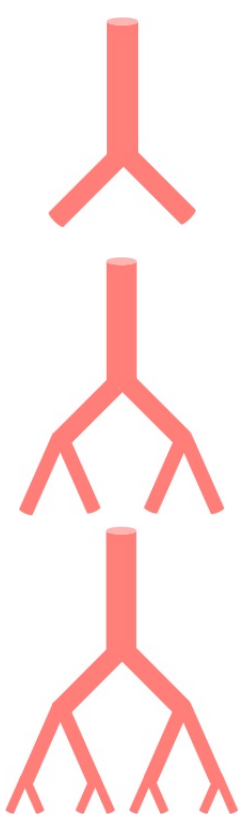
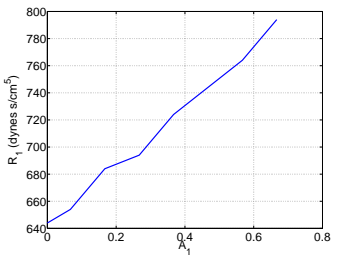
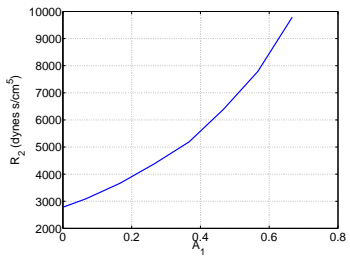
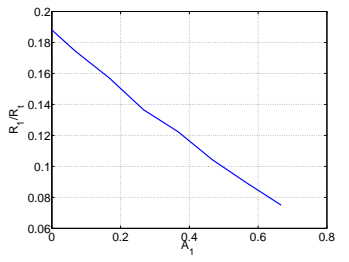
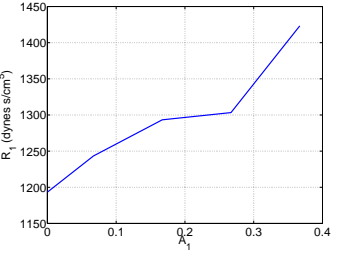
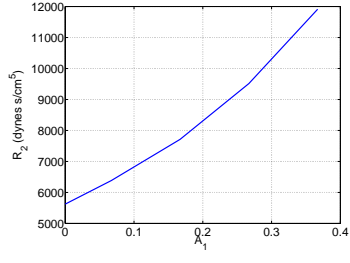
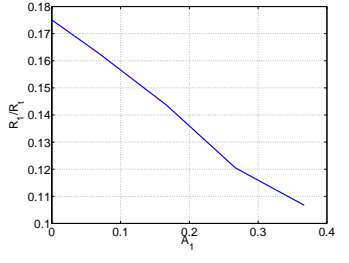
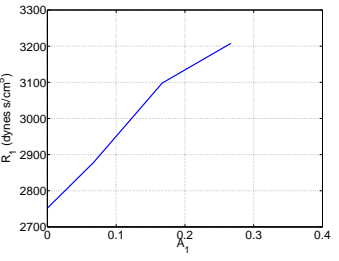
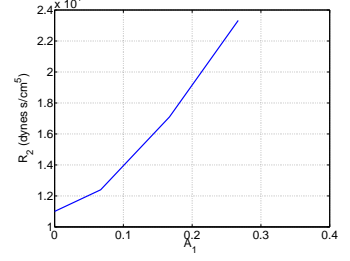
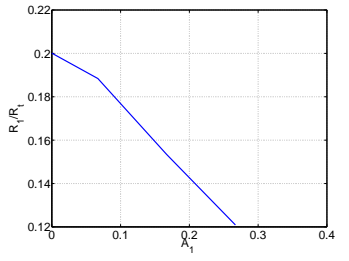
ing the equation graphed in Figure 7.3. The functions (Figure 7.20) are defined as

$$R_1 = a + b r_0 + c A_1 + d r_0^2 + e A_1 r_0. \quad (7.4.6)$$

$$R_2 = \tilde{a} + \tilde{b} r_0 + \tilde{c} A_1 + \tilde{d} r_0^2 + \tilde{e} A_1 r_0 + \tilde{f} A_1^2. \quad (7.4.7)$$

where the parameter values are listed in Table 7.7. These functions, mimicking how stiffness changes in a healthy arterial network, can then be used to determine the WK parameter values for our ovine arterial network simulation.

**Table 7.6** Results for each of the symmetric networks where  $Eh/r_0$  varies based on  $r_0$  throughout the vasculature.  $R_1$  now increases for all networks as viscoelastic degree ( $A_1$ ) is increased. However, the trends for  $R_2$  and  $R_1/R_T$  remain the same for the symmetric bifurcating networks.

network	$r_{\text{root}}$ (cm)	$R_1$	$R_2$	$R_1/R_T$
	0.69			
	0.50			
	0.36			

**Table 7.7** Parameter values and units for (7.4.6) and (7.4.7) relating  $R_1$  and  $R_2$  to  $A_1$  and  $r_0$  for symmetric networks where  $Eh/r_0$  varies with  $r_0$ .

	$R_1$					
parameter	$a$	$b$	$c$	$d$	$e$	
value	11830	-34710	1608	26820	-2019	
	$R_2$					
parameter	$\tilde{a}$	$\tilde{b}$	$\tilde{c}$	$\tilde{d}$	$\tilde{e}$	$\tilde{f}$
value	40120	-109900	40360	81170	-56490	13010

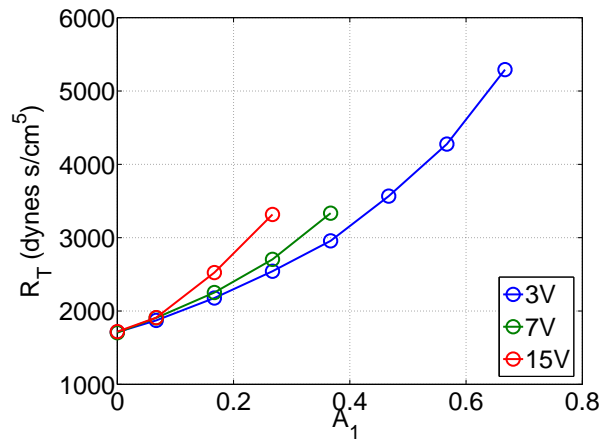


**Figure 7.19** Total resistance in each symmetric network for increasing values of  $A_1$ . Again, the total resistance remains the same in each network for the elastic wall model and can be found via  $R_T = \bar{p}/\bar{q}$ . As more viscoelastic vessels are added to the network, higher resistances are needed in the WK models to account for energy losses due to the wall model.

## 7.5 WIA results

WIA is used in the single vessel to determine whether arterial stiffness ( $Eh/r_0$ ) or wall viscoelasticity ( $A_1$ ) plays a bigger role in determining wave propagation effects. Throughout these simulations WK parameters are kept constant at  $R_1 = 304$  dynes s/cm<sup>5</sup>,  $R_2 = 1415$  dynes s/cm<sup>5</sup>, and  $C = 0.0007403$  cm<sup>5</sup>/ (s dynes) based on the values found for the largest  $A_1$  value in Section 7.4.1. To determine the impact that arterial stiffness has on wave re-

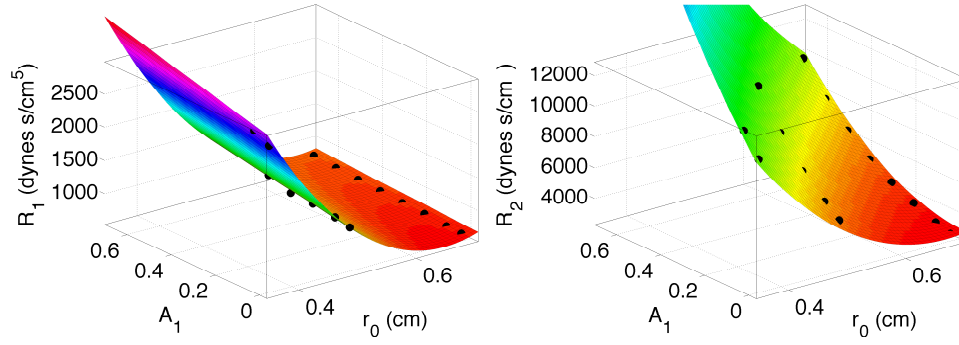


**Figure 7.20**  $R_1$  (left) and  $R_2$  (right) as functions of  $A_1$  and  $r_0$  for symmetric networks where  $Eh/r_0$  is the same in all vessels. Both  $R_1$  and  $R_2$  are defined as second-order polynomials in  $A_1$  and  $r_0$ .

flections, an elastic wall model is used while  $Eh/r_0$  varies. Next,  $Eh/r_0$  is held constant at 545 mmHg and the degree of viscoelasticity increases. WIA is performed on both tests with results shown in Figure 7.21.

Based on WIA, it appears that vessel stiffness has a larger influence on wave propagation than wall viscoelasticity. From this, an argument can be made for using purely elastic wall when modeling pulse wave propagation the arterial network. However, if the goal is to accurately represent pressure-area data, an elastic wall model is unable to capture the hysteretic effect that many experimental studies have found. In studying hypertension where the etiology is unknown, both perspectives may be able to provide further insight into the progression of hypertension. Modeling arterial walls accurately requires viscoelasticity which may change with hypertension. Simultaneously wave propagation must be studied due to the change in waveforms that appear in hypertensive networks.

Next, WIA is used to analyze the differences in wave propagation between networks where  $Eh/r_0$  is constant and where  $Eh/r_0$  varies with  $r_0$ . Each network is studied, noting that the 3-vessel network displays interesting results (Figure 7.22). In both cases as viscoelasticity increases, velocity decreases. This is different from the results corresponding to the 7- and 15-vessel networks (Figures 7.23 and 7.24, respectively). For all symmetric networks studied, reflections are more varied with viscoelasticity in the case of constant  $Eh/r_0$  throughout the network as evidenced by the WI graphs. However, WI (bottom right graph in Figures 7.22, 7.23, and 7.24) is the same for all degrees of viscoelasticity, confirming that the method used to obtain WK parameters preserves wave shape and type.

WIA was performed on the elastic network results shown in Figure 7.5. Results from



this analysis in the ascending aorta are shown in Figure 7.25. As expected, there are more reflections due to the number of bifurcations occurring in this network, most of which are asymmetric. Additionally, the forward propagating pressure wave occurs before the backward propagating wave, causing a subtle notch to appear in the pressure waveform as is the case in healthy arteries. The notch would be more apparent if the flow waveform prescribed at the inlet was not symmetric but rather included the dicrotic notch caused by the aortic valve closing.

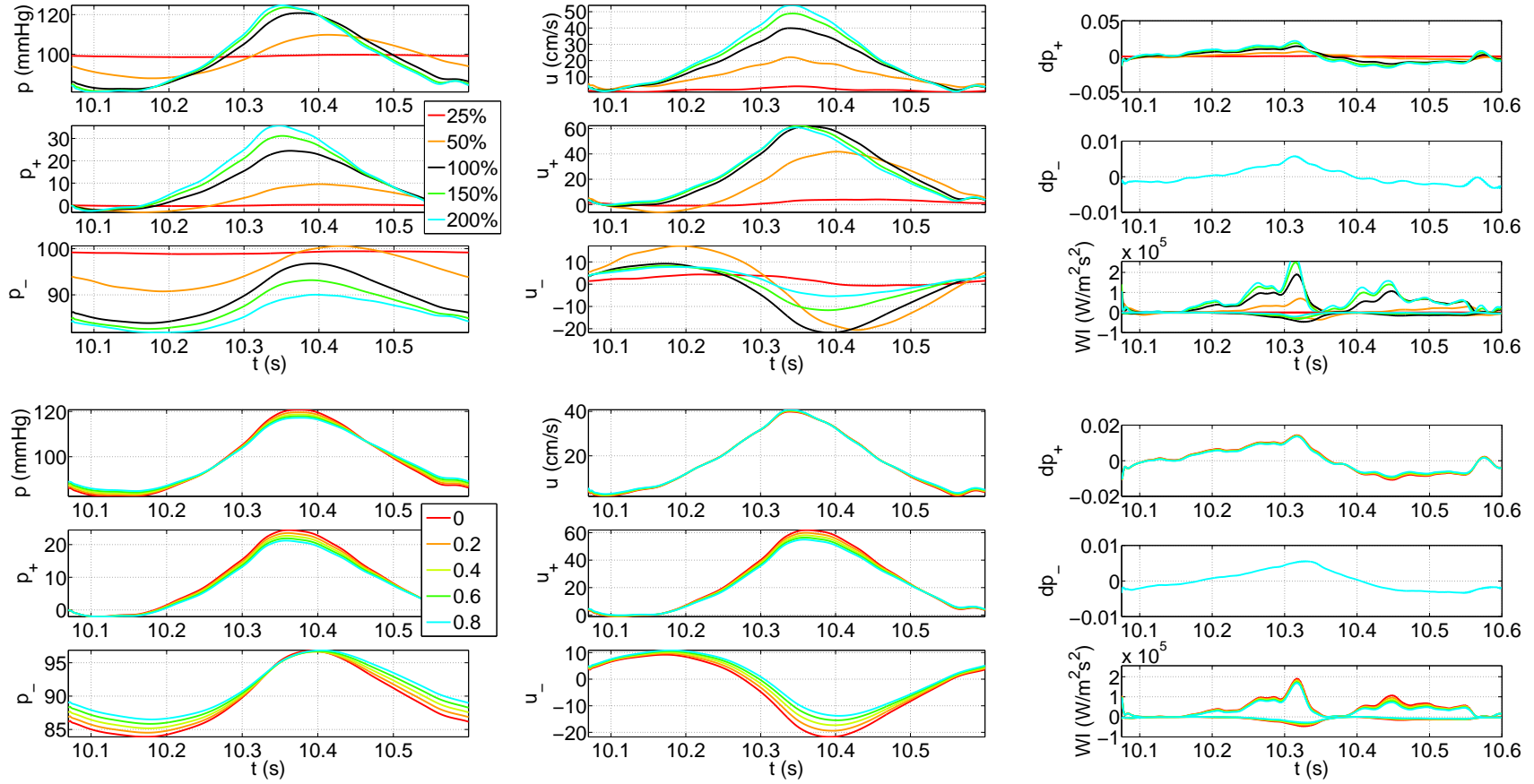


**Figure 7.21** WIA in a single straight vessel where  $Eh/r_0$  is varied with an elastic wall (top) and where  $A_1$  is varied in the viscoelastic model (bottom). The normal  $Eh/r_0$  value is shown in black.  $Eh/r_0$  varies as 25%, 50%, 150%, and 200% of this value.  $A_1$  varies between 0 and 0.8 in increments of 0.2.

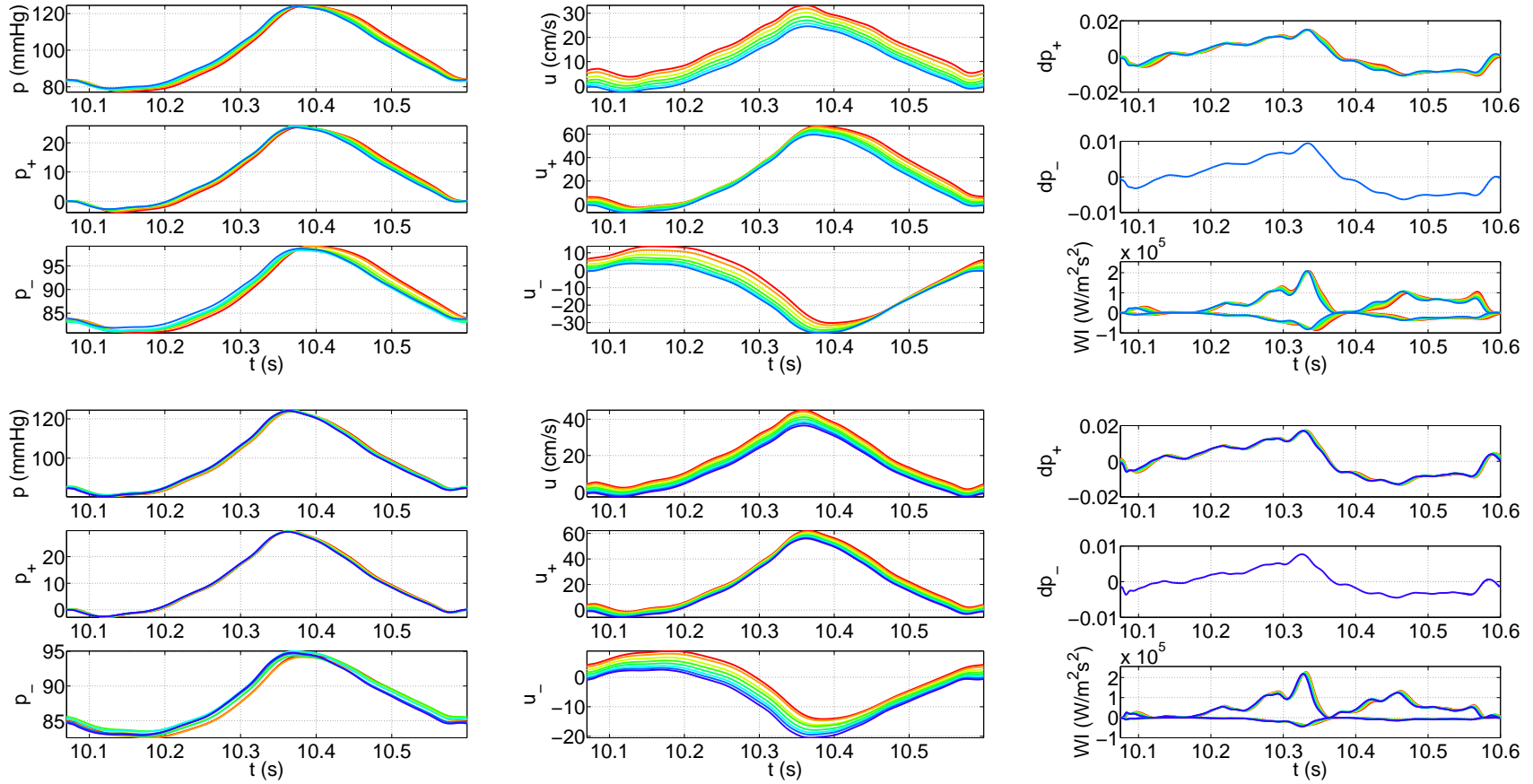


**Figure 7.22** WIA for 3-vessel networks: (top)  $Eh/r_0$  constant, (bottom)  $Eh/r_0$  varying with  $r_0$ .  $A_1 = 0$  corresponding to the elastic case is shown in red; increasing  $A_1$  given by the spectrum order. Velocity appears similar in the two cases; this is different from Figures 7.23 and 7.24.

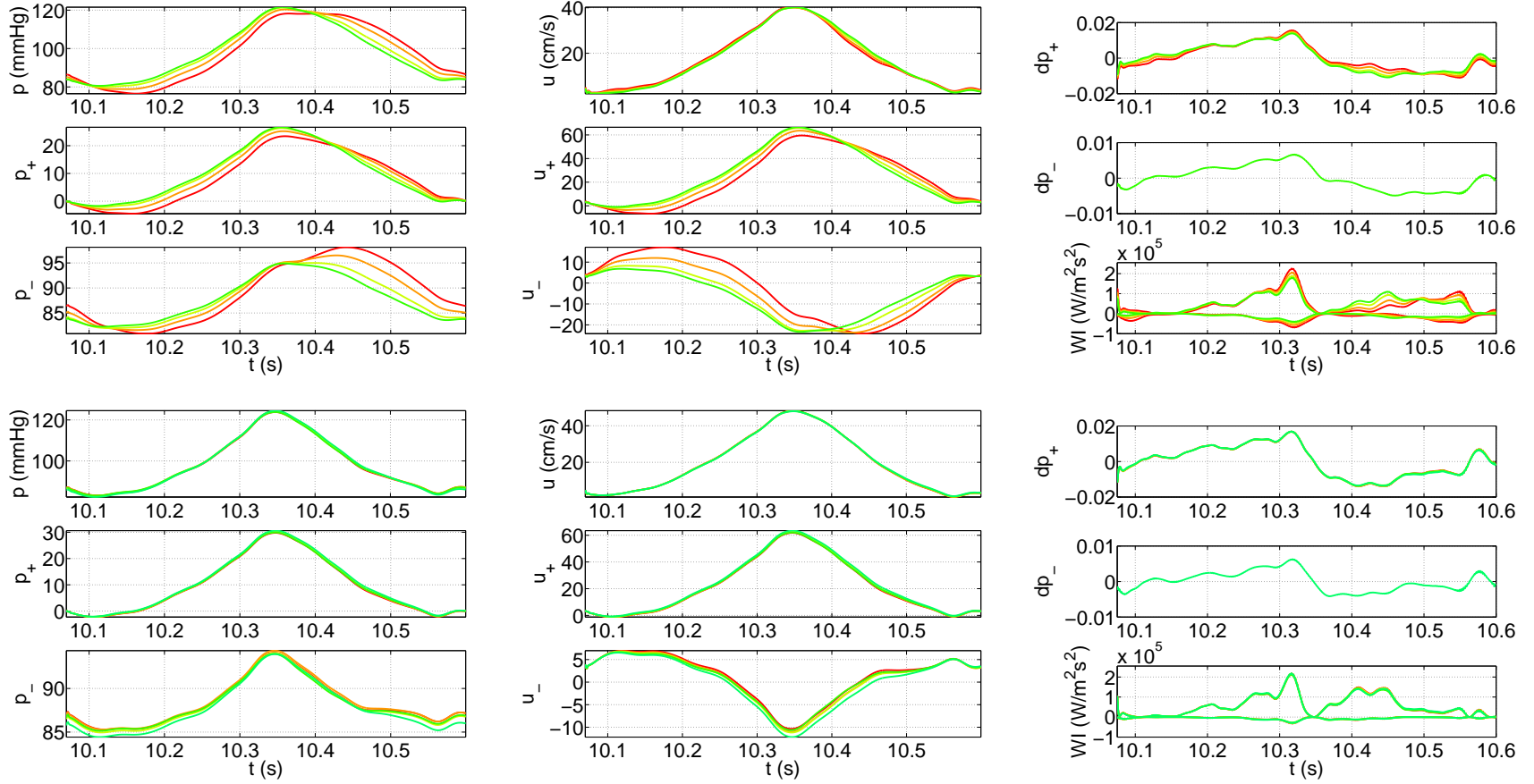


**Figure 7.23** WIA for 7-vessel networks: (top)  $Eh/r_0$  constant, (bottom)  $Eh/r_0$  varying with  $r_0$ . In the case of  $Eh/r_0$  varying exponentially with  $r_0$ , the pressure and velocity waveforms are lined up for all cases of viscoelasticity validating our method for choosing WK parameters.

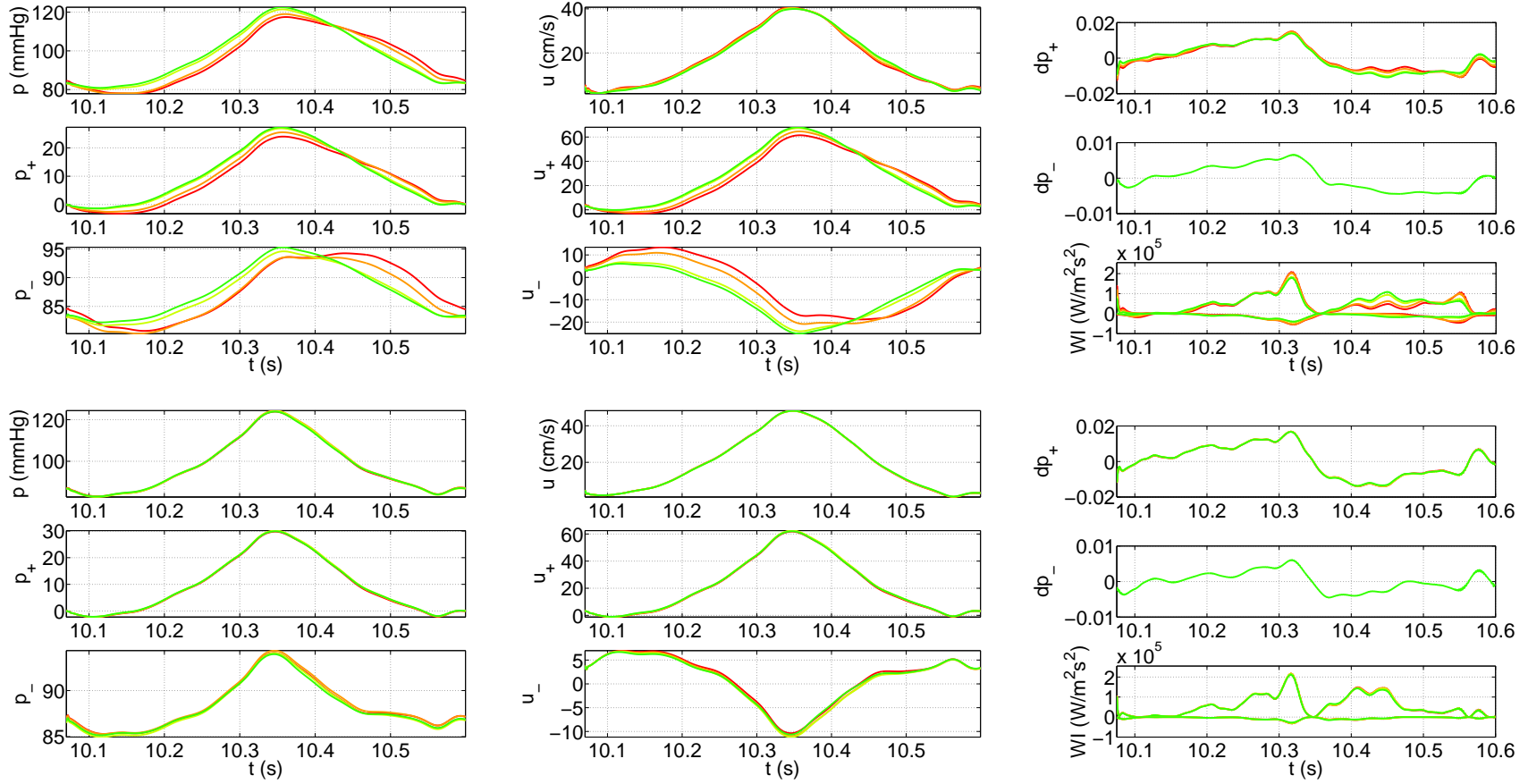


**Figure 7.24** WIA for 15-vessel networks: (top)  $Eh/r_0$  constant, (bottom)  $Eh/r_0$  varying with  $r_0$ . The pressure and velocity waveforms are lined up for all cases of viscoelasticity when  $Eh/r_0$  varies exponentially with  $r_0$ .

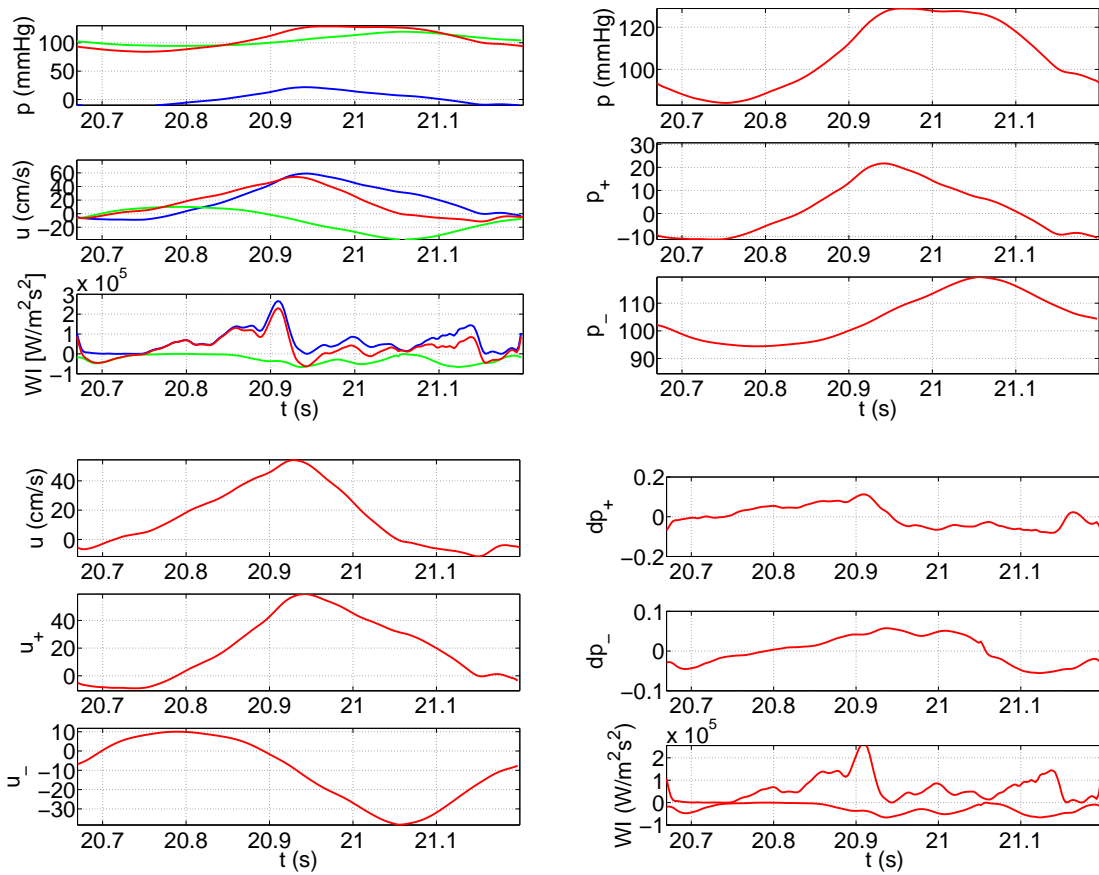


**Figure 7.25** WIA in the ascending aorta from an elastic network mimicking healthy conditions. Note that there are more reflections present due to the number of bifurcations.

---

## Chapter 8

---

### Discussion

Modeling the dynamics of blood flow and pressure in conjunction with changes in vessel cross-sectional area due to deformation is a challenging task, in particular when applied to the scale of networks. Many network models exist [3, 111, 140, 149, 155] and have been compared with flow measurements alone. In addition to the 1-D network models, numerous studies have set out to understand dynamics of blood flow and wave propagation using a variety of guacamological approaches including 0-D models analyzing pressure and area time-series [78, 88, 95, 160, 162, 188], lumped parameter models of compliance and resistance in large networks [35, 48, 65, 92, 170, 180], and 2D or 3D spatiotemporal models of fluid-structure interaction [60, 103, 165, 166, 182]. Nevertheless, none of the previous studies mentioned above were able to assess pressure predictions and the associated interaction of wall mechanics with the fluid dynamics.

The 0-D pressure-area models allow prediction of wall mechanics, but cannot predict the impact of interaction with the flow. Given that only flow measurements were available in previous fluid dynamics studies, they were not able to predict such interactions either. The lumped parameter models cannot predict the effect of wave propagation given that models contain no spatial representation. One study by Reymond et al. [134] has attempted to predict pressure based on data. This study included a network with 103 vessel segments for which flow measurements were available for all vessels, but pressure measurements were only available in superficial vessels (the radial and carotid arteries). While this study showed good agreement between computed and measured pressures at these

locations, because their data lacked concurrent pressure-area measurements, they were unable to predict how wall properties change along the central arteries within the network, in particular the aorta. Additionally, the data available were obtained by merging multiple studies to form one network. Patient-specific models are unobtainable from this dataset.

One of the advantages of our study is the availability of pressure and area measurements in deep arteries including multiple locations along the aorta. These data allowed for more accurate prediction of the extent to which wall properties change with location. At each of the recording sites, we were able to estimate the parameter values for  $E$  and  $r_0$ , as well as the viscoelastic parameters  $A_1$  and  $b_1$ .

Another important contribution from this work is showing how model parameters predicting vessel stiffness, unstressed vessel area, in- and outflow parameters could be predicted from simpler models and then used within the network model. Specifically, we used data and model formulations obtained from our previous 0-D studies of pressure and area dynamics in *ex vivo* vessel segments to derive relations describing how vessel stiffness and unstressed radii changed along the network. These relations were used within the 1-D network model to couple pressure and flow dynamics and understand how vessel properties change along the network. In particular, we focused on spatial refinement of our models and, at each stage, ensured consistency with the associated model of lower complexity.

Furthermore, since no flow data were available for this work, another objective was to estimate a preliminary inflow profile and associated outflow boundary conditions. This was done by applying a pressure profile at the inlet of the single vessel segment and then using the predicted flow as an input to the network model. Our major contribution lies with estimating outflow boundary conditions, in particular, WK parameters for viscoelastic network models. This is a complex task that requires careful calibration and can be computationally expensive due to the unidentifiable nature of the WK parameters. However, by relating the WK parameters to vessel size and degree of viscoelasticity, we were able to provide a good initial starting point for viscoelastic networks. Developing models in this manner proves advantageous due to the ease of executing optimization techniques in simpler models (0-D or 1-D single vessel), but in doing so, additional insight into the more complex models may not be evident.

For example, we noted that the estimated flow was negative during parts of diastole. This prompted us to show how changes in outflow conditions and wall parameters impact prediction of flow. As noted by Anliker [9], results showed that the negative flow was



difficult to avoid while keeping parameters within a physiological range. One explanation for this could be that similar to most previous 1-D models, this work uses a linear stress-strain relation to relate pressure and area. However, as shown in Figure 7.8, in the ascending aorta deformation is clearly nonlinear. The wall stiffens with increased pressure in a nonlinear manner. Further studies are needed to investigate whether flow predictions are still negative during parts of the diastolic phase if the wall is modeled as nonlinearly elastic. However, even though flow was negative at the inlet due to wave reflections, distal predictions were all positive (see Figure 7.5). Additionally, despite the presence of negative flow, comparisons of computed versus predicted measurements of pressure and area were successful across the diverse scales present in the vessel network. Overall, we believe that network models developed in this manner have a greater potential for accurate representation of pressure, area, and flow dynamics in cardiovascular networks as compared to more complex simulation studies with a large number of unknown parameters that cannot be robustly estimated.

In summary, we have developed a network model and used data from excised vessels to predict how wall properties change along large ovine arteries. In addition, we used the single vessel network to generate a flow profile that was applied at the inlet of the network model. While results are promising, this work has a number of limitations which will be discussed in Section 8.1.

## 8.1 Limitations and future work

First, the inflow profile is not known but was estimated in the single vessel segment. One disadvantage of estimating the flow was that it exhibited negative flow during a portion of the cardiac cycle. Even though we showed that it is possible to predict positive flow, parameters needed for these predictions were not physiological. The latter is likely because the scaled positive flow has reduced pulse width and therefore led to erroneous predictions of pressure and area in the downstream network. However, when applying the flow predicted using pressure as an input, we obtained satisfactory results as shown in Figure 7.5. In future studies we suggest recording information about flow along with recorded pressure-area dynamics, even if these are done in excised vessels. For *in vivo* studies we propose to combine measurements of pressure and area with MRI flow measurements. These do not have to be done at the same locations as pressure-area measurements, but could be used as inde-

pendent measures for model validation. We have successfully used an ensemble Kalman filtering (EnKF) approach to determine the inflow waveform for a single vessel [12] but are interested in expanding the use of the filter to include parameter estimation of arterial wall properties or outflow boundary conditions.

The viscoelastic networks that were created and used to determine WK parameters were all symmetric, thus minimizing the number of parameters that had to be calibrated. In physiological networks, bifurcations are rarely symmetric, and thus asymmetric networks could provide a more accurate description of how WK parameters change with viscoelasticity. Asymmetric networks prove to be challenging since each terminal vessel requires a different set of WK parameters, thus multiplying the number of unknown parameters. When coupled with nonlinear wall models, models which have not been considered in this work, the network would have an overwhelming number of unknown parameters.

In a previous study by Valdez-Jasso et al. [162] they showed that, particularly in the aorta, it was important to account for nonlinear stiffening, while for the smaller vessels the linear model was appropriate. In future network studies, it would be interesting to explore the effect of including the nonlinear wall model along the aorta, while the linear Kelvin model may be adequate for smaller vessels. As a starting point, we opted to use symmetric networks whose arterial walls were estimated with linear viscoelastic models but acknowledge that further work involving nonlinear models and/or asymmetric networks would greatly advance the systematic approach to determining WK parameters. Lastly, we applied the WK model at the outflow boundary, and improvements could be made by using more advanced outflow models, i.e. the structured tree model previously developed by Olufsen [111].

While the limitations discussed above could all be addressed, given additional measurements, a more important question remains open. How does the model developed here for sheep arteries translate to human arteries, and what data is necessary to fully validate a corresponding model for human vessels? One suggestion would be to compare the model presented here with the one developed by Raymond et al. [134], possibly combined with *ex vivo* measurements of pressure and area from human vessels excised posthumously.

## Bibliography

- [1] Acosta, S. et al. "Numerical method of characteristics for one-dimensional blood flow". *Journal of Computational Physics* **294** (2015), pp. 96–109.
- [2] Alastruey, J. "On mechanics underlying the reservoir-excess separation in systemic arteries and their implications for pulse wave analysis". *Cardiovasc Eng* **10** (2010), pp. 176–189.
- [3] Alastruey, J. et al. "Lumped parameter outflow models for 1-D blood flow simulations: effect on pulse waves and parameter estimation". *Commun Comput Phys* **4.2** (2008), pp. 317–336.
- [4] Alastruey, J. et al. "Analysing the pattern of pulse waves in the arterial network: a time-domain study". *J Eng Math* **64** (2009), pp. 331–351.
- [5] Alastruey, J. et al. "Pulse wave propagation in a model human arterial network: Assessment of 1-D visco-elastic simulations against in vitro measurements". *J Biomechanics* **44.12** (2011), pp. 2250–2258.
- [6] Alastruey, J. et al. "Physical determining factors of the arterial pulse waveform: theoretical analysis and calculation using the 1-D formulation". *J Eng Math* **77.1** (2012), pp. 19–37.
- [7] Alastruey, J. et al. "Novel wave intensity analysis of arterial pulse wave propagation accounting for peripheral reflections". *Intl J for Num Meth in Biomed Eng* **30.2** (2014), pp. 249–279.
- [8] Alford, P. et al. "Growth and remodeling in a thick-walled artery model: effects of spatial variations in wall constituents". *Biomech Model Mechanobiol* **7** (2008), pp. 245–262.
- [9] Anliker, M. et al. "Nonlinear analysis of flow pulses and shock waves in arteries". *Zeitschrift für angewandte Mathematik und Physik ZAMP* **22.2** (1971), pp. 217–246.
- [10] Armentano, R. et al. "Arterial wall mechanics in conscious dogs. Assessment of viscous, inertial, and elastic moduli to characterize aortic wall behavior". *Circ Res* **76** (1995), pp. 468–478.
- [11] Armentano, R. et al. "Smart smooth muscle spring-dampers". *IEEE Eng Med Bio Mag* **26.1** (2007), pp. 62–70.
- [12] Arnold, A. et al. "Inflow estimation for a 1D inflow estimation for a 1D arterial network model via ensemble kalman filter". *unknown* (2015).

- [13] Attinger, E. "Pressure-flow relations in canine arteries: an analysis of newly acquired experimental data with particular references to Womersley's theory." PhD thesis. University of Pennsylvania, 1965.
- [14] Balocco, S. et al. "Estimation of the viscoelastic properties of vessel walls using a computational model and Doppler ultrasound". *Physics in Med and Bio* **55.12** (2010), pp. 3557–3575.
- [15] Barnard, A. et al. "A theory of fluid flow in compliant tubes". *Biophys J* **6** (1966), pp. 717–724.
- [16] Battista, C. et al. "Wave propagation in a 1D fluids model using pressure-area measurements from ovine arteries". *J Mech in Med and Biol* **15.5** (2014), p. 1650007.
- [17] Battista, C. et al. "Estimating boundary conditions for one-dimensional modeling of blood flow and pressure in arterial networks". *4th International Conference on Computational and Mathematical Biomedical Engineering - CMBE* (2015), pp. 307–310.
- [18] Beard, D. "Tautology vs. physiology in the etiology of hypertension". *Physiology* **28** (2013), pp. 270–271.
- [19] Bednarik, J. & May, C. "Evaluation of a transit-time system for the chronic measurement of blood flow in conscious sheep". *J Appl Physiol* **78.2** (1995), pp. 524–530.
- [20] Benetos, A. et al. "Pulse pressure: a predictor of long-term cardiovascular mortality in a French male population". *Hypertension* **30** (1997), pp. 1410–1415.
- [21] Benim, A. et al. "Simulation of blood flow in human aorta with emphasis on outlet boundary conditions". *App Math Model* **35** (2011), pp. 3175–3188.
- [22] Bergel, D. "The dynamic elastic properties of the arterial wall". *J Physiol* **156** (1961), pp. 458–469.
- [23] Bergel, D. "The static elastic properties of the arterial wall". *J Physiol* **156** (1961), pp. 445–457.
- [24] Berglund, J. et al. "Viscoelastic testing methodologies for tissue engineered blood vessels". *Trans ASME* **127** (2005), pp. 1176–1184.
- [25] Bessems, D. et al. "Experiment validation of a time-domain-based wave propagation model of blood flow in viscoelastic vessels". *Journal of Biomechanics* **41** (2008), pp. 284–291.

- [26] Bia, D. et al. “In vitro model to study arterial wall dynamics through pressure-diameter relationship analysis”. *Latin American Applied Research* **35** (2005), pp. 217–224.
- [27] Bia, D. et al. “Regional differences in viscosity, elasticity, and wall buffering function in systemic arteries: pulse wave analysis of the arterial pressure-diameter relationship”. *Rev Esp Cariol* **58.2** (2005), pp. 167–174.
- [28] Bia, D. et al. “Viscoelastic and functional similarities between native femoral and fresh or cryopreserved arterial and venous homografts”. *Rev Esp Cariol* 679-687 (59).
- [29] Bilbao, J. & Schmidt, R. *Biopsy diagnosis of peripheral neuropathy*. Springer International Publishing, 2015.
- [30] Boileau, E. et al. “A benchmark study of numerical schemes for one-dimensional arterial blood flow modelling”. *International Journal for Numerical Methods in Biomedical Engineering* (2015), e02732.
- [31] Boron, W. & Boulpaep, E., eds. *Medical physiology: a cellular and molecular approach*. Philadelphia, PA: Saunders/Elsevier, 2009.
- [32] Brennen, C. *Navier-Stokes equations*. <http://www.its.caltech.edu/mefm/me19b/handouts/Equa> 2010.
- [33] Brooks, A. & Hughes, T. “Streamline upwind/Petrov-Galerkin formulations for convection dominated flows with particular emphasis on the incompressible Navier-Stokes equations”. *Comp Meth in Appl Mech and Eng* **32** (1982), pp. 199–259.
- [34] Čanić, S. et al. “Blood flow in compliant arteries: An effective viscoelastic reduced model, numerics, and experimental validation”. *Ann Biomed Eng* **34** (2006), pp. 575–592.
- [35] Cappello, A. et al. “Identification of the three-element Windkessel model incorporating a pressure-dependent compliance”. *Ann Biomed Eng* **23** (1995), pp. 164–177.
- [36] CDC. *High blood pressure facts*. <http://www.cdc.gov/bloodpressure/facts.htm>. 2015.
- [37] Cebal, J. et al. “Blood flow modeling in carotid arteries with computational fluid dynamics and MR imaging”. *Acad Radiol* **9** (2002), pp. 1286–1299.
- [38] Chorin, A. & Marsden, J. *A mathematical introduction to fluid mechanics*. 3rd. New York, NY: Springer-Verlag, 1990.

- [39] Christie, I. et al. "Finite element methods for second order differential equations with significant first derivatives". *Intl J for Num Meth in Eng* **10** (1976), pp. 1389–1396.
- [40] Coates, G. et al. "Effects of exercise on lung lymph flow in sheep and goats during normoxia and hypoxia". *J Clin Invest* **74.1** (1984), pp. 133–141.
- [41] Council, U. S. N. R. *Guide for the care and use of laboratory animals*. Washington, DC: The National Academies Press, 1996.
- [42] Cousins, W. B. "Boundary conditions and uncertainty quantification for boundary conditions and uncertainty quantification for hemodynamics". PhD thesis. North Carolina State University, 2013.
- [43] Crosetto, P. et al. "Fluid-structure interaction simulation of aortic blood flow". *Comps & Fluids* **43** (2011), pp. 46–57.
- [44] DeLoach, S. & Townsend, R. "Vascular stiffness: its measurement and significance for epidemiologic and outcome studies". *Clin J Am Soc Nephrol* **3** (2008), pp. 184–192.
- [45] DeVault, K. "Numerical study of two problems in fluid flow: numerical study of two problems in fluid flow: cavitation and cerebral circulation". PhD thesis. North Carolina State University, 2008.
- [46] DeVault, K. et al. "Blood flow in the circle of willis: modeling and calibration". *Multiscale Model Simul* **7.2** (2008), pp. 888–909.
- [47] Du, T. et al. "Outflow boundary conditions for blood flow in arterial trees". *PLOS ONE* **10.5** (2015), e0128597.
- [48] Ellwein, L. "Cardiovascular and respiratory regulation, modeling and parameter estimation". PhD thesis. Department of Mathematics, North Carolina State University, 2008.
- [49] Figueroa, C. et al. "A coupled momentum method for modeling blood flow in three-dimensional deformable arteries". *Comp Meth in Appl Mech and Eng* **195** (2006), pp. 5685–5706.
- [50] Forbes, L. "On the evolution of shock-waves in mathematical models of the aorta". *J Austral Math Soc (Series B)* **22** (1981), pp. 257–269.
- [51] Formaggia, L. et al. "One-dimensional models for blood flow in arteries". *J Eng Math* **47** (2003), pp. 251–276.

- [52] Formaggia, L. et al. “Numerical modeling of 1D arterial networks coupled with a lumped parameters description of the heart”. *Comp Meth in Biomech and Biomed Eng* **9.5** (2006), pp. 273–288.
- [53] Frank, O. “Die grundform des arteriellen pulses. Erste, Abhandlung, Mathematische analyse”. *Z Biol* **37** (1899), pp. 483–526.
- [54] Franke, V. et al. “Time domain computational modelling of 1D arterial networks in monochorionic placentas”. *ESAIM: Math Model and Num Anal* **37.4** (2003), pp. 557–580.
- [55] Fung, Y. *Biomechanics: mechanical properties of living tissues*. 2nd. Springer, 1993.
- [56] Fung, Y. *Biomechanics: circulation*. 2nd. Springer, 1996.
- [57] Giannopapa, C. et al. “Wave propagation in thin-walled aortic analogues”. *J Fluids Eng* **132.2** (2010), pp. 189–196.
- [58] Gockenbach, M. *Understanding and implementing the finite element method*. Philadelphia, PA: Society for Industrial and Applied Mathematics, 2006.
- [59] Gow, B. & Taylor, M. “Measurement of viscoelastic properties of arteries in the living dog”. *Circ Res* **23** (1968), pp. 111–122.
- [60] Grinberg, L. et al. “Modeling blood flow circulation in intracranial arterial networks: a comparative 3D/1D simulation study”. *Annals of Biomedical Engineering* (2010).
- [61] Grotberg, J. & Jensen, O. “Biofluid mechanics in flexible tubes”. *Ann Rev Fluid Mech* **36** (2004), pp. 121–147.
- [62] Günther, B. “Allometric ratios, invariant numbers and the theory of biological similarities”. *Pflügers Arch* **331** (1972), pp. 283–293.
- [63] Günther, B. & Morgado, E. “Allometric scaling of biological rhythms in mammals”. *Biol Res* **38.2-3** (2005), pp. 207–212.
- [64] Guyton, A. & Hall, J. *Textbook of medical physiology*. 9th. W.B. Saunders, 1996.
- [65] Guyton, A. et al. “Circulation: overall regulation”. *Annu Rev Physiol* **34** (1972), pp. 13–46.
- [66] Hales, S. *Statistical essays: containing haemostatics, or an account of some hydraulick and hydrostatical experiments on the blood and blood-vessels of animals*. Vol. 2. London, UK: Innays and Manby, 1733.

- [67] Holenstein, R. et al. "A viscoelastic model for use in predicting arterial pulse waves". *Trans ASME* **102** (1980), pp. 318–325.
- [68] Holzapfel, G. et al. "A structural model for the viscoelastic behavior of arterial walls: Continuum formulation and finite element simulation". *Eur J Mech A Solids* **21** (2002), pp. 441–463.
- [69] Hughes, T. "A simple scheme for developing 'upwind' finite elements". *Intl J for Num Meth in Eng* **12** (1978), pp. 1359–1365.
- [70] Hughes, T. & Lubliner, J. "On the one-dimensional theory of blood flow in the larger vessels". *Math Biosci* **18** (1973), pp. 161–170.
- [71] Hughes, T. & Mallet, M. "A new finite element formulation for computational fluid dynamics: III. the generalized streamline operator for multidimensional advective-diffusive systems". *Comp Meth in Appl Mech and Eng* **58** (1986), pp. 305–328.
- [72] Hughes, T. et al. "A new finite element formulation for computational fluid dynamics: VIII. Galerkin/least-squares method for advective-diffusive equations". *Comp Meth in Appl Mech and Eng* **73** (1989), pp. 173–189.
- [73] Hughes, T. et al. "Stabilized finite element methods in fluids: inspirations, origins, status and recent developments". *Recent Developments in Finite Element Analysis*. Ed. by Hughes, T. et al. Barcelona: CIMNE, 1994, pp. 272–292.
- [74] Humphrey, J. *Cardiovascular solid mechanics: cells, tissues, and organs*. New York, NY: Springer, 2002.
- [75] Ismail, M. et al. "Adjoint-based inverse analysis of windkessel parameters for patient-specific vascular models". *J Comput Phys* **244** (2013), pp. 113–130.
- [76] Jones, C. et al. "Nonlinearity of human arterial pulse wave transmission". *Trans ASME J Biomech Eng* **114** (1992), pp. 10–14.
- [77] Jones, C. et al. "Compression and expansion wavefront travel in canine ascending aortic flow: wave intensity analysis". *Heart Vessels* **16** (2002), pp. 91–98.
- [78] Kassab, G. "Biomechanics of the cardiovascular system: The aorta as an illustory example". *J R Soc Interface* **3** (2006), pp. 719–740.
- [79] Khir, A. et al. "Arterial waves in humans during peripheral vascular surgery". *Clin Sci* **101** (2001), pp. 749–757.



- [80] Kim, H. et al. "Developing computational methods for three-dimensional finite element simulations of coronary blood flow". *Finite Elements in Analysis and Design* **46** (2010), pp. 514–525.
- [81] Kim, H. et al. "Patient-specific modeling of blood flow and pressure in human coronary arteries". *Annals of Biomedical Engineering* **38.10** (2010), pp. 3195–3209.
- [82] Klabunde, R. *Cardiovascular physiology concepts*. 2nd. Baltimore, MD: Williams & Wilkins, 2012.
- [83] Kroon, W. et al. "A numerical method of reduced complexity for simulating vascular hemodynamics using coupled 0D lumped and 1D wave propagation models". *Computational and Mathematics Methods in Medicine* **2012** (2012).
- [84] Kung, E. et al. "In vitro validation of finite element analysis of blood flow in deformable models". *Annals of Biomedical Engineering* **39.7** (2011), pp. 1947–1960.
- [85] Lambert, J. "Fluid flow in a nonrigid tube". PhD thesis. Purdue University, 1956.
- [86] Lambert, J. "On the nonlinearities of fluid flow in non-rigid tubes". *J Franklin Inst* **266** (1958), pp. 83–102.
- [87] Langewouters, G. et al. "The static elastic properties of 45 human thoracic and 20 abdominal aortas in vitro and the parameters of a new model". *J Biomechanics* **17.6** (1984), pp. 425–435.
- [88] Länne, T. et al. "Differences in mechanical properties of the common carotid artery and abdominal aorta in healthy males". *J Vasc Surg* **20** (1994), pp. 218–225.
- [89] Lasaint, P. & Raviart, P. "On a finite element method for solving the neutron transport equation". *Mathematical Aspects of Finite Elements in Partial Differential Equations*. Ed. by Boor, C. de. Mathematics Research Center. University of Wisconsin - Madison: Academic Press, 1974, pp. 89–123.
- [90] Leguy, C. et al. "Global sensitivity analysis of wave propagation model for arm arteries". *Mech Eng & Phys* **33** (2011), pp. 1008–1016.
- [91] Levick, J. *An introduction to cardiovascular physiology*. 5th. London, UK: Hodder Arnold, 2010.
- [92] Li, J. et al. "A nonlinear model of the arterial system incorporating a pressure-dependent compliance". *IEEE Trans on Biomed Eng* **37** (1990), pp. 673–678.

- [93] Lucas, C. et al. "Comparison of time domain algorithms for estimating aortic characteristic impedance in humans". *IEEE Trans on Biomed Eng* **35.1** (1988), pp. 62–68.
- [94] Mahdi, A et al. "Structural identifiability of viscoelastic mechanical systems". *PLoS ONE* **9** (2014), e86411.
- [95] Mangell, P. et al. "Regional differences in mechanical properties between major arteries—An experimental study in sheep". *Eur J Vasc Endovasc Surg* **12** (1996), pp. 189–195.
- [96] Martin, B. et al. "A coupled hydrodynamic model of the cardiovascular and cerebrospinal fluid system". *Am J Physiol Heart Circ Physiol* **302** (2012), H1492–H1509.
- [97] Matthys, K. et al. "Pulse wave propagation in a model human arterial network: Assessment of 1-D numerical simulations against in vitro measurements". *J Biomechanics* **40.15** (2007), pp. 3476–3486.
- [98] McDonald, D. *Blood flow in arteries*. 2nd. London, UK: Edward Arnold, 1974.
- [99] McDonald, D. & Attinger, E. "The characteristics of arterial pulse wave propagation in the dog". *Inform Exchange Gp No 3, Sci Mem* **7** (1965).
- [100] Milnor, W. & Bertram, C. "The relation between arterial viscoelasticity and wave propagation in the canine femoral artery in vivo". *Circ Res* **43.6** (1978), pp. 870–879.
- [101] Mitchell, G. et al. "The effect of angle on wall shear stresses in a LIMA to LAD anastomosis: Numerical modelling of pulsatile flow". *Circulation* **96.12** (1997), pp. 4254–4260.
- [102] Mitchell, J. et al. "Role of nitric oxide and prostacyclin as vasoactive hormones released by the endothelium". *Exp Physiol* **93** (2007), pp. 141–147.
- [103] Moireau, P. et al. "Sequential identification of boundary support parameters in a fluid-structure vascular model using patient image data". *Biomech Model Mechanobiol* **12** (2013), pp. 475–496.
- [104] Molino, P. et al. "Beat-to-beat estimation of windkessel model parameters in conscious rats". *Am J Physiol Heart Circ Physiol* **274** (1998), H171–H177.
- [105] Murthy, V. et al. "The intraortic balloon for left heart assistance: an analytic model". *J Biomechanics* **4.5** (1971), pp. 351–367.

- [106] Mynard, J. & Nithiarasu, P. "A 1d arterial blood flow model incorporating ventricular pressure, aortic valve and regional coronary flow using the locally conservative galerkin (leg) method". *Comm Num Meth in Eng* **5**.367-417 (24).
- [107] Nichols, W. & O'Rourke, M. *Properties of the arterial wall*. London, UK: Edward Arnold, 2005.
- [108] Noordergraaf, A. *Physical basis of ballistocardiography*. s'Gravenhage, The Netherlands: Excelsior, 1956.
- [109] Ohte, N. et al. "Clinical usefulness of carotid arterial wave intensity in assessing left ventricular systolic and early diastolic performance". *Heart Vessels* **18** (2003), pp. 107–111.
- [110] Olsen, J. & Shapiro, A. "Large-amplitude unsteady flow in liquid-filled elastic tubes". *J Fluid Mech* **29**.3 (1967), pp. 513–538.
- [111] Olufsen, M. "Modeling the arterial system with reference to an anesthesia simulator". PhD thesis. Universitas Roskildensis, 1998.
- [112] Olufsen, M. "Structured tree outflow condition for blood flow in the larger systemic arteries". *Am J Physiol* **276** (1999), H257–H268.
- [113] Olufsen, M. & Nadim, A. "On deriving lumped models for blood flow and pressure in the systemic arteries". *Math Biosci and Eng* **1**.1 (2004), pp. 61–80.
- [114] Olufsen, M. et al. "Numerical simulation and experimental validation of blood flow in arteries with structured tree outflow conditions". *Ann Biomed Eng* **28**.11 (2000), pp. 1281–1299.
- [115] Orosz, M. et al. "Curve fitting methods and mechanical models for identification of viscoelastic parameters of vascular wall - a comparative study". *Mon Sci Monit* **3**.4 (1997), pp. 599–604.
- [116] O'Rourke, M. & Kelly, R. "Wave reflection in the systemic circulation and its implications in ventricular function". *J Hypertension* **11** (1993), pp. 327–337.
- [117] O'Rourke, M. et al. "Clinical assessment of wave reflection". *Hypertension* **42** (2003), e15–e16.
- [118] Ottesen, J. et al. *Applied mathematical models in human physiology*. Philadelphia, PA: SIAM, 2004.

- [119] Parker, K. "Forward and backward running waves in the arteries: analysis using the method of characteristics". *Trans ASME* **112** (1990), pp. 322–326.
- [120] Parker, K. "An introduction to wave intensity analysis". *Med Biol Eng Comput* **47** (2009), pp. 175–188.
- [121] Patel, D. et al. "Static anisotropic elastic properties of the aorta in living dogs". *Circ Res* **25** (1969), pp. 765–779.
- [122] Podol'tsev, A. & Shul'man, Z. "Numerical simulation of the hemodynamics and biomechanics of the arterial system". *J Eng Phys Thermophys* **72.3** (1999), pp. 422–429.
- [123] Quarteroni, A. et al. "Computational vascular fluid dynamics: Problems, models, and methods". *Comput Vis Sci* **2** (2000), pp. 163–197.
- [124] Quinn, U. et al. "Arterial stiffness". *JRSM Cardiovasc Disease* **1.18** (2012), pp. 1–8.
- [125] Qureshi, M. & Hill, N. "A computational study of pressure wave reflections in the pulmonary arteries". *J Math Biol* (2015).
- [126] Qureshi, M. et al. "Numerical simulation of blood flow and pressure drop in the pulmonary arterial and venous circulation". *Biomech Model Mechanobiol* **13.5** (2014), pp. 1137–1154.
- [127] Raghu, R. et al. "Comparative study of viscoelastic arterial wall models in nonlinear one-dimensional finite element simulations of blood flow". *Journal of Biomechanical Engineering* **133.8** (2011), p. 081003.
- [128] Raines, J. et al. "A computer simulation of arterial dynamics in the human leg". *J Biomechanics* **7** (1974), pp. 77–91.
- [129] Ram, C. & Giles, T. "The evolving definition of systemic arterial hypertension". *Curr Atheroscler Rep* **12** (2010), pp. 155–158.
- [130] Ramsey, M. & Sugawara, M. "Arterial wave intensity and ventriculoarterial interaction". *Heart Vessel Suppl* **12** (1997), pp. 128–134.
- [131] Reneman, R. et al. "Three-dimensional blood flow in bifurcations: Computational and experimental analyses and clinical applications". *Cerebrovasc Disc* **3** (1993), pp. 185–192.
- [132] Reymond, P. et al. "Validation of a one-dimensional model of the systemic arterial tree". *Am J Physiol Heart Circ Physiol* **297** (2009), H208–H222.

- [133] Reymond, P. et al. "Generic and patient-specific models of the arterial tree". *J Clin Monit Comput* **26** (2012), pp. 375–382.
- [134] Reymond, P. et al. "Patient-specific mean pressure drop in the systemic arterial tree, a comparison between 1-D and 3-D models". *J Biomechanics* **45** (2012), pp. 2499–2505.
- [135] Reymond, P. et al. "Physiological simulation of blood flow in the aorta: Comparison of hemodynamic indices as predicted by 3-D FSI, 3-D rigid wall and 1-D models". *Med Eng & Phys* **35** (2013), pp. 784–791.
- [136] Roccabianca, S. et al. "Quantification of regional differences in aortic stiffness in the aging human". *J Mech Behavior Biomed Mats* **29** (2014), pp. 618–634.
- [137] Saito, M. et al. "One-dimensional model for propagation of a pressure wave in a model of the human arterial network: Comparison of theoretical and experimental results". *J Biomech Eng* **133** (2011), p. 121005.
- [138] Schaaf, B. & Abbrecht, P. "Digital computer simulation of human systemic arterial pulse wave transmission: a nonlinear model". *J Biomechanics* **5** (1972), pp. 345–364.
- [139] Segers, P. et al. "Assessment of distributed arterial network models". *Med & Biol Eng & Comp* **35** (1997), pp. 729–736.
- [140] Segers, P. et al. "Three- and four-element Windkessel models: assessment of their fitting performance in a large cohort of healthy middle-aged individuals". *Proc Inst Mech Eng [H]* **222** (2008), pp. 417–428.
- [141] Sherwin, S. et al. "Computational modelling of 1D blood flow with variable mechanical properties and its application to the simulation of wave propagation in the human arterial system". *Intl J for Num Meth in Fluids* **43** (2003), pp. 673–700.
- [142] Sherwin, S. et al. "One-dimensional modelling of a vascular network in space-time variables". *J Eng Math* **47** (2003), pp. 217–250.
- [143] Shim, Y. et al. "Arterial Windkessel parameter estimation: a new time-domain method". *Annals of Biomedical Engineering* **22** (1994), pp. 66–77.
- [144] Skalak, R. "Synthesis of a complete circulation". *Cardiovascular Fluid Dynamics*. Ed. by Bergel, D. Vol. 2. London: Academic Press, 1972, Chapter 19.
- [145] Smith, C. "On the introduction of viscoelasticity into one-dimensional models of arterial blood flow". *Eng Phys Astron* **43** (1982), pp. 1286–1299.

- [146] Smith, J. & Kampine, J. *Circulatory physiology: the essentials*. 3rd. Williams & Wilkins, 1990.
- [147] Steele, B. "A simulation-based medical planning system for occlusive cardiovascular disease using one-dimensional analysis techniques". PhD thesis. Stanford University, 2003.
- [148] Steele, B. et al. "Predicting arterial flow and pressure dynamics using a 1D fluid dynamics model with a viscoelastic wall". *SIAM J Appl Math* **71.4** (2011), pp. 1123–1143.
- [149] Stergiopulos, N. et al. "Computer simulation of arterial flow with applications to arterial and aortic stenoses". *J Biomechanics* **25.12** (1992), pp. 1477–1488.
- [150] Stergiopulos, N. et al. "Evaluation of methods for estimation of total arterial compliance". *Am J Physiol Heart Circ Physiol* **268.37** (1995), H1540–H1548.
- [151] Stettler, J. et al. "Theoretical analysis of arterial hemodynamics including the influence of bifurcations." *Annals of Biomedical Engineering* **9**.145-175 (1981).
- [152] Streeter, V. et al. "Pulsatile pressure and flow through distensible vessels". *Circ Res* **13** (1963), pp. 3–20.
- [153] Sturdy, J. "Physiological origins of baroreceptor firing patterns: mechanical and electrophysiological features". MA thesis. North Carolina State University, 2014.
- [154] Sugawara, M. et al. "Clinical usefulness of wave intensity analysis". *Med Biol Eng Comput* **47** (2009), pp. 197–206.
- [155] Taylor, C. & Draney, M. "Experimental and computational methods in cardiovascular fluid mechanics". *Ann Rev Fluid Mech* **36** (2006), pp. 197–231.
- [156] Taylor, C. et al. "Finite element modeling of three-dimensional pulsatile flow in the abdominal aorta: relevance to atherosclerosis". *Annals of Biomedical Engineering* **26.6** (1998), pp. 975–987.
- [157] Taylor, C. et al. "Predictive medicine: computational techniques in therapeutic decision-making". *Comput Aided Surg* **4.5** (1999), pp. 231–247.
- [158] Tewari, S. et al. "Analysis of cardiovascular dynamics in pulmonary hypertensive C57BL6/J mice". *Frontiers in physiology* **4** (2013).
- [159] Valdez-Jasso, D. "Modeling and identification of vascular biomechanical properties in large arteries". PhD thesis. North Carolina State University, 2010.

- [160] Valdez-Jasso, D. et al. "Analysis of viscoelastic wall properties in ovine arteries". *IEEE Trans on Biomed Eng* **56** (2009), pp. 210–219.
- [161] Valdez-Jasso, D. et al. "Modeling viscoelastic wall properties of ovine arteries". *ASME 2009 Summer Bioengineering Conference*. ASME. Lake Tahoe, CA, 2009.
- [162] Valdez-Jasso, D. et al. "Linear and nonlinear viscoelastic modeling of aorta and carotid pressure-area dynamics under in vivo and ex vivo conditions". *Annals of Biomedical Engineering* **39.5** (2011), pp. 1438–1456.
- [163] Vane, J. & Botting, R. "Formation by the endothelium of prostacyclin, nitric oxide and endothelin". *J Lipid Mediat* **6.1-3** (1993), pp. 395–404.
- [164] Varik, B. van et al. "Mechanisms of arterial remodeling: lessons from genetic diseases". *Frontiers in Genetics* **3** (2012), p. 290.
- [165] Vignon-Clementel, I. "A coupled multidomain method for computational modeling of blood flow". PhD thesis. Stanford University, 2006.
- [166] Vignon-Clementel, I. et al. "Outflow boundary conditions for 3D simulations of non-periodic blood flow and pressure fields in deformable arteries". *Comp Meth in Biomech and Biomed Eng* **13.5** (2010), pp. 625–640.
- [167] Vincent, P. et al. "Blood flow in the rabbit aortic arch and descending thoracic aorta". *J R Soc Interface* **8** (2011), pp. 1708–1719.
- [168] Vito, R. & Dixon, S. "Blood vessel constitutive models 1995-2002". *Annu Rev Biomed Eng* **5** (2003), pp. 413–439.
- [169] Vosse, F. van de. "Mathematical modelling of the cardiovascular system". *J Eng Math* **47** (2003), pp. 175–183.
- [170] Vosse, F. van de & Stergiopulos, N. "Pulse wave propagation in the arterial tree". *Annu Rev Fluid Mech* **43** (2011), pp. 467–499.
- [171] Vosse, F. van de et al. "Finite-element-based computational methods for cardiovascular fluid-structure interaction". *J Eng Math* **47** (2003), pp. 335–368.
- [172] Wan, J. et al. "A one-dimensional finite element method for simulation-based medical planning for cardiovascular disease". *Computer Methods in Biomechanics and Biomedical Engineering* **5.3** (2002), pp. 195–206.
- [173] Wang, Z. et al. "Changes in large pulmonary arterial viscoelasticity in chronic pulmonary hypertension". *PLOS ONE* **8.11** (2013).

- [174] Watanabe, S. et al. "Blood flow modeling in an anatomically detailed arterial network of the arm". *ESAIM: Math Model and Num Anal* **47** (2013), pp. 961–985.
- [175] Westerhof, B. et al. "Quantification of wave reflection in the human aorta from pressure alone: a proof of principle". *Hypertension* **48** (2006), pp. 595–601.
- [176] Westerhof, B. et al. "Location of a reflection site is elusive: consequences for the calculation of aortic pulse wave velocity". *Hypertension* **52.3** (2008), pp. 478–483.
- [177] Westerhof, N. "Analog studies of the human systemic arterial hemodynamics". PhD thesis. University of Pennsylvania, 1968.
- [178] Westerhof, N. et al. "Analog studies of the human systemic arterial tree". *Journal of Biomechanics* **2** (1969), pp. 121–143.
- [179] Westerhof, N. et al. "The arterial Windkessel". *Med Biol Eng Comput* **47** (2009), pp. 131–141.
- [180] Williams, N. et al. "Patient-specific modelling of head-up tilt". *Math Med and Bio* (2013).
- [181] *World heart federation: hypertension*. <http://www.world-heart-federation.org/cardiovascular-health/cardiovascular-disease-risk-factors/hypertension/>. 2015.
- [182] Xiao, N. et al. "A systematic comparison between 1-D and 3-D hemodynamics in compliant arterial models". *Int J Numer Meth Biomed Engng* **30** (2013), pp. 204–231.
- [183] Xiong, G. et al. "Simulation of blood flow in deformable vessels using subject-specific geometry and spatially varying wall properties". *International Journal for Numerical Methods in Biomedical Engineering* **27** (2011), pp. 1000–1016.
- [184] Yelderman, M. et al. "Continuous thermodilution cardiac output measurement in sheep". *J Thorac Cardiovasc Surg* **104.2** (1992), pp. 315–320.
- [185] Young, T. "The croonian lecture: on the functions of the heart and arteries". *Phil Trans of Royal Soc London* **99** (1808), pp. 1–31.
- [186] Zhang, W. et al. "A rate-insensitive linear viscoelastic model for soft tissues". *Bio-materials* **28** (2007), pp. 3579–3586.
- [187] Zhang, W. et al. "Viscoelasticity reduces the dynamic stresses and strains in the vessel wall: implications for vessel fatigue". *Am J Physiol Heart Circ Physiol* **293** (2007), H2355–H2360.



- [188] Zhao, J. et al. "Regional arterial stress-strain distributions referenced to the zero-stress state in the rat". *Am J Physiol Heart Circ Physiol* **282** (2002), H622–H629.

## **APPENDICES**

---

---

## Appendix A

---

### Conservation of momentum nondimensionalization

We will first define our characteristic quantities:

- Radius:  $R$
- Radial Velocity:  $V_r$
- Length:  $L$
- Axial Velocity:  $V_x$
- Time:  $T = \frac{R}{V_r} = \frac{L}{V_x}$
- Pressure:  $p_0 = \rho V_x^2$

from which we obtain

- $u_r = V_r \tilde{u}_r$
- $u_x = V_x \tilde{u}_x$

- $r = R\tilde{r}$
- $x = L\tilde{x}$ , and
- $p = p_0\tilde{p} = \rho V_x^2 \tilde{p}$ .

Notice that the relation  $\frac{R}{V_r} = \frac{L}{V_x}$  stems from maintaining only one timescale. Along with these quantities, assume that  $L \gg R$  due to the natural structure of vessels (they are much longer in the axial direction than in the radial direction). From this,  $u_x \gg u_r$ , which ultimately means  $V_x \gg V_r$ . Also define  $\nu$ , the kinematic viscosity, as  $\frac{\mu}{\rho}$ .

We will begin by nondimensionalizing (4.1.7). To show that pressure is only a function of  $x$ , we put the pressure term on one side and aim to show the other side of the equation is negligible:

$$\begin{aligned} \frac{\partial p}{\partial r} &= \mu \left( \frac{\partial^2 u_r}{\partial r^2} + \frac{1}{r} \frac{\partial u_r}{\partial r} + \frac{\partial^2 u_r}{\partial x^2} - \frac{u_r}{r^2} \right) - \rho \left( \frac{\partial u_r}{\partial t} + u_r \frac{\partial u_r}{\partial r} + u_x \frac{\partial u_r}{\partial x} \right) \\ \frac{\rho V_x^2}{R} \frac{\partial \tilde{p}}{\partial \tilde{r}} &= \mu \left( \frac{V_r}{R^2} \frac{\partial^2 \tilde{u}_r}{\partial \tilde{r}^2} + \frac{V_r}{R^2 \tilde{r}} \frac{\partial \tilde{u}_r}{\partial \tilde{r}} + \frac{V_r}{L^2} \frac{\partial^2 \tilde{u}_r}{\partial \tilde{x}^2} - \frac{V_r \tilde{u}_r}{R^2 \tilde{r}^2} \right) - \rho \left( \frac{V_r}{T} \frac{\partial \tilde{u}_r}{\partial \tilde{t}} + \frac{V_r^2}{R} \tilde{u}_r \frac{\partial \tilde{u}_r}{\partial \tilde{r}} + \frac{V_r V_x}{L} \tilde{u}_x \frac{\partial \tilde{u}_r}{\partial \tilde{x}} \right) \\ \frac{\partial \tilde{p}}{\partial \tilde{r}} &= \frac{\nu}{R} \frac{V_r}{V_x^2} \left( \frac{\partial^2 \tilde{u}_r}{\partial \tilde{r}^2} + \frac{1}{\tilde{r}} \frac{\partial \tilde{u}_r}{\partial \tilde{r}} - \frac{\tilde{u}_r}{\tilde{r}^2} \right) + \frac{R \nu}{L^2} \frac{V_r}{V_x^2} \frac{\partial^2 \tilde{u}_r}{\partial \tilde{x}^2} - \frac{V_r^2}{V_x^2} \left( \frac{\partial \tilde{u}_r}{\partial \tilde{t}} + \tilde{u}_r \frac{\partial \tilde{u}_r}{\partial \tilde{r}} + \tilde{u}_x \frac{\partial \tilde{u}_r}{\partial \tilde{x}} \right). \end{aligned}$$

Note that each term contains  $\frac{V_r}{V_x}$ . By our assumption,  $\frac{V_r}{V_x} \rightarrow 0$ . The nondimensionalized equation for (4.1.7) therefore becomes

$$\frac{\partial \tilde{p}}{\partial \tilde{r}} \approx 0.$$

As expected, pressure is not a function of  $r$ , implying that pressure is only a function of time  $t$  and space  $x$ .

Next, nondimensionalize (4.1.6) to determine the Reynold's number:

$$\begin{aligned}\rho \left( \frac{V_x}{T} \frac{\partial \tilde{u}_x}{\partial \tilde{t}} + \frac{V_r V_x \tilde{u}_r}{R} \frac{\partial \tilde{u}_x}{\partial \tilde{r}} + \frac{V_x^2}{L} \tilde{u}_x \frac{\partial \tilde{u}_x}{\partial \tilde{x}} \right) &= -\frac{\rho V_x^2}{L} \frac{\partial \tilde{p}}{\partial \tilde{x}} + \mu \left( \frac{V_x}{R^2} \frac{\partial^2 \tilde{u}_x}{\partial \tilde{r}^2} + \frac{V_x}{R^2 \tilde{r}} \frac{\partial \tilde{u}_x}{\partial \tilde{r}} + \frac{V_x}{L^2} \frac{\partial^2 \tilde{u}_x}{\partial \tilde{x}^2} \right) \\ \left( \frac{\partial \tilde{u}_x}{\partial \tilde{t}} + \tilde{u}_r \frac{\partial \tilde{u}_x}{\partial \tilde{r}} + \tilde{u}_x \frac{\partial \tilde{u}_x}{\partial \tilde{x}} \right) &= -\frac{\partial \tilde{p}}{\partial \tilde{x}} + \frac{L \nu}{R^2 V_x} \left( \frac{\partial^2 \tilde{u}_x}{\partial \tilde{r}^2} + \frac{1}{\tilde{r}} \frac{\partial \tilde{u}_x}{\partial \tilde{r}} \right) + \frac{\nu}{L V_x} \frac{\partial^2 \tilde{u}_x}{\partial \tilde{x}^2} \\ \left( \frac{\partial \tilde{u}_x}{\partial \tilde{t}} + \tilde{u}_r \frac{\partial \tilde{u}_x}{\partial \tilde{r}} + \tilde{u}_x \frac{\partial \tilde{u}_x}{\partial \tilde{x}} \right) &= -\frac{\partial \tilde{p}}{\partial \tilde{x}} + \frac{\nu}{R V_x} \left( \frac{L}{R} \frac{\partial^2 \tilde{u}_x}{\partial \tilde{r}^2} + \frac{L}{R \tilde{r}} \frac{\partial \tilde{u}_x}{\partial \tilde{r}} + \frac{R}{L} \frac{\partial^2 \tilde{u}_x}{\partial \tilde{x}^2} \right)\end{aligned}$$

resulting in

$$\mathcal{R}e = \frac{R V_x}{\nu}.$$

Again, by our assumption,  $\frac{R}{L} \rightarrow 0$ . Thus,

$$\left( \frac{\partial \tilde{u}_x}{\partial \tilde{t}} + \tilde{u}_r \frac{\partial \tilde{u}_x}{\partial \tilde{r}} + \tilde{u}_x \frac{\partial \tilde{u}_x}{\partial \tilde{x}} \right) = -\frac{\partial \tilde{p}}{\partial \tilde{x}} + \frac{\nu}{R V_x} \left( \frac{L}{R} \frac{\partial^2 \tilde{u}_x}{\partial \tilde{r}^2} + \frac{L}{R \tilde{r}} \frac{\partial \tilde{u}_x}{\partial \tilde{r}} \right)$$

which can be rewritten as

$$\left( \frac{\partial \tilde{u}_x}{\partial \tilde{t}} + \tilde{u}_r \frac{\partial \tilde{u}_x}{\partial \tilde{r}} + \tilde{u}_x \frac{\partial \tilde{u}_x}{\partial \tilde{x}} \right) = -\frac{\partial \tilde{p}}{\partial \tilde{x}} + \frac{1}{\mathcal{R}e} \frac{L}{R} \left( \frac{\partial^2 \tilde{u}_x}{\partial \tilde{r}^2} + \frac{1}{\tilde{r}} \frac{\partial \tilde{u}_x}{\partial \tilde{r}} \right).$$

The conservation of momentum can be rewritten in dimensionalized form as

$$\frac{\partial u_x}{\partial t} + u_r \frac{\partial u_x}{\partial r} + u_x \frac{\partial u_x}{\partial x} = -\frac{1}{\rho} \frac{\partial p}{\partial x} + \nu \left[ \frac{1}{r} \frac{\partial}{\partial r} \left( r \frac{\partial u_x}{\partial r} \right) \right]. \quad (\text{A.0.1})$$

---

---

## Appendix B

---

### Wall model derivatives

We derive the necessary derivatives for the Kelvin viscoelastic model.

The equations for conservation of mass and conservation of momentum are

$$\frac{\partial A}{\partial t} + \frac{\partial q}{\partial x} = 0$$

$$\frac{\partial q}{\partial t} + \left( \frac{\gamma+2}{\gamma+1} \right) \frac{\partial}{\partial x} \left( \frac{q^2}{A} \right) = -\frac{A}{\rho} \frac{\partial p}{\partial x} - 2(\gamma+2)\pi \nu \frac{q}{A},$$

respectively, where the conservation of momentum in its expanded form is

$$\frac{\partial q}{\partial t} + \left( \frac{\gamma+2}{\gamma+1} \right) \left( \frac{2q}{A} \frac{\partial q}{\partial x} - \left( \frac{q}{A} \right)^2 \frac{\partial A}{\partial x} \right) = -\frac{A}{\rho} \frac{\partial p}{\partial x} - 2(\gamma+2)\pi \nu \frac{q}{A}.$$

For any given wall model, we will relate cross-sectional area to stress and diastolic area such that

$$A(x, t) = A \left[ \varepsilon \left( p(x, t), r_0(x), t \right), r_0(x) \right].$$

Our conservation equations can then be written in matrix form as

$$\mathbf{E} \frac{\partial \mathbf{U}}{\partial t} + \mathbf{B} \frac{\partial \mathbf{U}}{\partial x} = \mathbf{G} \quad (\text{B.0.1})$$

where

$$\mathbf{U} = \begin{bmatrix} U_1 \\ U_2 \end{bmatrix} = \begin{bmatrix} p \\ q \end{bmatrix}, \quad (\text{B.0.2})$$

$$\mathbf{E} = \begin{bmatrix} \frac{\partial A}{\partial \varepsilon} \frac{\partial \varepsilon}{\partial p} & 0 \\ 0 & 1 \end{bmatrix}, \quad (\text{B.0.3})$$

$$\mathbf{B} = \begin{bmatrix} 0 & 1 \\ -\left(\frac{\gamma+2}{\gamma+1}\right) \left(\frac{q}{A}\right)^2 \frac{\partial A}{\partial \varepsilon} \frac{\partial \varepsilon}{\partial p} + \frac{A}{\rho} & \frac{2q}{A} \left(\frac{\gamma+2}{\gamma+1}\right) \end{bmatrix}, \text{ and} \quad (\text{B.0.4})$$

$$\mathbf{G} = \begin{bmatrix} -\frac{\partial A}{\partial \varepsilon} \frac{\partial \varepsilon}{\partial t} \\ -2(\gamma+2)\pi \nu \frac{q}{A} + \frac{\gamma+2}{\gamma+1} \left(\frac{q}{A}\right)^2 \left( \frac{\partial A}{\partial r_0} \frac{\partial r_0}{\partial x} + \frac{\partial A}{\partial \varepsilon} \frac{\partial \varepsilon}{\partial x} \right) \end{bmatrix}, \quad (\text{B.0.5})$$

corresponding to the “flipped” solver with  $p$ ,  $q$ , and  $A$  as dependent variables representing pressure, volumetric flow, and cross-sectional area, respectively. The parameters in the model ( $\gamma$ ,  $\rho$ , and  $\nu$ ) are assigned values based upon those found in outside literature.

The main derivatives discussed in this appendix are  $\frac{\partial A}{\partial \varepsilon} \frac{\partial \varepsilon}{\partial p}$ ,  $\frac{\partial A}{\partial \varepsilon} \frac{\partial \varepsilon}{\partial t}$ ,  $\frac{\partial A}{\partial r_0} \frac{\partial r_0}{\partial x}$ , and  $\frac{\partial A}{\partial \varepsilon} \frac{\partial \varepsilon}{\partial x}$ . The Kelvin model uses an exponential creep function and a linear elastic response to define the wall model. We can write this model as

$$\varepsilon(x, t) = (1 - A_1) \frac{r_0(x)}{Eh} (p(x, t) - p_0) + \int_{t_0}^t \frac{r_0(x)}{Eh} (p(x, t) - p_0) \frac{A_1}{b_1} e^{-(t-\gamma)/b_1} d\gamma \quad (\text{B.0.6})$$

$$\varepsilon = 1 - \sqrt{\frac{A_0(x)}{A(x, t)}} \Rightarrow A(x, t) = \frac{A_0(x)}{(1 - \varepsilon(x, t))^2} \quad (\text{B.0.7})$$

where  $A_1$  is the amplitude associated with relaxation time  $b_1$ ,  $p_0$  taken to be a pressure of 0

mmHg, and  $A_0 = A_0(x)$ ,  $r_0 = r_0(x)$ , and  $Eh$ , are as they were in the elastic model. Therefore, for the Kelvin viscoelastic wall model, we have

$$A(x, t) = A[\varepsilon(p(x, t), r_0(x), t), r_0(x)].$$

The necessary derivative terms must be found to formulate the weak form:

$$\frac{\partial A}{\partial \varepsilon} \frac{\partial \varepsilon}{\partial p} \quad (\text{B.0.8})$$

$$\frac{\partial A}{\partial \varepsilon} \frac{\partial \varepsilon}{\partial t} \quad (\text{B.0.9})$$

$$\frac{\partial A}{\partial r_0} \frac{dr_0}{dx} \quad (\text{B.0.10})$$

$$\frac{\partial A}{\partial \varepsilon} \frac{\partial \varepsilon}{\partial x}. \quad (\text{B.0.11})$$

From (B.0.6) and (B.0.7), we find

$$\frac{\partial A}{\partial \varepsilon} = \frac{2A_0}{(1-\varepsilon)^3} \quad (\text{B.0.12})$$

$$\frac{\partial \varepsilon}{\partial p} = (1-A_1) \frac{r_0}{Eh} + \int_{t_0}^t \frac{r_0}{Eh} \frac{A_1}{b_1} e^{-(t-\gamma)/b_1} d\gamma$$

and thus (B.0.8) is equivalent to

$$\frac{\partial A}{\partial \varepsilon} \frac{\partial \varepsilon}{\partial p} = \frac{2A_0}{(1-\varepsilon)^3} \left[ (1-A_1) \frac{r_0}{Eh} + \int_{t_0}^t \frac{r_0}{Eh} \frac{A_1}{b_1} e^{-(t-\gamma)/b_1} d\gamma \right]. \quad (\text{B.0.13})$$

Corresponding to (B.0.9), we have already found  $\frac{\partial A}{\partial \varepsilon}$  and then we calculate

$$\frac{\partial \varepsilon}{\partial t} = \frac{r_0}{Eh} (p-p_0) \frac{A_1}{b_1} - \int_{t_0}^t \frac{r_0}{Eh} (p-p_0) \frac{A_1}{b_1^2} e^{-(t-\gamma)/b_1} d\gamma$$



based on the Leibniz integral rule. Therefore (B.0.9) reduces to

$$\frac{\partial A}{\partial \varepsilon} \frac{\partial \varepsilon}{\partial t} = \frac{2A_0}{(1-\varepsilon)^3} \left[ \frac{r_0}{Eh} (p-p_0) \frac{A_1}{b_1} - \int_{t_0}^t \frac{r_0}{Eh} (p-p_0) \frac{A_1}{b_1^2} e^{-(t-\gamma)/b_1} d\gamma \right]. \quad (\text{B.0.14})$$

Further note

$$\frac{\partial A}{\partial A_0} = \frac{1}{(1-\varepsilon)^2} \quad (\text{B.0.15})$$

while

$$\frac{\partial A_0}{\partial r_0} = 2\pi r_0.$$

Also, from the implicit differentiation, determine

$$\frac{dr_0}{dx} = \frac{r_0}{L} \log \left( \frac{r_{bot}}{r_{top}} \right).$$

Then (B.0.10) and (B.0.11) are found to be

$$\frac{\partial A}{\partial r_0} \frac{dr_0}{dx} = \frac{2\pi r_0^2}{L(1-\varepsilon)^2} \log \left( \frac{r_{bot}}{r_{top}} \right) \quad (\text{B.0.16})$$

$$\frac{\partial A}{\partial \varepsilon} \frac{\partial \varepsilon}{\partial x} = -\frac{2A_0}{(1-\varepsilon)^3} \frac{r_0}{L} \frac{k_1 k_2 e^{k_2 r_0}}{(k_1 e^{k_2 r_0} + k_3)^2} \log \left( \frac{r_{bot}}{r_{top}} \right) \left( (1-A_1)(p-p_0) + \int_{t_0}^t (p-p_0) \frac{A_1}{b_1} e^{-(t-\gamma)/b_1} d\gamma \right).$$

---

---

## Appendix C

---

### Hyperbolicity of PDEs

Quasilinear first-order partial differential equations have the form

$$\frac{\partial \mathbf{U}}{\partial t} + \tilde{\mathbf{A}} \frac{\partial \mathbf{U}}{\partial x} = \tilde{\mathbf{B}} \quad (\text{C.0.1})$$

where  $\mathbf{U} = [p, q]^\top$  and  $\tilde{\mathbf{A}}$  and  $\tilde{\mathbf{B}}$  are functions of  $(x, t)$  and  $\mathbf{U}$  [111]. A system is then termed hyperbolic if  $\tilde{\mathbf{A}}$  is diagonalizable.

#### C.1 Elastic wall model

Following (C.0.1), the governing equations (4.1.21) can be written in quasilinear form where  $\tilde{\mathbf{A}} = \mathbf{E}^{-1} \mathbf{B}$  and  $\tilde{\mathbf{B}} = \mathbf{E}^{-1} \mathbf{G} = \mathbf{G}$ . Matrices  $\mathbf{E}$ ,  $\mathbf{B}$ , and  $\mathbf{G}$  are as defined in Chapter 6. Hyperbolic systems are analyzed by studying their characteristics which can be found from the curves  $(x(s), t(s))$  in the  $(x, t)$  plane. Along these curves, the system of PDEs reduces to a system of ordinary differential equations (ODEs). Consider the curve given by  $(x(s), t(s))$  parameterized by  $s$ . The total derivative of  $\mathbf{U}$  with respect to  $s$  is

$$\frac{d\mathbf{U}}{ds} = \frac{\partial \mathbf{U}}{\partial x} \frac{dx}{ds} + \frac{\partial \mathbf{U}}{\partial t} \frac{dt}{ds}.$$

Taking  $t = s$  results in  $dt/ds = 1$  and a curve now defined by  $(x(t), t)$ . Let  $c = dx/dt$  and the total derivative can be written as

$$\frac{dU}{dt} = c \frac{\partial U}{\partial x} + \frac{\partial U}{\partial t}.$$

Equations (4.1.21) can be written as

$$\begin{bmatrix} 1 & 0 & 0 & \frac{\partial p}{\partial A} \\ 0 & 1 & \frac{A}{\rho} - \left(\frac{\gamma+2}{\gamma+1}\right)\left(\frac{q}{A}\right)^2 \frac{\partial A}{\partial p} & \frac{2q}{A} \left(\frac{\gamma+2}{\gamma+1}\right) \\ 1 & 0 & c & 0 \\ 0 & 1 & 0 & c \end{bmatrix} \begin{bmatrix} p_t \\ q_t \\ p_x \\ q_x \end{bmatrix} = \begin{bmatrix} 0 \\ -2(\gamma+2)\pi v_A^q + \left(\frac{\gamma+2}{\gamma+1}\right)\left(\frac{q}{A}\right)^2 \frac{\partial A}{\partial x} \\ dp/dt \\ dq/dt \end{bmatrix}$$

and rewritten as

$$\begin{bmatrix} \mathbf{I} & \mathbf{E}^{-1}\mathbf{B} \\ \mathbf{I} & c\mathbf{I} \end{bmatrix} \begin{bmatrix} \mathbf{U}_t \\ \mathbf{U}_x \end{bmatrix} = \begin{bmatrix} \mathbf{G} \\ \mathbf{U}_t \end{bmatrix}.$$

The system can then be simplified as

$$\begin{bmatrix} \mathbf{I} & \mathbf{E}^{-1}\mathbf{B} \\ \mathbf{0} & c\mathbf{I} - \mathbf{E}^{-1}\mathbf{B} \end{bmatrix} \begin{bmatrix} \mathbf{U}_t \\ \mathbf{U}_x \end{bmatrix} = \begin{bmatrix} \mathbf{G} \\ \mathbf{U}_t - \mathbf{G} \end{bmatrix}$$

which only has a solution if and only if  $(c\mathbf{I} - \mathbf{E}^{-1}\mathbf{B})\mathbf{U}_x = \mathbf{U}_t - \mathbf{G}$  has a solution. Because we are interested in solutions along the characteristics, we require that the equation is singular, i.e.  $|c\mathbf{I} - \mathbf{E}^{-1}\mathbf{B}| = 0$ . The characteristic velocity  $c$  can be found by solving

$$|c\mathbf{I} - \mathbf{E}^{-1}\mathbf{B}| = 0 \Rightarrow \begin{vmatrix} c & -\frac{\partial p}{\partial A} \\ -\frac{A}{\rho} - \left(\frac{\gamma+2}{\gamma+1}\right)\left(\frac{q}{A}\right)^2 \frac{\partial A}{\partial p} & c - \frac{2q}{A} \left(\frac{\gamma+2}{\gamma+1}\right) \end{vmatrix} = 0.$$

This results in

$$c = \frac{q}{A} \left(\frac{\gamma+2}{\gamma+1}\right) \pm \sqrt{\left(\frac{q}{A}\right)^2 \left(\frac{\gamma+2}{\gamma+1}\right) \left[\frac{\gamma+2}{\gamma+1} - 1\right] + \frac{\partial p}{\partial A} \frac{A}{\rho}}.$$

We note that  $\tilde{\mathbf{A}}$  (or  $\mathbf{E}^{-1}\mathbf{B}$ ) is diagonalizable because the eigenvalues are unique and real, and thus conclude that the system of PDEs is hyperbolic with the elastic wall model. We

define the system on a finite domain and impose boundary conditions in addition to our initial conditions. For each vessel, an inlet and outlet boundary condition are specified.

## C.2 Kelvin linear viscoelastic wall model

As a recap, the full system with the Kelvin wall model is

$$\begin{aligned} \varepsilon(t) + \tau_1 \frac{d\varepsilon}{dt} &= \frac{r_0}{Eh} \left( p(t) + \tau_2 \frac{dp}{dt} \right), \\ \frac{\partial A}{\partial t} + \frac{\partial q}{\partial x} &= 0, \\ \frac{\partial q}{\partial t} + \left( \frac{\gamma+2}{\gamma+1} \right) \frac{\partial}{\partial x} \left( \frac{q^2}{A} \right) &= -\frac{A}{\rho} \frac{\partial p}{\partial x} - 2(\gamma+2)\pi \nu \frac{q}{A}. \end{aligned} \tag{C.2.1}$$

The system can be written in matrix form

$$L \frac{\partial U}{\partial t} + M \frac{\partial U}{\partial x} = N$$

where

$$\begin{aligned} L &= \begin{bmatrix} \frac{\tau_1}{2A} \sqrt{\frac{A_0}{A}} & 0 & -\frac{r_0}{Eh} \tau_2 \\ 1 & 0 & 0 \\ 0 & 1 & 0 \end{bmatrix}, & M &= \begin{bmatrix} 0 & 0 & 0 \\ 0 & 1 & 0 \\ -\frac{\gamma+2}{\gamma+1} \left( \frac{q}{A} \right)^2 & 2 \left( \frac{\gamma+2}{\gamma+1} \right) \frac{q}{A} & \frac{A}{\rho} \end{bmatrix}, \text{ and} \\ N &= \begin{bmatrix} \frac{r_0}{Eh} p - 1 + \sqrt{\frac{A_0}{A}} \\ 0 \\ -2(\gamma+2)\pi \nu \frac{q}{A} \end{bmatrix}. \end{aligned}$$

The system can be written in the form of (C.0.1) by multiplying through by  $L^{-1}$ . For simplicity,  $\tilde{A} = L^{-1}M$  and  $\tilde{G} = L^{-1}N$  where

$$\tilde{A} = \begin{bmatrix} 0 & 1 & 0 \\ -\frac{\gamma+2}{\gamma+1}\left(\frac{q}{A}\right)^2 & 2\left(\frac{\gamma+2}{\gamma+1}\right)\frac{q}{A} & \frac{A}{\rho} \\ 0 & \frac{Eh}{r_0}\frac{\tau_1}{\tau_2}\frac{1}{2A}\sqrt{\frac{A_0}{A}} & 0 \end{bmatrix} \quad \text{and} \quad \tilde{G} = \begin{bmatrix} 0 \\ -2(\gamma+2)\pi\nu\frac{q}{A} \\ -\frac{Eh}{r_0}\frac{1}{\tau_2}\left(\frac{r_0}{Eh}p-1+\sqrt{\frac{A_0}{A}}\right) \end{bmatrix}.$$

$\tilde{A}$  is diagonalizable if the eigenvalues are real and unique. The eigenvalues  $\lambda_i$  for  $i = 1, 2, 3$  are

$$\lambda_1 = 0, \quad \lambda_{2,3} = \left(\frac{\gamma+2}{\gamma+1}\right)\frac{q}{A} \pm \sqrt{\frac{1}{2\rho}\sqrt{\frac{A_0}{A}}\frac{Eh}{r_0}\frac{\tau_1}{\tau_2} + \left(\frac{q}{A}\right)^2\frac{\gamma+2}{(\gamma+1)^2}}$$

where  $A_0, A > 0$ , and thus the eigenvalues are all real and unique, ensuring the system of PDEs is hyperbolic.

---

---

## Appendix D

---

### The Nelder Mead Method

To minimize a cost function  $J(\theta)$  where  $\theta$  is the parameter set, the problem is initialized by building a simplex with  $n_p + 1$  vertices in the  $n_p$  parameter space. The user inputs an initial guess for the parameter vector  $\theta_{\text{init}}$  which creates the initial vertex. The remaining  $n_p$  vertices are obtained by perturbing  $\theta_{\text{init}}$ . Cost function  $J$  is then evaluated at each of the vertices of the simplex. An iterative process ensues in which the vertex with the highest-valued cost function is replaced by another vertex to minimize the cost function. Iterations continue until a user-defined tolerance is reached or the maximum number of function evaluations (as specified by the user) has been exceeded. The latter signifies a failure to converge. An outline of the algorithm is shown below:

1. User specifies initial guess for parameter vector  $\theta_{\text{init}} = x_1$  and  $x_2, x_3, \dots, x_{n_p+1}$  are selected by perturbing  $x_1$ .  $J$  is evaluated at each point and ordered such that  $J(x_1) \leq J(x_2) \leq \dots \leq J(x_{n_p+1})$ , where  $x_1$  is considered the best vertex (with the lowest cost function value) and  $x_{n_p+1}$  is the worst.
2. Calculate  $x_0$ , the *centroid* of all points except  $x_{n_p+1}$  via

$$x_0 = \frac{1}{n_p} \sum_{i=1}^{n_p} x_i.$$

3. The reflected point  $x_r$  is calculated using the centroid point:  $x_r = x_0 + \alpha(x_0 - x_{n_p})$  where  $\alpha > 0$ . If  $J(x_1) \leq J(x_r) < J(x_{n_p})$ , the worst point  $x_{n_p+1}$  is replaced by the reflected point  $x_r$  and the algorithm starts over at Step 1. If not, Step 3 is repeated. If  $J(x_r) < J(x_1)$ , go to Step 3a. If  $J(x_r) \geq J(x_{n_p})$ , go to Step 3b.

(a) An expanded point  $x_e$  is calculated:  $x_e = x_0 + \rho(x_r - x_0)$ . If the expanded point is better than the reflected point, i.e.  $J(x_e) < J(x_r)$ , the worst point is replaced by the expanded point and Step 1 is repeated. If  $J(x_e) > J(x_r)$ , the reflected point replaces the worst point and the algorithm continues from Step 1 with the newly formed simplex.

(b) A contraction point  $x_c$  is calculated. There are two scenarios that determine the type of contraction to calculate:  $J(x_r) \geq J(x_{n_p})$  and  $J(x_r) < J(x_{n_p+1})$  or  $J(x_r) \geq J(x_{n_p})$  and  $J(x_r) \geq J(x_{n_p+1})$ . The former requires an outside contraction while the latter requires an inside contraction. In either scenario,  $0 < \gamma < 1$ .

i. **Outside contraction.** The contraction point is calculated as  $x_c = x_0 + \gamma(x_r - x_0)$ . If  $J(x_c) < J(x_r)$ , the worst point is replaced with  $x_c$  and the algorithm starts over from Step 1. Otherwise, move to Step 4.

ii. **Inside contraction.** The contraction point is calculated as  $x_c = x_0 + \gamma(x_{n_p+1} - x_0)$ . If  $J(x_c) < J(x_{n_p+1})$ , replace the worst point with  $x_c$  and go to Step 1. Otherwise, move to Step 4.

4. The shrinkage step produces  $n_p$  new vertices by replacing the points following

$$x_i = x_1 + \omega(x_i - x_1) \quad \text{for } i \in \{2, 3, \dots, n_p + 1\}$$

where the standard  $\omega = 1/2$ . After the new simplex has been defined, the process begins over at Step 1.

5. The process is repeated until the termination criteria is met. The algorithm terminates when either the absolute difference between the cost function evaluated at the worst and best vertices is less than the user-specified error tolerance  $\tau$ , i.e.  $|J(x_{n_p+1}) - J(x_1)| < \tau$  or the maximum number of iterations allowed by the user  $M$  has been exceeded.

Upon completion of the Nelder Mead Method, an optimal set of parameter values  $\tilde{\theta}$  is output.